Internal Report
DESY F35D-95-13
November 1995

# Measurement of the Proton Structure Function $F_2$ and Extraction of the Gluon Density of the Proton at Low x, Using the ZEUS Detector at HERA



by

A. Goussiou

MEASUREMENT OF THE PROTON STRUCTURE FUNCTION $F_2$
AND EXTRACTION OF THE GLUON DENSITY OF THE PROTON
AT LOW $X$,
USING THE ZEUS DETECTOR AT HERA

by

ANNA GOUSSIOU

A dissertation submitted in partial fulfillment of the
requirements for the degree of

Doctor of Philosophy
(Physics)

at the
UNIVERSITY OF WISCONSIN — MADISON
1995



# Abstract

The proton structure function $F_2(x, Q^2)$ is measured in neutral current deep inelastic scattering of 26.7 GeV electrons with 820 GeV protons at the HERA collider using the ZEUS detector. The data sample, collected during the 1993 HERA running period, corresponds to an integrated luminosity of 0.545 pb$^{-1}$. Results are presented for $7 < Q^2 < 2560$ GeV$^2$ and $1.5 \cdot 10^{-1} < x < 0.16$. The structure function $F_2$ is found to rapidly rise with decreasing $x$. The scaling violations of $F_2$ are used to extract the gluon momentum density of the proton, $G(x, Q^2)$, at $Q^2 = 20$ GeV$^2$ and $9 \cdot 10^{-4} < x < 0.96 \cdot 10^{-2}$. A substantial rise of the gluon density is found at small $x$.

# Contents

# Introduction

Deep Inelastic lepton-nucleon Scattering (DIS) has played an important role in the understanding of the structure of the matter. Our current knowledge of the constituent structure of the nucleon, as well as of the strong interactions, has emerged, to a large extent, from fixed target DIS experiments over the past thirty years. The first electron-proton collider, HERA, has opened a new era in the field. Operating at a center-of-mass energy of 296 GeV, HERA has been able to probe the structure of the proton at a scale two orders of magnitude smaller than the previous fixed target experiments.

This thesis presents a measurement of the proton structure function $F_2$ using the HERA data collected with the ZEUS detector during the second year of HERA operation in 1993. A total integrated luminosity of 0.545 $pb^{-1}$ is used. The measurement covers a wide kinematic region, for momentum transfers between 7 and 2560 $GeV^2$, and fractions of the proton momentum carried by the struck constituent between $10^{-2}$ and $10^{-4}$. The results show a strong rise of $F_2$ at low momentum fractions.

A review of DIS physics and the relevant parton model, the previous and current experiments, and the most recent Parton Distribution Functions, is given in chapter 1. An overview of the HERA accelerator and the ZEUS detector is given in chapter 2. The Monte Carlo simulation is described in chapter 3. The methods of reconstruction of the event kinematics are discussed

in chapter 4. The event selection procedure is discussed at length in chapter 5, including the selection criteria necessary to improve the accuracy of the reconstruction, and to suppress the various backgrounds. The electron energy response, crucial for kinematic reconstruction using the final state electron, is examined in chapter 6 along with a method to correct for the energy loss of the scattered electron due to inactive material. The statistics and event characteristics of the final sample are given in chapter 7. The $F_2$ extraction method is described and the final results on $F_2$ are given in chapter 8. The scaling violations of $F_2$ are used in chapter 9 to extract the gluon density of the proton. The final results are discussed in chapter 10, while a brief summary and future outlook are given in chapter 11.



# Chapter 1

# Review of Deep Inelastic Scattering

## 1.1 The Structure of the Nucleon

The first evidence for internal nuclear structure appeared in the early 1950s from elastic scattering of electrons from the proton, an experiment performed by Hofstadter and his collaborators at the linear electron accelerator at Stanford.[1] The elastic scattering cross section was observed to drop sharply with increasing momentum transfer, relative to that of a point charge. This implied a diffused charge and magnetic moment distribution for the proton, with no underlying point-like constituents.

In the early 1960s the bootstrap theory was developed, in an attempt to understand hadronic interactions.[2] It assumed no fundamental particles and considered each hadron as a composite of the others.

In 1961 Gell-Mann and Ne'eman independently proposed the "Eightfold Way", a scheme for classifying the hadrons according to their charge and strangeness, using SU(3) symmetry.[3]

In 1964, Gell-Mann and Zweig independently introduced the notion of *quarks* as the elementary constituents of hadrons.[4] The quarks were proposed with three different types, called *flavors*, spin equal to $\frac{1}{2}$, and fractional electric

charges. This model was found to reproduce the multiplet structures of all the observed hadrons. Three (anti)quarks were required for (anti)baryons, and quark-antiquark pairs for mesons. A new quantum number, *color*, appearing in three states ('red', 'green', and 'blue'), was assigned to quarks, in order to make the baryons' wave functions consistent with the Pauli Exclusion principle.[5] Although initially quarks were very successful as the building blocks of unitary symmetry, the failure of numerous free-quark searches led to the belief that they were merely mathematical constructs, without any physical manifestation.

The introduction of quarks was followed by the development of "current algebra", a field theory that examined hadrons under the influence of weak and electromagnetic interactions, and gave rise to several sum rules, derived by Bjorken and others.

In late 1967 a long series of experiments on deep inelastic (i.e. large-energy-loss) electron-proton scattering started at the Stanford Linear Accelerator Center (SLAC).[6] The early results from these experiments featured two unexpected effects: the deep inelastic cross sections were found to fall only weakly with increasing momentum-transfer, and the deep inelastic *Structure Functions*, which could be interpreted as the momentum distributions of the proton constituents, depended only on the fraction of momentum carried by the struck constituent of the proton. This second surprising feature in the data, called *scale invariance*, was found following a suggestion by Bjorken. In 1969, he had predicted the scaling of the proton structure functions in the deep inelastic region, on the basis of quark model current algebra calculations.[7]

Bjorken's scaling hypothesis and the early SLAC data led Feynman to



apply his *parton* model, a constituent model he had developed to explain hadron-hadron inclusive interactions at high energies, to deep inelastic electron scattering.[8] He assumed that the proton was composed of free point-like partons, from which the electron scatters incoherently.

In an application of the parton model, Bjorken and Paschos identified the partons with the spin-$\frac{1}{2}$ quarks.[9] They studied a system of three quarks, commonly called *valence* quarks, in a background of quark-antiquark pairs, known as *sea* quarks.

In a more detailed description of the quark-parton model, Kuti and Weisskopf added to the constituent model of the nucleon the neutral *gluons*, the field quanta responsible for the binding of the quarks.[10]

By 1973 *Quantum Chromodynamics* (QCD), a comprehensive theory of quarks and gluons and their strong interactions, was constructed. The concept of *asymptotic freedom*[11] provided an explanation for the inconsistency between the 'free' behavior of the partons during lepton scattering, where short distances were probed, and the strong final-state interactions required to account for the fact that no free quarks had ever been observed in the laboratory. In non-Abelian gauge theories, like QCD, the effective coupling which characterises the interaction between two particles, and which is a function of the distance between them, goes to zero as the separation becomes very small (asymptotically zero). Thus, quarks and gluons seem to be effectively free when probed at short distance. The *infrared slavery* mechanism, on the other hand, provided the origin of the *confinement* of quarks in 'colorless' hadrons.[12] When a quark and antiquark separate, their color interaction becomes stronger, due to the interaction of gluons with one another, which

confines the color field lines of force between the $q$ and $\bar{q}$ into a tube-like region. If this color tube has a constant energy density per unit length, the potential energy between the $q$ and $\bar{q}$ will increase with separation (i.e. linearly rising potential energy), as particles are produced. Therefore, quarks and gluons can never escape.

The first deep inelastic electron-proton scattering results from SLAC, and the introduction of the naive parton model, were followed by several fixed target deep inelastic scattering experiments at major laboratories. SLAC experiments continued to use electron beams, whereas muon and neutrino beams of higher energies were used at CERN and FNAL. New, more precise data showed logarithmic deviations of the scaling invariance for the proton structure functions.[13] These results were explained by the radiative QCD corrections, generated by the gluons.

Throughout the 1980's the nucleon structure functions were measured with increasing precision over more extended kinematic regions. However, since the center-of-mass energy at fixed target experiments is proportional to the square root of the beam energy, fixed target DIS experiments are limited in their reach to high momentum transfer and to small proton momentum fraction carried by the struck quark.

Higher center-of-mass energies can be achieved at colliders, which can therefore explore extended kinematic regions. Beginning in 1992, HERA has studied deep inelastic scattering by means of collisions between electrons (or positrons) and protons. The measurement of the proton structure function has been extended by the HERA experiments, H1 and ZEUS, to a new kinematic regime, reaching two orders of magnitude higher momentum transfers,



and two orders of magnitude lower proton momentum fractions, than the fixed target experiments.

## 1.2 DIS - Definitions and Kinematics

Deep Inelastic Scattering (DIS) is defined as the scattering of a lepton from a nucleon at high momentum transfer. At the HERA collider DIS is studied in collisions between electrons or positrons and protons. The electron-proton interaction is mediated by the exchange of a single vector boson. We distinguish two classes of $ep$ DIS events, depending on the exchanged particle:

(i) Neutral Current (NC) DIS events, for virtual photon or $Z^0$ exchange:

$$e^{\pm} + p \rightarrow e^{\pm} X \tag{1.1}$$

(ii) Charged Current (CC) DIS events, for $W^{\pm}$ exchange:

$$e^{\pm} + p \rightarrow \overset{(-)}{\nu} X \tag{1.2}$$

where $X$ denotes the total hadronic system in the final state. The Feynman diagrams for NC and CC DIS events are shown in fig. 1.1.

In this thesis we restrict ourselves to the study of inclusive NC DIS scattering, between unpolarized electrons and protons, for which the final electron and hadronic final state are observed. The kinematics of such a process can be described in terms of two independent variables. We first define a number of Lorentz-invariant independent variables and then can express the kinematics in terms of any two of them.

We denote by $q$ the momentum 4-vector of the exchanged vector boson, transferred from the electron to the proton, by $k$ and $k'$ the 4-vectors of the

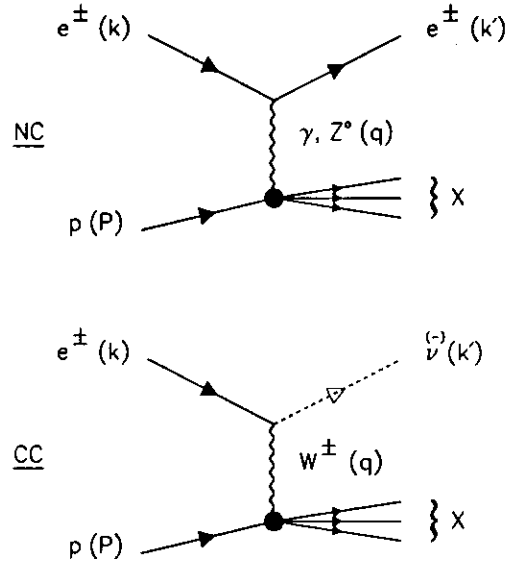


Figure 1.1: *Feynman diagrams for NC and CC DIS events.*



incident and scattered electron, respectively, and by $P$ the 4-vector of the proton.

The center of mass energy squared is given by:

$$s = (k + P)^2 \tag{1.3}$$

The 4-vector $q$ of the virtual exchanged boson is space-like and its square is a negative quantity. For convenience, we introduce the positive quantity $Q^2$ as:

$$Q^2 = -q^2 = -(k - k')^2 \tag{1.4}$$

The electron's energy loss, transferred to the hadronic system, in the proton's rest frame is given by:

$$\nu = \frac{P \cdot q}{M} = [E - E']_{\vec{P}=0} \tag{1.5}$$

where $E$, $E'$ are the incident and scattered electron energies, respectively, and $M$ is the proton mass.

The scalar variable $x$, known as Bjorken-$x$, is defined as:

$$x = \frac{Q^2}{2P \cdot q} = \left[\frac{Q^2}{2M\nu}\right]_{\vec{P}=0} \tag{1.6}$$

As shown below, $x$ can be identified with the fraction of the proton's momentum carried by the struck quark.

The scalar variable $y$, which corresponds to the fraction of the energy lost by the electron in the proton's rest frame, is defined by:

$$y = \frac{P \cdot q}{P \cdot k} = \left[\frac{\nu}{E}\right]_{\vec{P}=0} \tag{1.7}$$

The kinematically allowed region for both $x$ and $y$ is: $0 < x, y < 1$.

The variables $x$, $y$, $Q^2$ and $s$ are related by:

$$Q^2 = sxy \tag{1.8}$$

Finally, we define the invariant mass of the hadronic final state $X$ by:

$$W^2 = (P+q)^2 = M^2 + Q^2(\frac{1}{x} - 1) \tag{1.9}$$

The kinematic ranges for $Q^2$ and $W^2$ are from zero to $s$.

## 1.3 NC DIS and Structure Functions

The assumption of a single-boson exchange implies that the cross section for the deep inelastic $ep$ scattering can be factorised into a leptonic tensor $L_{\mu\nu}$ contracted with a tensor at the hadron vertex $W^{\mu\nu}$ [14]:

$$d\sigma \sim L_{\mu\nu} W^{\mu\nu}(q,p) \tag{1.10}$$

For deep inelastic scattering at values of $Q^2$ much lower than the square of the mass of the $Z^o$ ($Q^2 \gg M_Z^2$), the electron-proton interaction is mediated almost exclusively by the virtual photon. Thus, the $Z^o$ contribution to the cross section can be neglected.

The lepton vertex is described by Quantum Electrodynamics (QED) and its tensor is given by:

$$L_{\mu\nu} = 2[k'_\mu k_\nu + k'_\nu k_\mu + (\frac{q^2}{2})g_{\mu\nu}] \tag{1.11}$$

At the hadron vertex, in order to obtain the cross section for the inclusive process, we must integrate over all possible hadronic final states. The current at the hadron vertex is parametrized by the hadronic tensor which



can be constructed out of $g^{\mu\nu}$ and the independent momenta $q$ and $p$. Antisymmetric contributions to $W^{\mu\nu}$ are omitted, since their contribution to the cross section vanishes when $W^{\mu\nu}$ is contracted with the symmetric tensor $L_{\mu\nu}$. The most general form of $W^{\mu\nu}$ contains five terms. However, neglecting the parity-violating term and imposing current conservation at the hadron vertex ($q_\mu W^{\mu\nu} = q_\nu W^{\mu\nu} = 0$), only two independent terms remain:

$$W^{\mu\nu}(q,p) = [-g^{\mu\nu} + \frac{q^\mu q^\nu}{q^2}]W_1 + [p^\mu - \frac{p\cdot q}{q^2}q^\mu][p^\nu - \frac{p\cdot q}{q^2}q^\nu]\frac{1}{M^2}W_2 \tag{1.12}$$

The inelastic structure functions, $W_i$, are functions of two independent Lorentz-invariant scalar variables that can be constructed from the 4-momenta at the hadron vertex. We choose $Q^2$ and $\nu$ as these variables.

Using the leptonic and hadronic tensors, and including the flux factor and the final electron phase space, we calculate the inclusive cross section for inelastic electron-proton scattering. In terms of laboratory variables, and neglecting electron mass effects, the cross section is given by:

$$\frac{d^2\sigma}{dQ^2 d\nu} = \frac{4\pi\alpha^2}{Q^4}\frac{E'}{E}[W_2(\nu,Q^2)\cos^2(\frac{\theta}{2}) + 2W_1(\nu,Q^2)\sin^2(\frac{\theta}{2})]. \tag{1.13}$$

where $\theta$ is the angle of the scattered electron.

The DIS physics is contained in the $\nu$ and $Q^2$ dependence of the structure functions $W_1$ and $W_2$.

In the deep inelastic region, where $Q^2$ and $\nu$ are large, but $Q^2/\nu$ is finite, the structure functions $W_1$ and $\nu W_2$ become functions not of $Q^2$ and $\nu$ independently but only of the ratio $x = Q^2/2M\nu$:

$$MW_1(\nu,Q^2) \rightarrow F_1(x) \tag{1.14}$$

$$\nu W_2(\nu,Q^2) \rightarrow F_2(x). \tag{1.15}$$

The first evidence for scaling (i.e. $Q^2$-independence of the structure functions) came from the early DIS experiments at SLAC, as noted in section 1.1.

## 1.4 The Naive Quark-Parton Model

According to the parton model, the proton is composed of free point-like constituents, called partons, from which the electron scatters elastically and incoherently.

At high momentum transfer, $Q^2$, the virtual photon is probing very short distance and time scales within the proton. The short distance scale justifies the assumption of small, pointlike constituents. In the infinite momentum frame of the proton, where $|\vec{P}| \gg m, M$ ($m$ being the mass of the parton), each parton carries only a fraction $z$ of the proton's energy and momentum: $p_i \equiv z(E_p, 0, 0, -E_p)$. In this frame, relativistic time dilation slows down the rate at which partons interact with each other. Then the short time scale of the photon-parton interaction enables us to treat the struck constituents as effectively free. We can then regard the deep inelastic scattering of the electron from the proton as an incoherent sum (addition of probabilities, not amplitudes) of elastic scatterings from single free partons within the proton.

Energy and momentum conservation at the parton vertex, assuming the initial and final partons to be massless, results in:

$$0 = p_f^2 = (p_i + q)^2 = 2zP \cdot q - Q^2 \Rightarrow z = \frac{Q^2}{2P \cdot q} \equiv x, \qquad (1.16)$$

where $p_i$ and $p_f$ are the intial and final 4-momenta of the struck parton, respectively. Equation (1.16) shows that the scaling of the proton structure functions (independence of $Q^2$) can indeed be interpreted as a result of the quasi-free electron-parton scattering process.



If partons have spin $\frac{1}{2}$, the cross section for the electron- parton scattering must resemble the $e\mu$ scattering cross section:

$$\frac{d^2\sigma}{dQ^2 d\nu} = \frac{4\pi\alpha^2}{Q^2}\frac{E'}{E}\{\epsilon_i^2 \cos^2(\frac{\theta}{2}) + \epsilon_i^2 \frac{Q^2}{2m^2}\sin^2(\frac{\theta}{2})\}\delta(\nu - \frac{Q^2}{2m}) \qquad (1.17)$$

where $e_i$, $m_i$ are the electric charge and mass of the parton of type $i$, respectively.

By comparing equations (1.13) and (1.17) we can extract the contributions to $W_1$ and $W_2$ from one parton of type $i$. Summing over the contributions from all partons, $i$, we obtain the total contribution from all partons, i.e. the total structure functions of the proton, $W_1(\nu, Q^2)$ and $W_2(\nu, Q^2)$, or, according to equations (1.14) and (1.15), $F_1(x)$ and $F_2(x)$:

$$2xF_1(x) = F_2(x) \qquad (1.18)$$

$$F_2(x) = \sum_i \epsilon_i^2 x f_i(x), \qquad (1.19)$$

where $f_i(x)$ represents the probability for a parton of type $i$ to carry a fraction $x$ of the proton's momentum.

Equation (1.18), called the Callan-Gross relation,[15] is a direct consequence of the assumption of spin-$\frac{1}{2}$ quarks which couple to transversely polarised ($\lambda = \pm 1$) virtual photons. Its experimental verification provided strong evidence for the identification of the partons with the spin-$\frac{1}{2}$ quarks and antiquarks.

According to the quark-parton model the proton (neutron) is made of three valence quarks, $uud$ ($udd$), and a distribution of quark-antiquark pairs, commonly called sea quarks: $u_s\bar{u}_s$, $d_s\bar{d}_s$, $s_s\bar{s}_s$, and so on. The latter become dominant at low values of $x$.

The (anti)quark distributions inside the proton (and neutron) should add up to the total electric charge, strangeness and total momentum of the proton. While the sum rules for electric charge and strangeness were experimentally verified, providing further evidence for the parton-quark identification, the momentum sum rule revealed that the quarks and antiquarks carry only half of the proton's momentum. This last result led to the introduction of neutral partons which carry the remaining half of the proton's momentum, and which were identified with the gluons, the bosons that carry the color force in QCD.

## 1.5 QCD Parton Evolution

QCD produces interactions between quarks and gluons via the processes: $q \rightarrow qg$, $\bar{q} \rightarrow \bar{q}g$, $g \rightarrow q\bar{q}$, $g \rightarrow gg$. Explicit calculations show that these processes have a $\ln(Q^2)$ behaviour.

As $Q^2$ increases the photon acquires a higher resolution and starts to "see" each quark as surrounded by a cloud of partons (quarks and gluons), which share the proton's momentum. Therefore, the probability of finding a quark at small $x$ ("soft" quark) increases with increasing $Q^2$, while the probability of finding a quark at high $x$ decreases.

The $Q^2$ evolution of the quark and gluon densities is determined by QCD through the Gribov-Lipatov-Altarelli-Parisi (GLAP) equations [16]:

$$\frac{dq_f(x,Q^2)}{d\ln Q^2} = \frac{\alpha_s(Q^2)}{2\pi}\int_x^1 \frac{dy}{y}\left[P_{qq}(\frac{x}{y})q_f(y,Q^2) + P_{qg}(\frac{x}{y})g(y,Q^2)\right] \quad (1.20)$$

$$\frac{dg(x,Q^2)}{d\ln Q^2} = \frac{\alpha_s(Q^2)}{2\pi}\int_x^1 \frac{dy}{y}\left[\sum_f P_{gq}(\frac{x}{y})q_f(y,Q^2) + P_{gg}(\frac{x}{y})g(y,Q^2)\right] \quad (1.21)$$



The coupling constant $\alpha_s$ of the strong force is given in lowest order by [14]:

$$\alpha_s(Q^2) = \frac{12\pi}{(33-2n_f)\log(Q^2/\Lambda^2)}, \quad (1.22)$$

where $n_f$ is the number of flavors and $\Lambda$ is the QCD parameter that sets the boundary (for $Q^2 \gg \Lambda^2$) at which $\alpha_s$ becomes 'small' and the perturbative description in terms of quasi free quarks and gluons is justified.

The functions $P_{ij}(x/y)$ are called *Splitting Functions*. They give the probability that a parton (either gluon or quark) $i$, with momentum fraction $x$, originated from a parton $j$, with momentum fraction $y$, where $x < y < 1$.

In lowest order QCD the splitting functions are given by [14]:

$$P_{qq}(z) = \frac{4}{3}(\frac{1+z^2}{1-z}) \quad (1.23)$$

$$P_{qg}(z) = \frac{1}{2}(z^2+(1-z)^2) \quad (1.24)$$

$$P_{gq}(z) = \frac{4}{3}(\frac{1+(1-z)^2}{z}) \quad (1.25)$$

$$P_{gg}(z) = 6(\frac{z}{1-z} + \frac{1-z}{z} + z(1-z)) \quad (1.26)$$

where $z = x/y$. They are schematically drawn in fig. 1.2.

The logarithmic radiative QCD processes and their subsequent parton evolution result in logarithmic scaling violations, i.e. the proton structure functions are functions of both $x$ and $Q^2$.

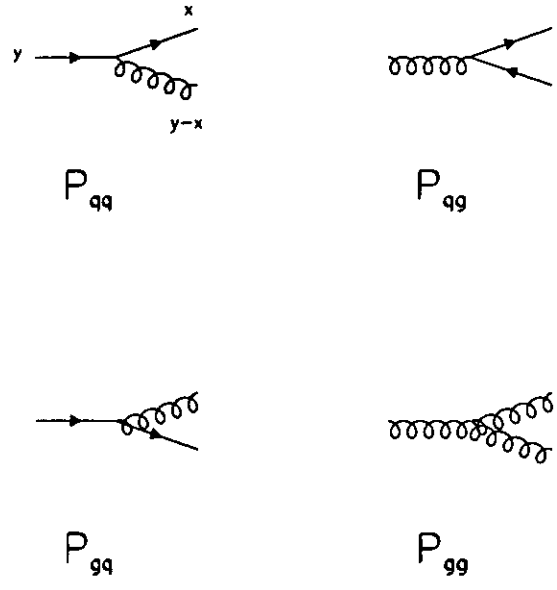


Figure 1.2: *The lowest order Splitting Functions $P_{qq}, P_{qg}, P_{gq}, P_{gg}$.*



## 1.6 General Form of the Structure Functions

At high $Q^2$ there is a probability that the vector boson exchanged between the electron and the proton will be the $Z^o$. In this case there is a third, parity-violating term in the hadronic tensor:

$$W^{\mu\nu}(q,p) = [-g^{\mu\nu} + \frac{q^\mu q^\nu}{q^2}]W_1 + [p^\mu - \frac{p\cdot q}{q^2}q^\mu][p^\nu - \frac{p\cdot q}{q^2}q^\nu]\frac{1}{M^2}W_2 - i\epsilon_{\mu\nu\kappa\lambda}\frac{p^\kappa q^\lambda}{M}W_3 \tag{1.27}$$

We then obtain the general form of the differential NC $ep$ cross section:

$$\frac{d^2\sigma^{NC}(e^\pm p)}{dxdQ^2} = \frac{4\pi\alpha^2}{xQ^4}[y^2 x\mathcal{F}_1(x,Q^2) + (1-y)\mathcal{F}_2(x,Q^2) \pm (y - y^2/2)x\mathcal{F}_3(x,Q^2)] \tag{1.28}$$

where the structure functions $\mathcal{F}_1$, $\mathcal{F}_2$, $x\mathcal{F}_3$ include both $\gamma$ and $Z^o$ exchange. In lowest order QCD (where the spin-$\frac{1}{2}$ of the quarks dictates the absorption of transversely polarised photons and results in the Callan-Gross relation, eq. (1.18)) they are given by:

$$\mathcal{F}_1^{NC}(x,Q^2) = \mathcal{F}_2^{NC}(x,Q^2)/2x \tag{1.29}$$

$$\mathcal{F}_2^{NC}(x,Q^2) = \sum_f A_f(Q^2)[xq_f(x,Q^2) + x\bar{q}_f(x,Q^2)] \tag{1.30}$$

$$x\mathcal{F}_3^{NC}(x,Q^2) = \sum_f B_f(Q^2)[xq_f(x,Q^2) - x\bar{q}_f(x,Q^2)] \tag{1.31}$$

where $q_f(x,Q^2)$, $\bar{q}_f(x,Q^2)$ represent the probability distribution for a quark and antiquark, respectively, of flavor $f$, to be found in the proton.

The coefficients $A_f$, $B_f$ include $\gamma$-exchange, $Z^o$ exchange, their interference term, and are given by [14]:

$$A_f(Q^2) = \epsilon_f^2 - 2\epsilon_f v_e v_f P_Z(Q^2) + (v_e^2 + a_e^2)(v_f^2 + a_f^2)P_Z^2(Q^2) \tag{1.32}$$

$$B_f(Q^2) = -2\epsilon_f a_e a_f P_Z(Q^2) + 4v_e v_f a_e a_f P_Z^2(Q^2). \tag{1.33}$$

$P_Z(Q^2)$ is the ratio of the $\gamma$ and $Z^o$ propagators:

$$P_Z(Q^2) = \frac{Q^2}{Q^2 + M_Z^2}. \tag{1.34}$$

The neutral current vector and axial vector couplings are given by:

$$v_f = \frac{T_{3f} - 2e_f \sin^2\theta_W}{\sin 2\theta_W} \tag{1.35}$$

$$a_f = \frac{T_{3f}}{\sin 2\theta_W} \tag{1.36}$$

respectively, where $T_{3f}$ denotes the 3rd component of the weak isospin (equal to $\frac{1}{2}$ for neutrino and $(u, c, t)$ quarks and $-\frac{1}{2}$ for electron and $(d, s, b)$ quarks) and $\theta_W$ is the weak mixing angle.

In higher order perturbation theory there is a contribution to the cross section from longitudinally polarised ($\lambda = 0$) virtual photons. This contribution is measured by the Longitudinal Structure Function $\mathcal{F}_L$:

$$\mathcal{F}_L(x, Q^2) = \mathcal{F}_2(x, Q^2) - 2x\mathcal{F}_1(x, Q^2). \tag{1.37}$$

In terms of the longitudinal structure function the NC $ep$ cross section is expressed in the form:

$$\frac{d^2\sigma^{NC}(e^{\pm}p)}{dxdQ^2} = \frac{2\pi\alpha^2}{xQ^4}[Y_+\mathcal{F}_2(x, Q^2) - y^2\mathcal{F}_L(x, Q^2) \mp Y_- x\mathcal{F}_3(x, Q^2)], \tag{1.38}$$

with $Y_\pm = 1 \pm (1 - y)^2$.



## 1.7 QED Radiative Corrections

In higher order perturbation theory the Born cross section for the $ep$ interaction is modified due to additional electroweak corrections. These corrections originate from the emission of additional real or virtual photons from either the leptons or the quarks. Hence, they can be classified as *lepton*, *quark*, and *lepton-quark interference* corrections.

The quark corrections can be absorbed into the quark distribution functions, and the corrections from the interference between the lepton and quarks are in general small.[17]

The lepton corrections can be further classified into:

(a) virtual $\gamma$ and $Z^o$ corrections. They can be vertex corrections, self energies of $\gamma$ and $Z^o$, or $\gamma Z^o$ mixing.

(b) emission of real photons. In the leading logarithm approximation, the emitted photon can be collinear either with the initial or the final state electron, in which cases we refer to "Initial State Radiation" (ISR) or "Final State Radiation" (FSR), respectively. There is a third contribution, called "Compton scattering" (CS), which refers to a hard scattering of the electron on a quasi-real photon originating from the proton.

We include radiative corrections in a factor $\delta_r$ in the double differential cross section for inclusive NC deep inelastic $ep$ scattering:

$$\frac{d^2\sigma^{NC}(e^{\pm}p)}{dxdQ^2} = \frac{2\pi\alpha^2}{xQ^4}[Y_+\mathcal{F}_2(x, Q^2) - y^2\mathcal{F}_L(x, Q^2) \mp Y_- x\mathcal{F}_3(x, Q^2)](1 + \delta_r(x, Q^2)). \tag{1.39}$$

## 1.8 Low-x phenomena

In the low $x$ region the nucleon is dominated by sea quarks and gluons, the former originating from the $q\bar{q}$ splitting of the latter. Both the quark and gluon distributions grow with increasing $Q^2$, at fixed low $x$.

As discussed in section (1.5), the evolution of the parton densities with $Q^2$ is predicted by perturbative QCD, which is applicable in the large $Q^2$ region ($Q^2 > Q_o^2$, $Q_o^2 \cong 4\text{GeV}^2$). The exact form of the equations that describe the parton evolution depends on the accuracy of the treatment of the large logarithms $\ln(Q^2)$ and/or $\ln(1/x)$.

In the *leading* $ln(Q^2)$ *approximation* only the leading logarithmic terms in $Q^2$ are kept in the perturbative expansion and the evolution equations take the form of the GLAP equations.

However, in the limit $x \to 0$ the $P'_{gq}$ and $P'_{gg}$ splitting functions become singular (see eqs. (1.25) and (1.26), where $x/y = z \to 0$). This means that at low $x$ the terms that contain the singular parts $1/x$ become important.

In the low $x$, large $Q^2$ region the terms $\ln(1/x)$ and $\ln(Q^2)$ are comparable. Keeping the products of both large logarithms in the pertubative expansion we arrive at the ***double logarithmic approximation.***[18] In this approximation the gluon distribution is given by :

$$G(x,Q^2) \equiv xg(x,Q^2) \sim exp[\sqrt{\ln\ln(Q^2/\Lambda^2)\ln(1/x)}] \qquad (1.40)$$

which predicts that the gluon (and consequently, also the sea quark) distribution at low $x$ will grow faster than any power of $\ln(1/x)$.

In the low $x$, moderate $Q^2$ region, $\ln(1/x)$ terms become larger than the leading $\ln(Q^2)$ terms. Here we apply the *leading* $ln(1/x)$ *approximation*, where



we resum the terms that contain leading powers of $\ln(1/x)$ (and arbitrary powers of $\ln(Q^2)$). The summation is done by the Balitsky-Fadin-Kuraev-Lipatov (BFKL) equation,[19] which is in effect an evolution equation in $x$. When this equation is solved analytically, it results in a gluon distribution function in the form of:

$$G(x,Q^2) \equiv xg(x,Q^2) \sim x^{-\lambda}. \qquad (1.41)$$

The growth of the parton densities with $Q^2$, which is rapid at low $x$, results in a steep increase of the DIS cross section. However, an unlimited increase would violate the Froissart bound, which requires that the total cross section must not grow faster than $\ln^2 s$.[20] Such a violation is prevented by parton recombination and saturation effects. When the numbers of gluons and sea quarks in the proton become very large, at low $x$, they begin to overlap spatially in the transverse direction and recombine via the processes $gg \to g$ and $q\bar{q} \to g$. Hence, they can no longer be treated as free partons, as was required by the QCD parton model. This interaction of partons puts an end to the growth of the parton densities in the low $x$ limit, and the DIS cross section finally reaches its saturation (geometrical) limit, equal to $\pi R^2$, $R$ being a radius parameter.

Quantitatively, the parton interaction introduces a nonlinear screening correction to the evolution equations. The modified evolution for the gluon density is expressed by the Gribov-Levin-Ryskin (GLR) equation[21]:

$$\frac{\partial xg(x,Q^2)}{\partial \ln Q^2} = \frac{3\alpha_s(Q^2)}{\pi}\int_x^1 \frac{dy}{y}[yg(y,Q^2)] - \frac{9}{16R^2}\left[\frac{3\alpha_s(Q^2)}{Q}\right]^2 \int_x^1 \frac{dy}{y}[yg(y,Q^2)]^2. \qquad (1.42)$$

The first (linear) term on the right-hand side is obtained from the GLAP

equation for gluons [eq.(1.21)] by neglecting the quark contribution to the gluon evolution (i.e. the $P_{gq}$ splitting function) and by keeping only the most singular term of the $P_{gg}$ splitting function, $P_{gg} \sim 6/z$, in the limit $x/y = z \to 0$ (double logarithmic approximation). The second term represents the screening correction, whose strength depends on the magnitude of the radius parameter $R$. $R$ is expected to be comparable to the hadronic radius ($\sim 5$ GeV$^{-1}$) for a gluon saturation uniformly distributed in the nucleon, or comparable to the constituent (valence quark) radius ($\sim 2$ GeV$^{-1}$) for gluons concentrated around the valence quarks ("*hot spots*" model ).

The GLR equation is expected to be valid for $W_{sat} \leq \alpha_s(Q^2)$, where the parameter $W_{sat}$ is defined as the ratio of the total transverse area occupied by the small-$x$ gluons in a nucleon over the total transverse area of the nucleon, $\pi R^2$. $W_{sat}$ can be obtained from the ratio of the coefficients of the second and first terms on the right-hand side of equation (1.42):

$$W_{sat} = \frac{27\pi\alpha_s(Q^2)}{16R^2Q^2} xg(x,Q^2). \tag{1.43}$$

The gluon distribution obtained from the GLR equation approaches the parton saturation limit for $x \to 0$ :

$$G^{sat}(x,Q^2) = xg^{sat}(x,Q^2) = \frac{16}{27\pi\alpha_s(Q^2)} R^2Q^2, \tag{1.44}$$

which corresponds to $W_{sat} = 1$.

For $W_{sat} \ll 1$ the parton evolution is described by the QCD parton model without screening corrections.



## 1.9 DIS Experiments

### 1.9.1 Fixed Target DIS Experiments

As discussed in section (1.1), a number of fixed target DIS experiments at SLAC, CERN and FNAL followed the first deep inelastic electron-proton scattering results from SLAC. They used electron, muon, or neutrino beams on a variety of targets.

The SLAC experiments used electron beams with an energy range $3.65 < E_e < 20$ GeV, on hydrogen and deuterium targets.

The CERN experiments used either muon beams, with energies $100 < E_\mu < 280$ GeV (EMC, BCDMS, NMC, SMC), or neutrino beams with energies $100 < E_\nu < 280$ GeV (CDHSW, WA25, WA59), on deuterium, iron and neon targets.

At FNAL, the CCFR experiment used a neutrino beam on an iron target, with $30 < E_\nu < 600$ GeV, while the E665 experiment used a muon beam of 490 GeV, on various targets.

A hydrogen target is used for the measurement of the proton structure function $F_2^p$, whereas an additional deuterium target allows the measurement of the neutron structure function $F_2^n$. Heavy nuclear targets are used for the measurement of the nucleon structure function, the average of the proton and neutron structure functions. Finally, a neutrino beam enables the measurement of the parity-violating $xF_3$ structure function, and hence, the extraction of the valence quark distributions.

The center-of-mass energy at fixed target DIS experiments is given by:

$$\sqrt{s} = \sqrt{2m_p E_{e,\mu,\nu}}. \tag{1.45}$$

which yields a maximum value approximately equal to $\sqrt{s} \simeq 31$ GeV, at the highest FNAL $\nu$ beam energy. The kinematic ranges of $x$ and $Q^2$ that can be explored, limited by beam energies and the final lepton phase space, are: $10^{-2} < x < 0.9$ and $0.1 < Q^2 < 200$ GeV$^2$.

### 1.9.2 DIS at HERA

HERA extends the measurement of the proton structure functions to lower values of $x$ and higher values of $Q^2$ than fixed target experiments.

The center-of-mass energy at the HERA $ep$ collider is given by:

$$\sqrt{s} = 2\sqrt{E_e E_p}. \tag{1.16}$$

In 1992 and 1993 HERA operated with an electron beam of energy $E_e = 26.7$ GeV and a proton beam of energy $E_p = 820$ GeV, producing a center-of-mass energy equal to $\sqrt{s} = 296$ GeV.

The maximum value of $Q^2$ that can be reached is equal to $Q^2_{max} = s = 8.75 \cdot 10^4$ GeV$^2$, whereas the lower limit for NC DIS events, in order for the scattered electron to be seen in the detectors, is a few GeV$^2$. The kinematically allowed region in $x$ and $Q^2$ is bounded by $y = 1$. Thus, the measurable region in $x$ is $10^{-4} < x < 1$.

HERA started operation in 1992, with two major detectors, ZEUS and H1. The first results on the measurement of the proton structure function $F_2$ were based on 25 nb$^{-1}$ of deep inelastic electron-proton scattering data[22,23] In the second year of operation, 1993, 20 times more data were accumulated (540 nb$^{-1}$).

HERA is able to reach two orders of magnitude smaller values of x and



two orders of magnitude higher values of $Q^2$ than fixed target experiments. However, there is still no overlap in the $(x, Q^2)$ phase space between HERA and fixed target experiments, as can be seen in fig. 1.3.

This gap would be closed were HERA to run at reduced beam energies. However, it is also possible to close the gap even at present beam energies, if the detection of the final state electron were feasible at smaller scattering angles in the ZEUS and H1 detectors. This has been achieved in more recent running by shifting the interaction point towards the direction of the proton beam, and by new detector components at small angles around the beampipe in the electron beam direction. In addition, a measurement of the proton structure function at lower values of $Q^2$ is made by considering Initial State Radiation events, where the real photon emitted from the initial state electron effectively lowers the initial state electron energy.

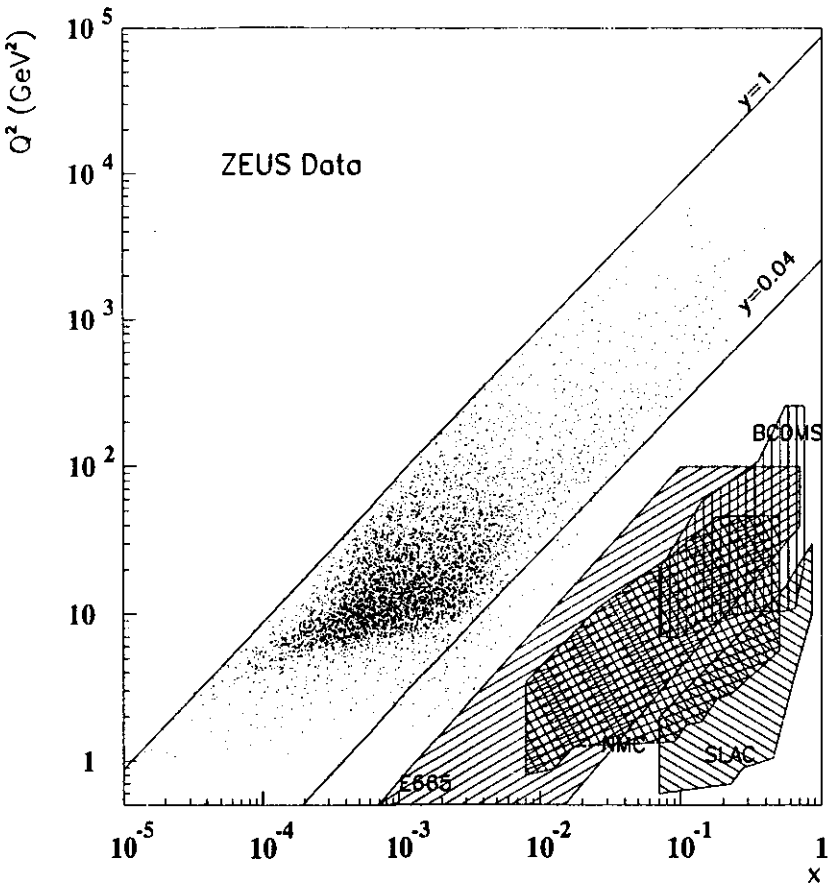


Figure 1.3: *Kinematic regions in the $(x, Q^2)$ phase space covered by the 1993 HERA data and various fixed target DIS experiments. The $y = 1$ isoline limits the kinematically allowed region. The $y = 0.01$ isoline represents a y cut used in the ZEUS analysis (see section 5.4).*



## 1.10 Parton Parametrizations

The Parton Distribution Functions (PDF's) describe the sharing of nucleon's momentum among its constituent quarks and gluons. Knowledge of PDF's is necessary for the parametrization of the nucleon's structure functions and the prediction of the cross sections for present and future colliders. Although the QCD parton model constrains the PDF's, it provides no absolute predictions. Thus, they have to be extracted from experimental data.

The Parton Distribution Functions are parametrized as a function of $x$ at a reference value $Q^2 = Q_o^2$. These parametrizations are usually simple functional forms, which satisfy QCD and contain a number of free, adjustable parameters. The initial quark and gluon distributions are evolved upward with $Q^2$, using the QCD GLAP equations (eqs. (1.20), (1.21)). This produces a parametrization of the PDFs at all $x$ and $Q^2$ values, which can then be used to characterize the structure functions and calculate cross sections. Since the predicted cross sections must match all existing lepton-hadron and hadron-hadron data, a global fit is performed in order to determine the best values of the initial free parameters of the PDFs.

We will briefly summarize the characteristics of the most commonly used PDF's.

### 1.10.1 MRS parametrizations

The Martin-Roberts-Stirling (MRS) parametrizations are obtained from a global next-to-leading order (NLO) QCD fit, including DIS data from BCDMS, EMC, NMC and CCFR. Their starting $Q^2$ value is $Q_o^2 = 4$ GeV$^2$.

The NMC measurement of the Gottfried Sum Rule (GSR) is incorporated in the MRSD' parametrizations[24] using a flavor asymmetric sea. The GSR predicts the difference between the proton and neutron structure functions as:

$$I_{GSR} \equiv \int_0^1 \frac{dx}{x}(F_2^p - F_2^n) = \frac{1}{3}\int_0^1 dx(u_V - d_V) + \frac{2}{3}\int_0^1 dx(\bar{u} - \bar{d}) \qquad (1.47)$$

A flavor symmetric sea ($\bar{u} = \bar{d}$) would yield: $I_{GSR} = \frac{1}{3}$. The NMC measurement is[25]:

$$I_{GSR}(NMC) = \int_{0.004}^{0.8} \frac{dx}{x}(F_2^p - F_2^n) = 0.227 \pm 0.007(stat) \pm 0.014(sys) \quad (1.48)$$

which indicates that $\bar{u} < \bar{d}$. Hence, the initial sea-quark distributions at $Q_o^2$ for the MRSD' parametrizations were given the form:

$$2\bar{u} = 0.4S - \Delta \qquad (1.49)$$

$$2\bar{d} = 0.4S + \Delta \qquad (1.50)$$

$$2\bar{s} = 0.2S \qquad (1.51)$$

where $S(x)$ is the total sea-quark distribution and $\Delta$ is a non-zero distribution which reproduces the NMC data. The strange quark distribution is suppressed compared to the $\bar{u}$ and $\bar{d}$ distributions, according to experimental evidence from CCFR.[26] The charm and bottom quark distributions are set to zero at $Q_o^2$ and generated dynamically at higher $Q^2$, using the GLAP evolution equations.

The gluon and sea quark distributions at low $x$ are parametrised with the same function: $xf \sim x^{-\lambda}$, at $Q^2 = Q_o^2$. Since the pre-HERA data did not restrict the value of $\lambda$, the MRS group produced two sets of parametrizations using two extreme values: the MRSD$'_0$, which has a constant gluon/sea distribution, with $\lambda = 0$, and the MRSD$'_-$, with a singular gluon/sea, with $\lambda = \frac{1}{2}$.



A subsequent parametrization of the MRS group, called MRSH,[27] includes the 1992 HERA data along with the previous fixed target experiments in the global QCD fit. This set has also a singular gluon and sea quark distribution at $Q_o^2 = 4$ GeV$^2$, with $\lambda = 0.3$.

The 1993 HERA data, presented in this thesis, are incorporated in the MRSA, MRSA' and MRSG sets.[28] A preliminary form of the 1993 $F_2$ measurement is included in the MRSA fit, which otherwise follows the line of MRSH. The final 1993 results are used in the MRSA' and MRSG sets. In MRSA' the usual assumption of the same singular behavior of the sea and gluon distributions is made, with $\lambda \equiv \lambda_S = \lambda_g = 0.17$. In MRSG the sea and gluon exponents are allowed to vary independently, and the fit yields a steeper gluon, $\lambda_g = 0.30$, and a flatter sea, $\lambda_S = 0.07$.

### 1.10.2 CTEQ parametrizations

The CTEQ group (Coordinated Theoretical/Experimental Project on QCD) also performs a NLO global QCD fit. They allow a flavor asymmetric sea, and have a singular gluon behavior at low $x$: $xg \sim x^{-\lambda_g}$, at $Q^2 = Q_o^2$.

The initial CTEQ1 parametrization[29] used data from BCDMS, NMC and CCFR, with reference $Q^2$ value for the GLAP evolution equal to $Q_o^2 = 4$ GeV$^2$, and with $\lambda_g = \frac{1}{2}$. There was no strange quark suppression: the $u$, $d$ and $s$ distributions were parametrized independently.

The subsequent CTEQ2 set[30] includes the 1992 HERA data in the QCD fit, starting at $Q_o^2 = 1.6$ GeV$^2$. The strange quark suppression is incorporated in the CTEQ2 set. The QCD fit yields a value of $\lambda_g = 0.21$.

The 1993 HERA data are included in the CTEQ3 set,[31] which starts the

QCD evolution at $Q_o^2 = 1.6$ GeV$^2$ and yields $\lambda_g = 0.33$.

### 1.10.3 GRV parametrizations

An alternative approach to Parton Distribution Functions is used by Glück, Reya, and Vogt.[32]

They start with valence-like parton (gluon, valence and $\bar{u} = \bar{d}$ sea quark) distributions, at a very low reference scale of $Q_o^2 = 0.3$ GeV$^2$ and demand $xq(x, Q_o^2) \to 0$ as $x \to 0$. Strange, as well as charm and bottom, sea quark distributions at $Q_o^2$ are set to zero. All parton distribution functions are then evolved to higher values of $Q^2$ using the GLAP equations.

This dynamically generated growth of the PDFs predicts a fast rise in $F_2$ at low values of $x$.

The most recent set from the GRV group, called GRV94,[33] adopts a factorization scheme in which the heavy quarks c, b,... are not included among the intrinsic (massless) parton distributions in the proton.



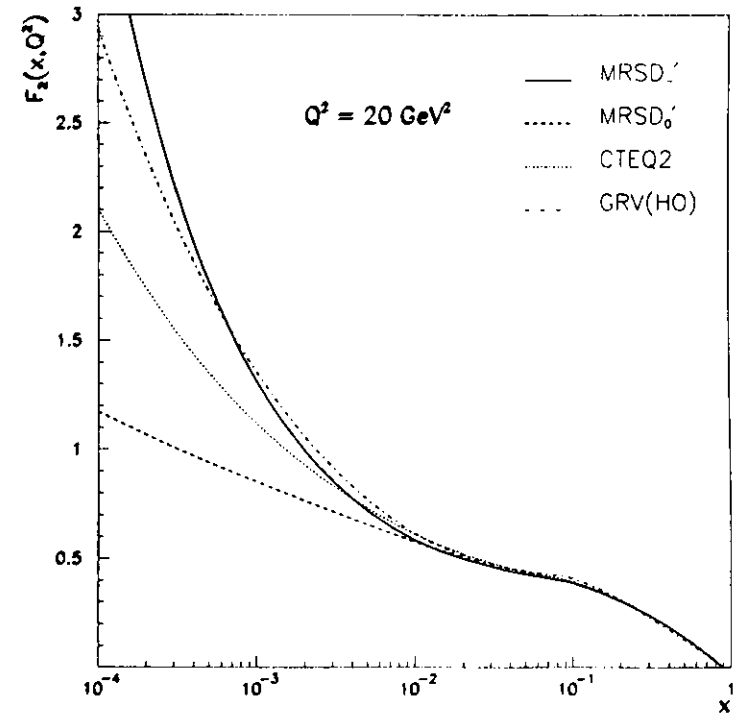


Figure 1.1: *Various parametrizations of $F_2$ as a function of $x$ at $Q^2 = 20$ GeV$^2$.*

# Chapter 2

# HERA and ZEUS

## 2.1 The HERA electron-proton Collider

HERA, the first electron-proton collider, is located at the DESY (Deutsches Electronen Synchrotron) laboratory, in Hamburg, Germany. It is designed to accelerate 30 GeV electrons (or positrons) and 820 GeV protons, yielding a center-of-mass energy $\sqrt{s} = 314$ GeV. Four interaction points are available: two of them are occupied by the H1 and ZEUS detectors, the third is used by the spin-physics fixed target experiment HERMES, while the fourth will be occupied by the HERA-B detector, currently under construction. The layout of the accelerator is shown in fig. 2.1, while its main parameters are listed in table 2.1.

The electrons are pre-accelerated with a linear accelerator (LINAC II) and then with the DESY II and PETRA II, reaching energies of 500 MeV, 7 GeV and 11 GeV, respectively, before being injected into HERA. For the proton beam, $H^-$ ions are accelerated in a linac, then the electrons are stripped and the protons are pre-accelerated with DESY III and PETRA II, to 7.5 and 40 GeV, respectively. From there they are injected into HERA.

Both beams are divided in bunches, in order to increase the frequency of the



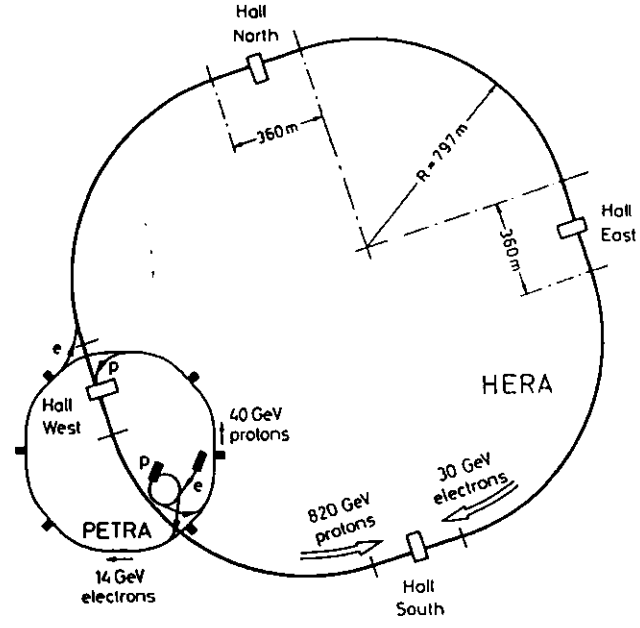


Figure 2.1: *The HERA collider*

| HERA parameters | Design values | | 1993 | |
|---|---|---|---|---|
| | electron | proton | electron | proton |
| Energy (GeV) | 30 | 820 | 26.7 | 820 |
| Luminosity ($cm^{-2}s^{-1}$) | $1.5 \cdot 10^{31}$ | | $1.8 \cdot 10^{30}$ | |
| Circumference (m) | 6336 | | | |
| Magnetic Field (T) | 0.165 | 4.65 | | |
| Energy range (GeV) | 10-33 | 300-820 | | |
| Injection Energy (GeV) | 14 | 40 | | |
| Circulating Current (mA) | 58 | 163 | 7-20 | 7-15 |
| Number of bunches | 210 | | 81 + 10 | 81 + 6 |
| Time Between Crossing (ns) | 96 | | 96 | |
| Horizontal Beam Size $\sigma_x$ (mm) | 0.26 | 0.29 | | |
| Vertical Beam Size $\sigma_y$ (mm) | 0.07 | 0.07 | | |
| Longit. Beam Size $\sigma_z$ (mm) | 0.8 | 11 | | |
| Filling Time (min) | 15 | 20 | 45 | 60 |
| Energy Lost per Turn (MeV) | 127 | $1.4 \cdot 10^{-10}$ | | |

Table 2.1: *Design values of HERA parameters and 1993 running values.*



crossing per unit time. A small number of $e/p$-bunches, usually called pilot bunches, are unpaired with each-other (i.e. do not collide) and are used to estimate the background produced by interactions of the beams with residual gas in the beam-pipe (see section 5.10.1). In the 1993 run there were 84 colliding $e/p$-bunches, 10 unpaired $p$-bunches, and 6 unpaired $e$-bunches.

The collision between the two beams occurs at zero crossing angle. The z-width of the collision region is in principal determined by the length of the proton and electron bunches. In practice, however, the collision region is mainly determined by the proton bunch length, since this is much greater than the electron bunch length. In the 1993 run the root-mean-square of the proton bunch length was about $\pm 20$ cm.

It should be noted here that HERA differs from all previous colliders in the asymmetric beam energies, which boost the center-of-mass system towards the proton beam direction, and the very small beam crossing interval (96 ns). The first characteristic requires the H1 and ZEUS detectors to have asymmetric geometry, while the second condition requires very fast trigger and read-out systems.

## 2.2 The ZEUS Detector

The ZEUS detector[31] is a multi-purpose detector designed to achieve the best possible energy measurement of electrons and jets in DIS Neutral Current (NC) and Charged Current (CC) events. It is asymmetric along the beam direction, to account for the boosted center-of-mass at HERA. It is a hermetic detector (except for the beam-pipe hole), which is crucial for the study of CC

events.

The ZEUS coordinate system is a right-handed orthogonal coordinate system with the origin at the nominal interaction point, the positive (negative) z-axis in the proton (electron) beam direction, the positive x-axis towards the center of the HERA ring, and the positive y-axis in the upward direction. The polar angle $\theta$ of the scattered electron is measured with respect to the positive z-axis, and the azimuthal angle $\phi$ is measured relative to the positive x-axis.

The layout of the ZEUS detector is shown in fig. 2.2. It consists of (proceeding outwards from the interaction point):

- the Inner Tracking System: Vertex Detector (VXD), Cental Tracking Detector (CTD), Forward and Rear Tracking Detectors (FDET and RTD), and the magnetic coil (Solenoid);
- the Calorimeter: Forward, Barrel and Rear Calorimeter (FCAL, BCAL and RCAL);
- the Hadron-Electron Separator (HES) (not shown in the picture);
- the Backing Calorimeter (BAC), which absorbs and detects energy leakage of the Calorimeter;
- Muon Detectors: Forward, Barrel and Rear Muon chambers (FMUON, BMUON and RMUON);
- the C5 counter and the Veto wall (not shown in the picture), which detect particles entering the detector from the rear direction.
- Luminosity monitor



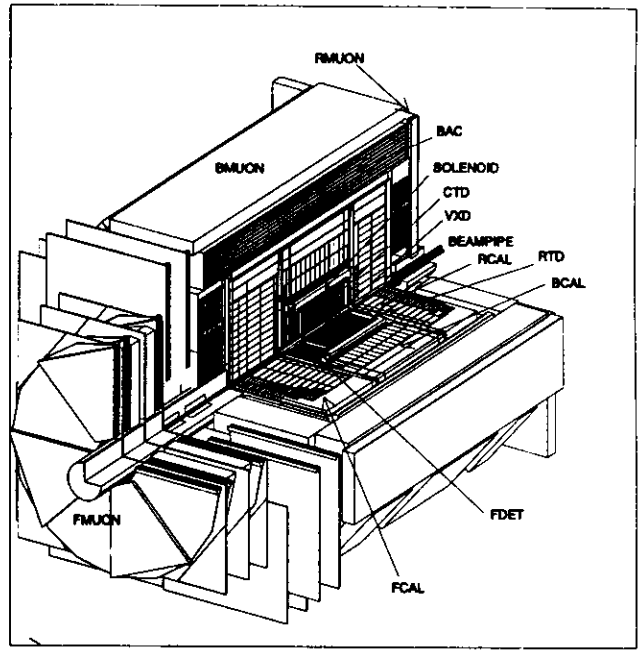


Figure 2.2: *The ZEUS detector.*

The ZEUS detector components used in this analysis are described in the following sections.

### 2.2.1 The Inner Tracking System

The ZEUS tracking system consists of a set of cylindrical drift chambers in the central region, called the Vertex Detector (VXD) and the Cental Tracking Detector (CTD), planar drift chambers and transition radiation detectors (FDT and TRD) in the forward region and a planar drift chamber (RTD) in the rear region. During the 1993 HERA run, only the central tracking system (VXD and CTD) was functioning.

The VXD is a cylindrical drift chamber placed immediately around the beampipe, with a length of 160 cm, an inner radius of 88 mm and an outer radius of 162 mm. During the 1993 data taking, it achieved a spatial resolution of 50 $\mu$m in the central region and 150 $\mu$m around the edges. It is used in the event vertex reconstruction.

The CTD is also a cylindrical drift chamber surrounding the VXD. It has a length of 240 cm, an inner radius of 17 cm, an outer radius of 85 cm, and covers polar angles $\theta$ from 15° to 164°. It consists of 72 cylindrical drift chamber layers, organized into 9 superlayers. During the 1993 data taking, the CTD achieved a spatial resolution of 260 $\mu$m, yielding a resolution in transverse momentum $\sigma(p)/p = 0.005p \oplus 0.016$, for tracks that traverse all superlayers. The CTD is used in the reconstruction of the tracks of charged particles, and, along with the VXD, in the event vertex reconstruction.

The magnetic field, of 1.43 Tesla, is provided by a superconducting solenoid that surrounds the CTD.



### 2.2.2 The Calorimeter

The ZEUS calorimeter is a high resolution uranium-scintillator compensating calorimeter. It consists of alternating layers of depleted[1] uranium (at a thickness of 1 radiation length = 3.3 mm), as absorber, and scintillator (2.6 mm thick), for readout purposes. The use of uranium helps to increase the response to hadrons. The ratio of scintillator thickness to absorber thickness has been chosen so that the calorimeter has an equal response to electrons and hadrons ($e/h = 1$), and a high energy resolution for hadrons and jets. The measured energy resolution of the ZEUS calorimeter is

$\sigma(E)/E = 0.35/\sqrt{(E)}$, for hadrons

$\sigma(E)/E = 0.18/\sqrt{(E)}$, for electrons.

The layout of the calorimeter is shown in fig. 2.3. It completely surrounds the tracking detectors and the solenoid. Mechanically it is divided in three overlapping parts, covering three polar regions:

- the forward calorimeter (FCAL), covering polar angles
  $2.2° \leq \theta \leq 39.9°$,
- the barrel calorimeter (BCAL), covering polar angles
  $36.7° \leq \theta \leq 129.1°$,
- the rear calorimeter (RCAL), covering polar angles
  $128.1° \leq \theta \leq 176.5°$.

With the exception of holes of $20 \times 20$ cm$^2$, in the center of FCAL and RCAL, which are necessary to accomodate the HERA beampipe, the calorimeter is hermetic.

[1] An alloy of 98.4% $U^{238}$, 1.4% Nb, and less than 0.2% $U^{235}$.

The structure of the three calorimeter parts is similar. They are subdivided longitudinally into modules, which in turn are subdivided into towers of approximate transverse dimensions $20 \times 20$ cm$^2$. Each tower is segmented longitudinally into an electromagnetic (EMC) and one (in RCAL) or two (in FCAL and BCAL) hadronic (HAC1,2) sections. The EMC sections consist of four $5 \times 20$ cm$^2$ cells in FCAL and BCAL, and two $10 \times 20$ cm$^2$ cells in RCAL. The HAC sections are cells on their own. Each calorimeter cell is read out on two opposite sides by two photomultiplier tubes (PMTs), to achieve a more accurate position measurement within the cell. The EMC section has a depth of approximately 25 radiation lengths ($X_o$), or 1 absorption length ($\lambda$). The total HAC sections in FCAL/BCAL/RCAL are $6\lambda$, $4\lambda$ and $3\lambda$ deep, respectively.

The calorimeter also provides accurate timing information. The total time of a calorimeter section (F/B/RCAL) is obtained from an energy weighted average of the times of all PMTs with energy deposits greater than 200 MeV. The timing information is very useful for background rejection.



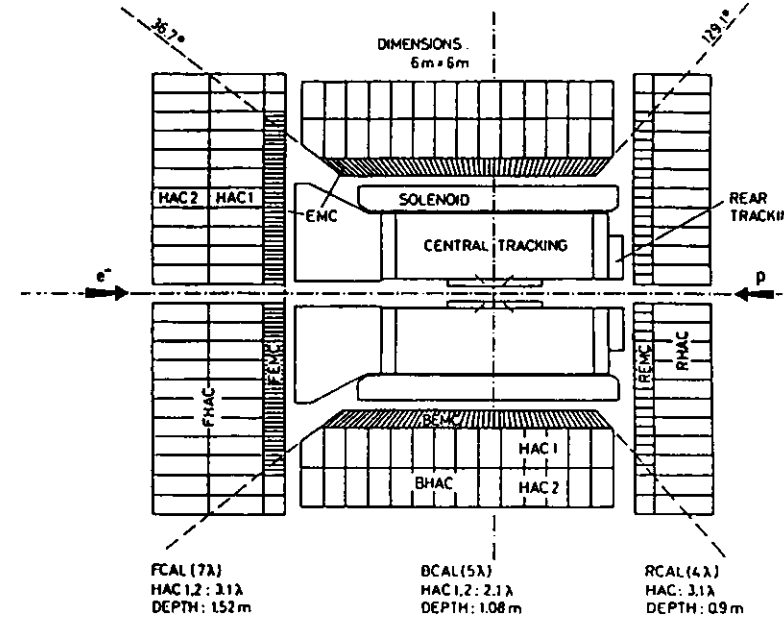


Figure 2.3: *Side view of the ZEUS calorimeter.*

### 2.2.3 The Hadron-Electron Separator (HES)

In order to achieve a more accurate electron identification and electron position reconstruction, a plane of $3 \times 3$ cm$^2$ silicon diodes has been inserted at 3.3 radiation lengths inside the RCAL. This device is called the Hadron Electron Separator (HES) because at this depth electromagnetic showers give a large signal in one or more HES diodes, while hadrons, which typically interact at greater depths, behave like minimum ionizing particles in the HES.

### 2.2.4 The C5 Counter and the Veto Wall

The C5 beam monitor is a scintillator counter positioned around the beampipe, at $z = -3.15$ m upstream of the interaction point. It is used to reject proton beam-gas background events, and to measure the beam arrival times.

The Veto wall is an iron wall located at $z = -7.5$ m upstream of the interaction point. Its main main purpose is to protect the main detector from beam halo particles accompanying the proton beam. The iron wall has a thickness of 87 cm and is covered on both sides with scintillator counters, which are used to tag penetrating particles from background interactions.

### 2.2.5 The Luminosity Monitor and Measurement

The $ep$ luminosity is measured by the luminosity monitor using the rate of the hard bremsstrahlung photons produced in the Beithe-Heitler process $e p \rightarrow e' p \gamma$. This process has been chosen because of its large and precisely known cross section, and its well defined experimental signature.



The luminosity monitor consists of two scintillator calorimeters that measure the scattered electron and the radiative photon, and are placed at $z = -35$ m and $z = -106$ m, respectively. Both the scattered electron and the radiative photon are emitted at very small angles with respect to the initial electron direction. The LUMI-$e$ calorimeter detects electrons emitted at scattering angles $\theta_e \leq 6$ mrad and with energies between $0.2E_e$ and $0.9E_e$, $E_e$ being the electron beam energy. The LUMI-$\gamma$ calorimeter detects photons at angles $\theta_\gamma \leq 0.5$ mrad. The sum of the energy deposits in the LUMI-$e$ and LUMI-$\gamma$ counters is equal to the electron beam energy.

A significant background in the luminosity measurement comes from bremsstrahlung of the beam electrons on the residual gas in the beampipe, $eA \rightarrow e'A\gamma$. The rate of this background is estimated using the electron pilot bunches: the bremsstrahlung rate from the electron pilot bunches, is weighted with the ratio of the total electron colliding bunch current to the electron pilot bunch current, and the estimated rate of total electron-gas bremsstrahlung photons is subtracted from the total measured rate of photons. The instantaneous (integrated) luminosity is obtained from the corrected rate (number) of photons, using by the theoretical cross section of the Beithe-Heitler process.

The integrated luminosity delivered by HERA in 1993 was 1088 nb$^{-1}$, while ZEUS wrote on tape 600 nb$^{-1}$. Both the HERA delivered and ZEUS accumulated luminosity during the 1993 running period are shown in fig. 2.4.

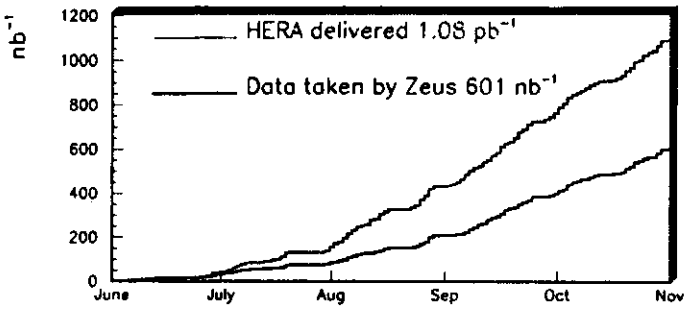


Figure 2.4: *HERA delivered and ZEUS accumulated luminosity during the 1993 run.*

### 2.2.6 Trigger and Data Acquisition Systems

ZEUS uses a sophisticated trigger and read-out system, to enable operation with the very short beam crossing interval of HERA (96 ns). $ep$ physics events in the ZEUS detector are written to tape at a rate of a few Hz. However, background from interactions of the proton beam with residual gas in the beampipe has a much higher rate, on the order of 100 kHz, which has to be reduced by the trigger system. In addition, background events from electron beam-gas interactions, beam halo, and cosmic rays, have to be rejected. The trigger system is organized in three levels.

The First Level Trigger (FLT) system is a hardware trigger, designed to reduce the input rate below 1 kHz. Each detector component has its own FLT, which stores the data in a pipeline, and makes a trigger decision within 2 $\mu$s



after the bunch crossing. The decisions from the local FLTs are passed to the Global First Level Trigger (GFLT), which decides whether to accept or reject the event, and returns this decision to the component readout within 5 $\mu$s.

If the event is accepted, the data are transferred to the Second Level Trigger (SLT), which is software-based and runs on a network of Transputers. It is designed to reduce the rate below 100 Hz, using mainly timing cuts. Each component can also have its own SLT, which passes a trigger decision to the Global Second Level Trigger (GSLT). The GSLT then decides on accepting or rejecting the event.

If the event is accepted by the GSLT, all detector components send their data to the Event Builder (EVB), which produces an event structure on which the Third Level Trigger (TLT) code runs. The TLT is also software-based, runs on a farm of Silicon Graphics CPU's, and is designed to reduce the rate to a few Hz.

Events accepted by the TLT are written to tape.

The ZEUS trigger and data acquisition system is shown in fig. 2.5.

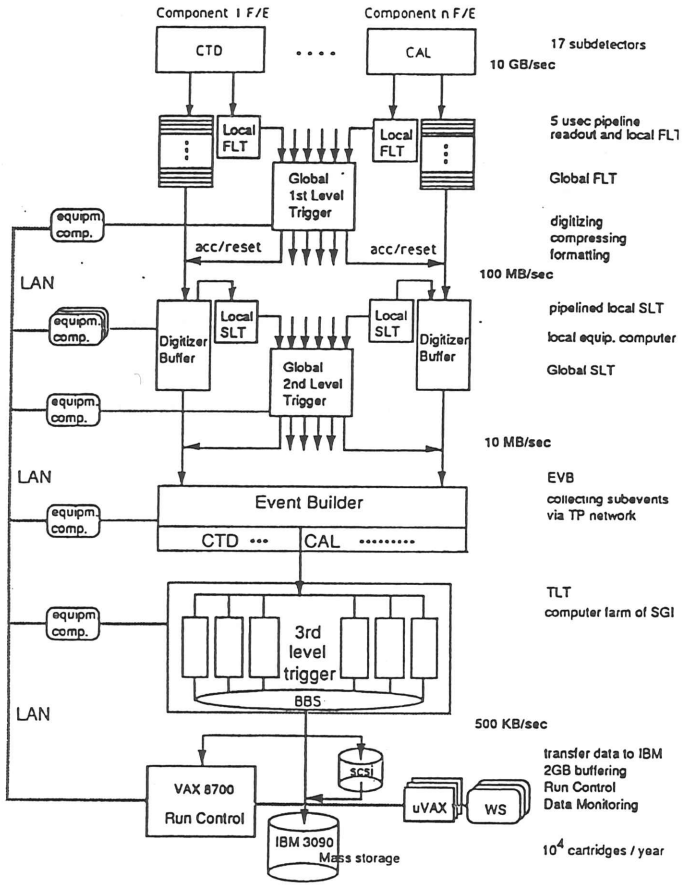


Figure 2.5: *The ZEUS trigger and data acquisition system.*



# Chapter 3

# Monte Carlo Simulation

Monte Carlo (MC) simulation is used to correct for reconstruction resolution, detector and selection acceptance effects.

The MC sample used in this analysis has been produced with the following generators.

HERACLES 4.1[35] is used to simulate neutral current deep inelastic $ep$ collisions. It includes first order electroweak radiative corrections.

The DIS NC cross section is generated using MRSD'_ (see section 1.10.1) as the input structure function, since it shows the best agreement with the 1992 HERA data.

In order to simulate the hadronic final state, a model for the QCD cascade and a model for the hadronisation process are required. The QCD cascade (i.e. development of the parton shower) is simulated using the Color Dipole Model (CDM),[36] as implemented in ARIADNE 3.1,[37] and includes Boson Gluon Fusion (BGF). The Color Dipole Model treats gluons as radiation from the color dipole formed between the struck quark and the proton remnant, rather than from individual partons. The Boson Gluon Fusion process, where it is possible that both a quark and an antiquark create one dipole each with the remnant, is not satisfactorily described by the CDM, and has been added

separately. The hadronisation process is simulated using the LUND string model,[38] as implemented in JETSET 6.3.[39] According to this model, as the struck quark moves away from the proton remnant, the color flux tube, which can be thought of as a massless relativistic string, is being stretched between the partons. Assuming uniform energy density, the potential energy stored in the string increases, the string may break into shorter fragments, and hadrons are formed by the (anti)quarks from adjacent breaks.

The output of the MC generators described above is a set of momentum 4-vectors of the final state particles. These are then passed through the simulation of the ZEUS detector, which is based on GEANT 3.13,[40] and the simulation of the ZEUS trigger system. Finally, the MC events are also passed through the reconstruction program identical to the one used for the data.

The main DIS NC Monte Carlo sample consists of 300k events, corresponding to an integrated luminosity of 738 $nb^{-1}$. It has been generated with $Q^2 > 4$ $GeV^2$, which is the lowest cutoff of the input structure function.

In addition to the main DIS Monte Carlo, two other MC samples are used for background studies and radiative corrections.

Approximately 150k photoproduction background events (see section 5.5.4) have been generated with $0 < Q^2 < 2$ $GeV^2$, at high $y$ ($y > 0.6$), using the PYTHIA 5.6[41] program. They are used for statistically estimating the photoproduction background in the final DIS sample (see section 5.10.2).

A sample of 100k DIS events with only the Born cross section included has been generated with the LEPTO 6.1[42] program. It is used for correcting the measured DIS cross section due to radiative processes (see section 8.3).



# Chapter 4

# Reconstruction of Kinematics

## 4.1 Reconstruction Methods

An accurate reconstruction of the Lorentz-invariant variables $x$, $y$ and $Q^2$ is of crucial importance for the measurement of the proton structure functions.

In inclusive Neutral Current Deep Inelastic $ep$ Scattering the final state consists of the scattered electron and the final state hadron flow. The latter originates from the fragmented struck quark, which produces the "current" jet, and the remaining diquark, which gives rise to the "remnant" or "spectator" jet. The scattered electron and the current jet emerge back to back in azimuthal direction and balance each other in transverse momentum. The remnant jet is emitted in the forward direction (that of the initial proton), and escapes mostly unobserved down the beam-pipe.

We denote by $\mathbf{k}_e$ and $\mathbf{k}'_e$ the momentum 4-vectors of the initial and scattered electron, respectively, $\mathbf{P}$ the 4-vector of the initial state proton, and $\mathbf{P}'$ the 4-vector of the final state hadron flow. In the ZEUS coordinate system, where the direction of the initial proton is defined as the positive $z$ axis, and neglecting all particle masses, the 4-momenta of the initial and final state particles can

be written as:

$$\mathbf{k_e} = \begin{pmatrix} E_e \\ 0 \\ 0 \\ -E_e \end{pmatrix}, \mathbf{k'_e} = \begin{pmatrix} E \\ E\sin\theta\cos\phi \\ E\sin\theta\sin\phi \\ E\cos\theta \end{pmatrix}, \mathbf{P} = \begin{pmatrix} E_p \\ 0 \\ 0 \\ E_p \end{pmatrix}, \mathbf{P'} = \begin{pmatrix} E_h \\ P_{xh} \\ P_{yh} \\ P_{zh} \end{pmatrix}, \tag{4.1}$$

where $E_e$ and $E_p$ are the energies of the initial electron and proton, respectively, $E$, $\theta$, $\phi$ are the energy, polar angle and azimuthal angle of the scattered electron, and $E_h$ is energy of the total hadronic system, where a summation over all particles in the final state is assumed.

In order to reconstruct the event kinematics we can use either the final state electron, or the hadron flow, or both. In the first case we use the scattered electron energy $E$ and polar angle $\theta$. In the case of the hadron flow we need to be careful that the extracted variables are independent of the final state fragmentation and insensitive to particle losses along the forward beam direction. The transverse momentum of the hadron system, $P_{Th}$, and the difference between the energy and the $z$-momentum of the hadron flow, $(E - P_z)_h$, satisfy these requirements. The remnant jet contributes very little to the above variables, as it is lost in the direction of the beam-pipe. We can then assume that the hadron flow (in effect, the current jet) can be described by a massless object, whose energy $E_j$ and direction $\cos\gamma$ can be reconstructed from the quantities $(E - P_z)_h$ and $P_{Th}$. In the naive quark model, $E_j$ and $\gamma$ are the energy and polar angle of the struck quark.

The kinematics of the event, $x$, $y$ and $Q^2$, are extracted using any two of the four parameters that describe the final state electron and hadron flow, $\{E, \theta, E_j, \gamma\}$. The various reconstruction methods obtained from the possible combinations have a different response to detector effects and vary in accuracy, depending also on kinematic regions, as explained below. The methods used in this analysis are discussed in the following sections.



### 4.1.1 Electron method

Using the definitions of the Lorentz-invariant variables $x$, $y$, $Q^2$ and $s$ (eqs. 1.4, 1.6, 1.7, 1.3), and the momentum 4-vectors from eq. (4.1), we obtain the event kinematics in terms of the energy $E$ and the angle $\theta$ of the final state electron:

$$Q^2_{elec} = 2E_e E(1+\cos\theta) = 4E_e E\cos^2\frac{\theta}{2} \tag{4.2}$$

$$y_{elec} = 1 - \frac{E}{2E_e}(1-\cos\theta) = 1 - \frac{E}{E_e}\sin^2\frac{\theta}{2} \tag{4.3}$$

$$x_{elec} = \frac{Q^2_{elec}}{s\, y_{elec}} = \frac{E\cos^2\frac{\theta}{2}}{E_p\left[1 - \frac{E}{E_e}\sin^2\frac{\theta}{2}\right]} \tag{4.4}$$

where $s$ is given by eq. (1.16). We call this method of reconstruction the Electron method.

Substituting either $\theta$ or $E$ from eq. (4.4) into eq. (4.2), we obtain the equations of contours of constant scattered electron energy and angle, respectively, for the electron method:

$$Q^2(x,E) = \frac{sx\left(1 - \frac{E}{E_e}\right)}{1 - \frac{xE_p}{E_e}} \tag{4.5}$$

$$Q^2(x,\theta) = \frac{sx}{1 + \frac{xE_p}{E_e}\tan^2\frac{\theta}{2}} \tag{4.6}$$

The scattered electron energy and angle isolines in the $(x, Q^2)$ phase space are

shown in fig. 1.1. The dashed lines represent lines of constant $y$ values at 1., 0.1 and 0.01. The resolution in $x$ and $Q^2$ is in general good in regions of phase space where the $E$ and $\theta$ isolines are close together, whereas for isolines far apart, small errors in the measurement of $E$ and $\theta$ produce large uncertainties in $x$ and $Q^2$. As can be seen from fig. 4.1a, the resolution of the electron method is good for low values of $x$, which also correspond to low values of the scattered electron energy $E$. At higher values of $x$, the energy isolines become distant, which means that small errors in the electron energy measurement produce large uncertainties in the determination of $x$. In fig. 4.1b the lines at 36.7° and 129.1° represent the boundaries between FCAL-BCAL and BCAL-RCAL, respectively. The RCAL beam hole (for $\theta \geq 176.5°$) sets a lower acceptance limit for $Q^2$ at approximately 2 GeV$^2$. The resolution in $Q^2$, as determined from the electron angle $\theta$, is independent of $x$, and becomes better for higher values of $Q^2$.

The dependence of the reconstructed $x_{elec}$ and $Q^2_{elec}$ on the measurement errors of the scattered electron energy $E$ and angle $\theta$ is given by:

$$\frac{\Delta x_{elec}}{x_{elec}} = \sqrt{\left(\frac{1}{y}\right)^2 \left(\frac{\Delta E}{E}\right)^2 + \left[-\tan\frac{\theta}{2} + \left(\frac{1}{y} - 1\right)\cot\frac{\theta}{2}\right]^2 (\Delta\theta)^2} \qquad (4.7)$$

$$\frac{\Delta Q^2_{elec}}{Q^2_{elec}} = \sqrt{\left(\frac{\Delta E}{E}\right)^2 + \tan^2\frac{\theta}{2}\,(\Delta\theta)^2} \qquad (4.8)$$

As can be seen from eq.(4.7), the resolution in $x$ is good for high $y$ values, whereas it deteriorates with decreasing $y$, due to the $1/y$ factor that amplifies the error of the energy measurement. The resolution in $Q^2$ is good, except at



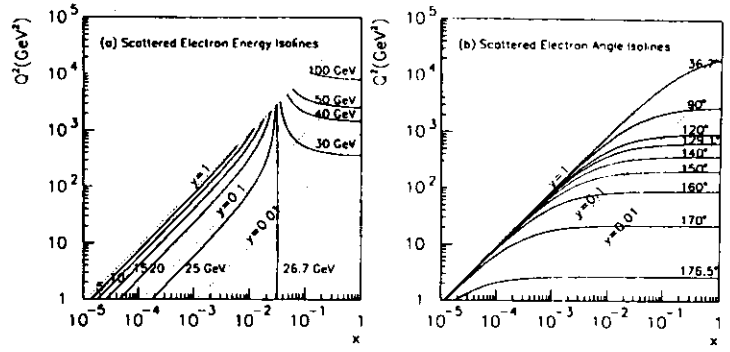


Figure 4.1: *Contours of constant scattered electron (a) energy and (b) angle, for initial electron and proton energies $E_e = 26.7GeV$ and $E_p = 820GeV$.*

large electron scattering angles $\theta$, where the error in the angle measurement becomes the dominant term in eq.(4.8).

### 4.1.2 Current Jet and Jacquet-Blondel method

The event kinematics could in principle be reconstructed from the current jet, which originates from the struck quark, using its energy $E_j$ and angle $\gamma$. However, in order to avoid effects arising from the final state fragmentation, the particle losses along the beam-pipe, and the separation between the current and remnant jets, we use the quantities $P_{Th}$ and $(E - P_z)_h$, as discussed in section (4.1). The reconstruction method of the HERA kinematics based on the above quantities was developed by Jacquet and Blondel. [13]

Since the remnant jet is lost in the forward direction of the beam-pipe, the

transverse momentum $P_{Th}$ and the difference $(E-P_z)_h$ of the hadron flow are approximately equal to those of the current jet, $P_{Tj}$ and $(E-P_z)_j$:

$$P_{Th} \sim P_{Tj} = E_j \sin\gamma \tag{4.9}$$

$$\sum_h (E-P_z)_h \sim (E-P_z)_j = E_j(1-\cos\gamma) = 2E_j \sin^2\frac{\gamma}{2} \tag{4.10}$$

where:

$$P_{Th} = (\sum_h P_{xh})^2 + (\sum_h P_{yh})^2 \tag{4.11}$$

and the sums over $h$ run over all final state hadrons.

We determine $Q^2$ at the hadron vertex:

$$Q^2 = -q^2 = -(P_j - xP)^2, \tag{4.12}$$

where $xP$ and $P_j$ are the 4-momenta of the struck quark and the current jet, respectively.

Using the definition for $y$ from eq.(1.7), we obtain:

$$y_{JB} = \frac{E_j}{E_e}\sin^2\frac{\gamma}{2} = \frac{\sum_h (E-P_z)_h}{2E_e} \tag{4.13}$$

From the electron method we calculate:

$$Q^2_{elec}(1-y_{elec}) = P^2_{T\,elec} \tag{4.14}$$

A similar equation must hold for the hadron flow, because of conservation of transverse momentum. Thus:

$$Q^2_{JB} = \frac{P^2_{Th}}{1-y_{JB}} = \frac{E_j^2 \sin^2\gamma}{1-\frac{E_j}{E_e}\sin^2\frac{\gamma}{2}} \tag{4.15}$$

Finally, $x_{JB}$ is given by:

$$x_{JB} = \frac{Q^2_{JB}}{s\,y_{JB}} = \frac{E_j\cos^2\frac{\gamma}{2}}{E_p\left(1-\frac{E_j}{E_e}\sin^2\frac{\gamma}{2}\right)} \tag{4.16}$$



The Jacquet-Blondel method does not make any assumption about the internal structure of the proton. It also makes no distinction between hadrons coming from different jets. Thus, it works equally well for multijet events, without any need for exact jet definition and separation.

The contours of constant scattered jet energy and angle for the Jacquet-Blondel method are given by:

$$Q^2(x,E_j) = \frac{sx\left(1-\frac{E_j}{xE_p}\right)}{1-\frac{E_j}{xE_p}} \tag{4.17}$$

$$Q^2(x,\gamma) = \frac{sx}{1+\frac{E_j}{xE_p}\cot^2\frac{\gamma}{2}} \tag{4.18}$$

The scattered jet energy and angle isolines in the $(x,Q^2)$ phase space are shown in fig. 4.2. In contrast to the electron method, resolution in $x$, as determined from the scattered jet energy, is good at high values of $x$, whereas it deteriorates for lower $x$. On the other hand, the forward beam hole ($\gamma < 2.2^\circ$) sets an acceptance limit for the measurement and use of the scattered jet at high values of $x$ and low values of $y$.

The dependence of $x_{JB}$ and $Q^2_{JB}$ on the measurement errors of the scattered jet energy $E_j$ and angle $\gamma$ is given by:

$$\frac{\Delta x_{JB}}{x_{JB}} = \sqrt{\left(\frac{1}{1-y}\right)^2\left(\frac{\Delta E_j}{E_j}\right)^2 + \left[-\tan\frac{\gamma}{2} + \frac{y}{1-y}\cot\frac{\gamma}{2}\right]^2(\Delta\gamma)^2} \tag{4.19}$$

$$\frac{\Delta Q^2_{JB}}{Q^2_{JB}} = \sqrt{\left(\frac{2-y}{1-y}\right)^2\left(\frac{\Delta E_j}{E_j}\right)^2 + \left[2\cot\gamma + \frac{y}{1-y}\cot\frac{\gamma}{2}\right]^2(\Delta\gamma)^2} \tag{4.20}$$

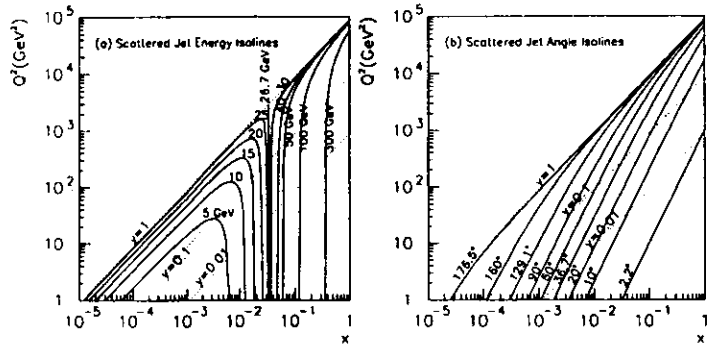


Figure 1.2: *Contours of constant scattered jet (a) energy and (b) angle, for initial electron and proton energies* $E_e = 26.7GeV$ *and* $E_p = 820GeV$.

The resolution in $x$ for low $y$ values depends only on the scattered jet energy measurement. At high $y$, the resolution in $x$ becomes poor, due to the $1/(1-y)$ factor, in contrast to the electron method. The $Q^2$ resolution also deteriorates with increasing $y$. The resolution in $x$ is poor at both low and high values of $\gamma$, whereas the resolution in $Q^2$ is affected by the error of the scattered jet angle measurement only at low values of $\gamma$.

### 4.1.3 Double Angle method

In the Double Angle method, $x$, $y$ and $Q^2$ are reconstructed using the scattering angles $\theta$ and $\gamma$ of the final state electron and the final state hadron flow, respectively. There is no direct dependence on energy scales.

The scattering angle $\gamma$ of the struck quark is obtained from the hadronic



flow measurement. Inverting eqs. (1.13) and (1.15) that give $y_{JB}$ and $Q^2_{JB}$ as functions of $E_j$ and $\gamma$, we obtain:

$$\cos\gamma = \frac{Q^2_{JB}(1-y_{JB}) - 4E_e^2 y^2_{JB}}{Q^2_{JB}(1-y_{JB}) + 4E_e^2 y^2_{JB}} \tag{1.21}$$

Substituting $y_{JB}$ and $Q^2_{JB}$ in terms of $P_{Th}$ and $(E-P_z)_h$ yields:

$$\cos\gamma = \frac{(\sum_h P_{xh})^2 + (\sum_h P_{yh})^2 - (\sum_h (E-P_z))^2}{(\sum_h P_{xh})^2 + (\sum_h P_{yh})^2 + (\sum_h (E-P_z))^2} \tag{1.22}$$

The energy of the final state electron can be expressed in terms of the angles $\theta$ and $\gamma$. Conservation of energy, longitudinal momentum, and transverse momentum, on the quark level, result in the following relations:

$$xE_p + E_e = E + E_j \tag{1.23}$$

$$xE_p - E_e = E\cos\theta + E_j\cos\gamma \tag{1.24}$$

$$E\sin\theta = E_j\sin\gamma \tag{1.25}$$

Using the above equations we obtain:

$$E = \frac{2E_e\sin\gamma}{\sin\theta + \sin\gamma - \sin(\theta+\gamma)} \tag{1.26}$$

Substituting the scattered electron energy, $E$, from equation (1.26) in the equations (4.2), (4.3) and (4.4) that reconstruct $Q^2$, $y$, and $x$ according to the electron method, we extract the event kinematics in terms of the scattering angles $\theta$ and $\gamma$:

$$Q^2_{DA} = 4E_e^2\frac{\sin\gamma\,(1+\cos\theta)}{\sin\gamma + \sin\theta - sin(\theta+\gamma)} \tag{1.27}$$

$$y_{DA} = \frac{\sin\theta\,(1-\cos\gamma)}{\sin\gamma + \sin\theta - sin(\theta+\gamma)} \tag{1.28}$$

$$x_{DA} = \frac{E_e}{E_p}\frac{\sin\gamma + \sin\theta + sin(\theta+\gamma)}{\sin\gamma + \sin\theta - sin(\theta+\gamma)} \tag{1.29}$$

Although the determination of the angle $\gamma$ is based on hadronic energies, it is only weakly affected by hadronic energy miscalibrations, since it involves a ratio of energies.

## 4.2 Radiative events

QED radiative processes shift the reconstructed kinematic variables, in addition to modifying the Born cross section. As discussed in section (1.7), the largest radiative corrections originate from the emission of a real photon from the initial or final state electron. Therefore, the shift in the reconstructed $x$, $y$ and $Q^2$ is larger when the kinematic variables are calculated at the lepton vertex (i.e. using the electron method).

In the case of Initial State Radiation (ISR), a real photon of energy $E_\gamma$ is emitted from the initial state electron. Thus, the effective energy of the incident electron becomes $E_e - E_\gamma$, where $E_e$ is the electron beam energy. The photon is emitted collinear with the beam electron and is usually lost in the rear direction of the beampipe. A small number of these initial state photons (about 15%)[44] are detected by the photon calorimeter of the Luminosity monitor.

In the case of Final State Radiation (FSR), a real photon is emitted from the final state electron. If $E$ is the energy of the scattered electron as measured in the calorimeter, the real energy of the outgoing electron at the lepton vertex is $E + E_\gamma$. In most cases the final state photon is emitted at very small angles relative to the scattered electron. Thus, the calorimeter-measured energy of the latter effectively includes the energy of the emitted photon, and the effects



of FSR on the kinematic reconstruction are relatively small.

For radiative events, the equations (1.2), (1.3) and (1.1) give only the *apparent reconstructed* $Q^2_{elec}$, $y_{elec}$ and $x_{elec}$. Substituting the effective energies of the initial or final state electron in the above equations we obtain the *true reconstructed* kinematics, $Q^2_{rad}$, $y_{rad}$ and $x_{rad}$, for ISR or FRS events, respectively.

ISR :

$$Q^2_{rad} = 2(E_e - E_\gamma)E(1 + \cos\theta) \tag{4.30}$$

$$y_{rad} = 1 - \frac{E}{2(E_e - E_\gamma)}(1 - \cos\theta) \tag{4.31}$$

$$x_{rad} = \frac{Q^2_{rad}}{s_{rad}\, y_{rad}} = \frac{E\cos^2\frac{\theta}{2}}{E_p\left[1 - \frac{E}{E_e - E_\gamma}\sin^2\frac{\theta}{2}\right]}, \tag{4.32}$$

with $s_{rad} = 4E_p(E_e - E_\gamma)$.

FSR :

$$Q^2_{rad} = 2E_e(E + E_\gamma)(1 + \cos\theta) \tag{4.33}$$

$$y_{rad} = 1 - \frac{E + E_\gamma}{2E_e}(1 - \cos\theta) \tag{4.34}$$

$$x_{rad} = \frac{Q^2_{rad}}{s_{rad}\, y_{rad}} = \frac{(E + E_\gamma)\cos^2\frac{\theta}{2}}{E_p\left[1 - \frac{E+E_\gamma}{E_e}\sin^2\frac{\theta}{2}\right]}, \tag{4.35}$$

with $s_{rad} = 4E_pE_e$.

By comparing the above sets of equations with eqs.(4.2), (4.3) and (4.4), we conclude that $Q^2_{rad}$ is smaller or larger than $Q^2_{elec}$ for ISR or FRS, respectively. However, $y_{rad}$ is smaller than $y_{elec}$, and $x_{rad}$ is larger than $x_{elec}$, for both ISR and FSR events.

## 4.3 Smearing and Migration effects

Detector smearing effects on the measurement of the energies and angles of the final state electron and hadron flow introduce additional shifts in the reconstructed $x$, $y$ and $Q^2$ compared to the true values. In order to investigate the smearing of the kinematic variables due to QED radiative processes and detector effects, we use the Monte Carlo sample, after it has passed through the ZEUS detector simulation, and compare the reconstructed $x$, $y$ and $Q^2$ with the true values, which are calculated from the 4-momenta of the initial and final state particles. The results for the initial Monte Carlo sample, before any cuts are applied, are shown in fig. 4.3.

The resolution in $Q^2$ is better for the electron and double angle methods than for the Jacquet-Blondel method. For all methods, it deteriorates in the low-$Q^2$ region.

Since the variable $x$ is calculated from $Q^2$ and $y$ for all methods, the resolution in $x$ is determined mainly from the resolution in $y$.

For the electron method, the energy-loss of the scattered electron, mainly due to dead material in front of the calorimeter and secondarily due to photon radiation, yields a reconstructed $y_{elec}$ value greater than the true $y$. The effect becomes worse in the low-$y$ region, and results in poor resolution in $x$, especially at high-$x$.

For the Jacquet-Blondel reconstruction method, the $y$-resolution also degrades at low-$y$. In this region, the current jet is emitted at very low scattering angles and gets lost in the forward beam-pipe, while the reconstruction picks up calorimeter cell noise and treats it as hadronic energy deposits.



For the double angle method, in the low-$y$ region, the same effect (i.e. calorimeter noise interpreted as hadronic flow, when the current jet is lost in the beampipe) shifts the reconstructed angle $\gamma$ to higher values (towards the rear direction), and yields reconstructed $y$ values greater than the true ones.

The resolution plots from the final Monte Carlo sample, after all selection criteria have been applied, are shown in chapter 7.

Due to the smearing of the kinematic variables, the number of reconstructed events in a given bin in the $(x, Q^2)$ phase space differs from the number of generated events in that bin. A fraction of the events generated in the bin have migrated to adjacent bins, while a fraction of the reconstructed events have migrated into the bin from adjacent bins.

The migrations for the three reconstruction methods, as extracted from the whole Monte Carlo sample, before any selection criteria are applied, are shown in fig. 4.4. In this figure, the phase space has been divided into the $x$ and $Q^2$ bins that will be used in the $F_2$ extraction, as discussed in chapter 8. The three dotted lines represent the $y = 1, 0.1$, and 0.01 boundaries. The large migrations at high-$x$ for the electron method are consistent with the poor resolution in $x$, at high $x$ values, of this reconstruction method. For the Jacquet-Blondel and double angle methods, the migration plots show the shift in the $y$ reconstruction towards higher $y$ values, in the low-$y$ region.

As it is evident from the resolution and migration plots, the Jacquet-Blondel method is the least favourable in terms of a reliable reconstruction of the event kinematics. The electron and double angle methods are in principal complementary in resolution in the low and intermediate $x$ regions, and are both used in this thesis.

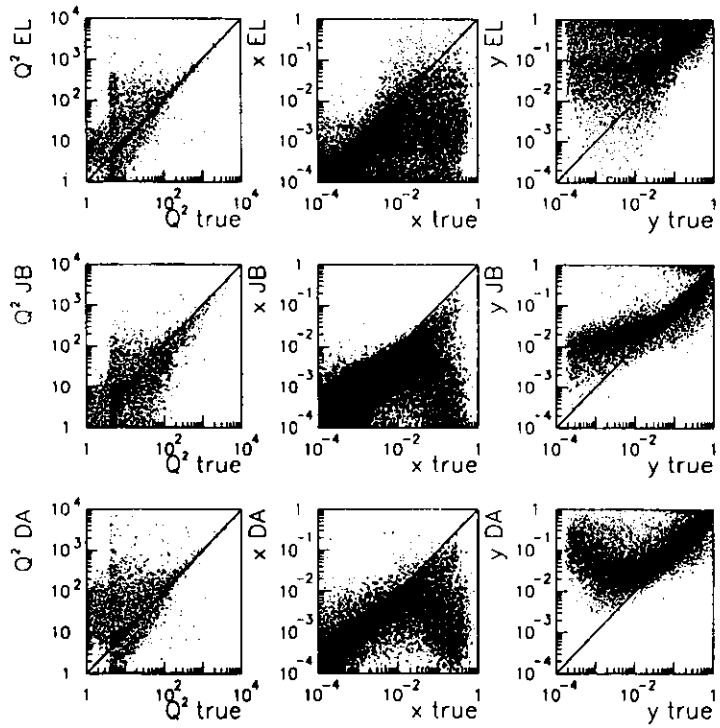


Figure 4.3: *Resolution in $Q^2$, $x$, $y$, for the Electron, Jacquet-Blondel and Double Angle reconstruction methods. The true variables are plotted on the x-axis. The reconstructed variables are plotted on the y-axis. No selection criteria are applied.*



The migrations for the electron and double angle methods, extracted from the final Monte Carlo sample (after the event selection), and for the $(x, Q^2)$ bins where an $F_2$ value is reported, are shown in chapter 8.

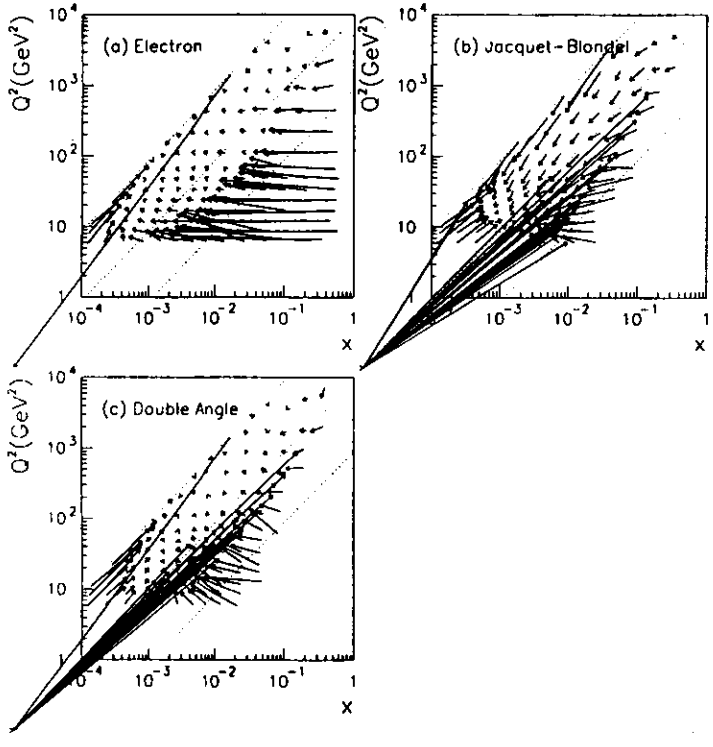


Figure 4.4: *Migrations from the generated to the reconstructed kinematic variables, in the $(x, Q^2)$ phase space, for the three reconstruction methods. No selection criteria are applied.*



# Chapter 5

# Event Selection

The selection procedure for DIS NC data is discussed in this chapter. The methods used to reconstruct the event vertex, identify the scattered electron, reconstruct the impact point of the scattered electron and determine the angle of the hadron system are described. The cuts necessary to select well-reconstructed events are discussed. The sources of background to the DIS data are described, and the selection criteria imposed to reduce the various backgrounds are explained.

## 5.1 Vertex Reconstruction

The position of the event vertex influences the reconstruction of the scattering angles of the electron and hadron system, and hence the reconstruction of the event kinematics. The acceptance of the final DIS event sample also depends on the event vertex, through the selection criteria applied to the variable $y$ and to the quantity $(E_{tot} - P_{z\,tot})$, as is discussed in the following sections.

For most of the DIS NC events the vertex position is reconstructed using VXD and CTD information. The algorithm recognizes trajectories in the CTD, extends them into the VXD, and fits them to estimate the event vertex

position. The track Z-vertex distributions for both data and Monte Carlo samples, without analysis cuts, are shown in fig. 5.1a. The two distributions are in good agreement. A gaussian fit to the peak of the data yields a root-mean-square of ±11.1 cm. The actual Z-width of the collision region, as determined by the root-mean-square of the proton bunch length, is about ±20 cm (see section 2.1).

For 16% of the events, both the outgoing electron and the hadron system are emitted at very small angles, and leave no tracks in the CTD. For these events the position of the vertex is reconstructed using calorimeter timing. The timing Z-vertex distribution for the data sample, without analysis cuts, is shown in fig. 5.1b. A gaussian fit to the peak yields a root-mean-square of ±18.9 cm.

The difference between the generated and the track-reconstructed Z-vertex distribution for Monte Carlo events is shown in fig. 5.1c. A fit to this distribution yields a mean resolution for the vertex position reconstruction equal to 3.3 mm.

The efficiencies for vertex reconstruction using tracking and calorimeter

| | Data - no cuts | DIS MC - no cuts |
|---|---|---|
| Tracking vertex | 83.5% | 80.65% |
| CAL Time vertex | 9.5% | |
| no vertex | 7.0% | 19.35% |

Table 5.1: *Efficiencies for reconstructing the event vertex for the whole data and DIS Monte Carlo samples, before any selection criteria.*



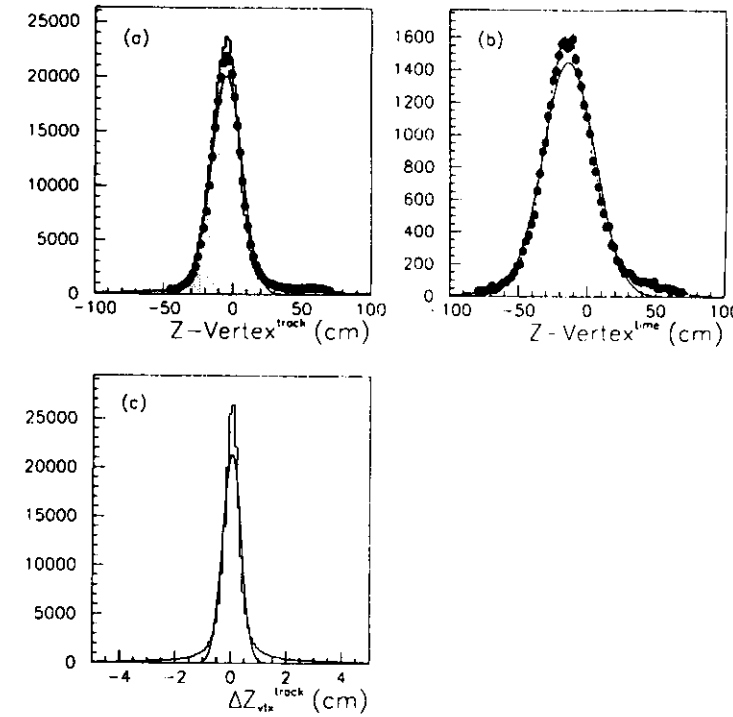


Figure 5.1: *The reconstructed Z-vertex distributions from data and Monte Carlo samples, without cuts. (a) The Z-vertex distribution from tracking information. The shaded area gives the Monte Carlo distribution, the points represent the data distribution, and the line is a gaussian fit to the data. (b) The data Z-vertex distribution from timing information. The line gives the gaussian fit. (c) The difference between reconstructed and generated tracking Z-vertex for Monte Carlo.*

timing information, for data and Monte Carlo before selection cuts, are shown in table 5.1. For data, the timing vertex is used if there is no tracking vertex available. For data events where a vertex cannot be reconstructed by either method, the event vertex is set to zero (nominal beam interaction point). For Monte Carlo events, the vertex is also set to zero if no tracking vertex is available. The vertex reconstruction efficiencies for the final samples are given in chapter 7.

## 5.2 Electron Identification

The identification of a scattered electron in the ZEUS calorimeter is based on the difference in size (both in longitudinal and transverse dimensions) between electromagnetic and hadronic shower clusters, and on the degree of isolation of clusters. An electron produces a shallow and narrow shower, with most of its energy deposited in the EMC section of the calorimeter, and generally well isolated from other energy deposits.

The calorimeter cells are first projected onto a spherical surface, centered at the event vertex. EMC cells with energy greater than 1 GeV are defined as seed cells, around which two concentric cones of different size are constructed. For EMC cells, the half angles of the inner and outer cones are $\theta^{\rm EMC}_{\rm inner} = 250$ mrad and $\theta^{\rm EMC}_{\rm outer} = 400$ mrad, respectively, while for HAC1 and HAC2 cells the equivalent angles are $\theta^{\rm HAC}_{\rm inner} = 300$ mrad and $\theta^{\rm HAC}_{\rm outer} = 500$ mrad. If two or more seed cells are found within the cone of half angle 250 mrad, the highest energy cell is considered to be the seed cell. All cells within the two cones are considered as a single cluster and the clusters constructed in this way are the



electron candidates.

For each electron candidate, a quality factor is calculated, which is a combination of the size of the cluster, the ratio of EMC to HAC energies, and the degree of the cluster isolation. The calculation of this quality factor is based on the following quantities:

- energy imbalance between the energy calculated from the left and right readout of the seed cell energy,
- energy weighted radius of EMC-inner-cone,
- ratio of EMC-outer-cone energy to EMC-inner-cone energy,
- ratio of HAC1-inner-cone energy to EMC-inner-cone energy,
- energy in HAC1-outer-cone,
- energy in HAC2-outer-cone,
- ratio of HAC2-outer-cone energy to EMC-inner-cone energy.

Only electron candidates that pass the cut on the quality factor are kept. This cut has been determined from calorimeter testbeam data and studies with Monte Carlo samples.

In addition, the electron candidates are required to pass the following cuts:

- energy of the electron candidate (EC) higher than 2 GeV;
- number of calorimeter cells belonging to EC cluster less than 35;
- energy imbalance of the EC seed cell less than 0.2;

- ratio of the HAC energy to the total energy of the EC less than 0.1,

where the total energy of an electron candidate is defined as the sum of the energies of the EMC-inner, EMC-outer, HAC1-inner and HAC2-inner cones.

If more than one electron candidate remains after the above procedure, the one with the highest energy is considered as the scattered electron of the event.

In addition to the main electron finding algorithm described above (EF1), a second one (EF2), based on neural network logic,[45] has been used for systematic studies.

The efficiency and purity of an electron finder are defined as follows:

$$\text{Efficiency} = \frac{\text{number of correctly identified electrons}}{\text{number of true electrons}} \tag{5.1}$$

$$\text{Purity} = \frac{\text{number of correctly identified electrons}}{\text{number of identified electrons}} \tag{5.2}$$

where a correctly identified electron is an electromagnetic cluster that has both been generated and identified by the electron finder as the scattered electron of the event. The efficiencies and purities of both electron finders have been studied using the DIS NC Monte Carlo sample,[45] after the $\delta$ cut (section 5.7) and the *box* cut (section 5.3) have been applied. The efficiency of EF1 is between 40% and 60% at low scattered electron energies (5 GeV to 12 GeV), between 80% and 90% for energies 12 GeV to 20 GeV, and 98% or higher for scattered electron energies above 12 GeV. The purity of EF1 is around 95% at low energies, and better than 97% for energies above 12 GeV. The efficiency of



EF2 at 5 GeV is 70%, with a purity of about 96%. For energies greater than 12 GeV, the efficiency of EF2 is about 90% or higher, and the purity is 98% or better.

For low values of the scattered electron energy, the current jet follows the same direction as the scattered electron. The hadronic energy around the outgoing electron makes the electron identification both difficult and unreliable, and results in poor efficiencies and purities of the electron finders. In order to avoid this effect, events with scattered electron energy less than 5 GeV are removed from the sample. This cut is referred to as the *electron energy cut*.

## 5.3 Electron Position Reconstruction

The impact point of the scattered electron is reconstructed using calorimeter information.

The center of the electromagnetic shower is obtained from the $3 \times 3$ array of calorimeter cells centered around the cell with the maximum energy deposit. Due to the rectangular shape of the calorimeter cells, the position reconstruction is different in the $X$ and $Y$ directions. The vertical position $Y$ is determined from the energy leakage of the electron to the adjacent 3-cell rows (strips) above ($E_{strip_{up}}$) and below ($E_{strip_{down}}$) the row that contains the maximum energy cell ($E_{strip_{center}}$):

$$Y = Y_o \frac{E_{strip_{up}} - E_{strip_{down}}}{E_{strip_{up}} + E_{strip_{center}} + E_{strip_{down}}}. \tag{5.3}$$

The horizontal position $X$ is reconstructed as the energy weighted mean of the shower centers of the three 3-cell columns (modules). The shower center of each module is determined from the energy imbalance between the signals

from the left and right PMTs of each cell:

$$X = X_o \frac{E_{left} - E_{right}}{E_{left} + E_{right}} \tag{5.4}$$

The cells in the upper and lower strips contribute to the imbalance of the relevant module only if they contain more than 2.5% of the energy.

The functions $Y_o$ and $X_o$ for the RCAL are obtained by fitting parametrized functions to the RHES (see section 2.2.3) electron position of the real DIS NC data. For FCAL and BCAL, the functions are fit to testbeam data.

The difference between the reconstructed and generated polar and azimuthal angles of the scattered electron are shown in fig. 5.2. The resolution in $\theta$ is approximately 0.8°, while the resolution in $\phi$ is approximately 2.5°.

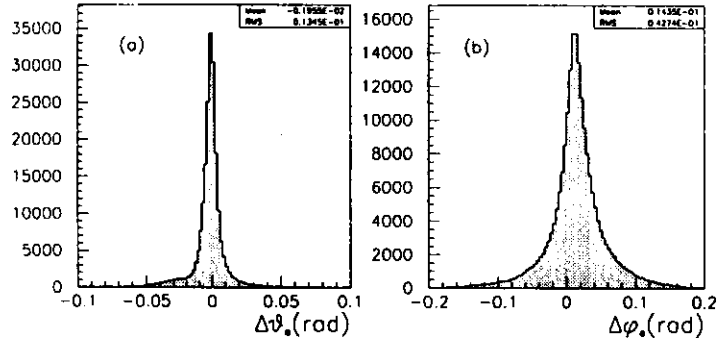


Figure 5.2: *The reconstruction resolutions for the angles of the scattered electron, for the DIS NC Monte Carlo, without any selection criteria applied. (a) The difference between reconstructed and generated polar angle. (b) The difference between reconstructed and generated azimuthal angle.*



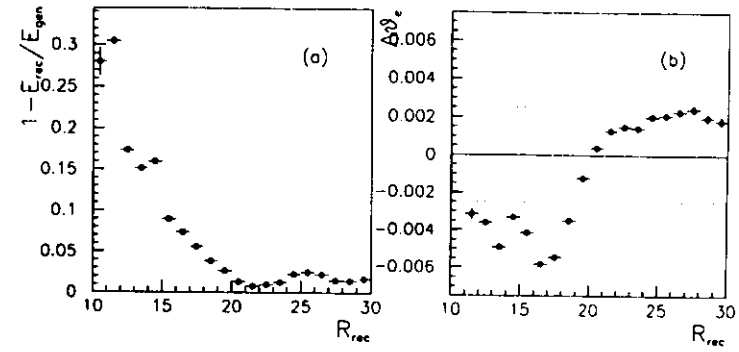


Figure 5.3: *The RCAL beampipe effect on the reconstruction of the scattered electron. In (a) the fractional energy leakage and in (b) the resolution of the scattered electron polar angle are plotted as a function of the reconstructed distance around the RCAL beampipe. No selection criteria are applied.*

In the region around the RCAL beampipe the reconstruction of the electron impact position is poor, due to energy leakage into the beampipe hole. The quantity $1 - E_{rec}/E_{gen}$, where $E_{rec}$ and $E_{gen}$ are the calorimeter measured and generated energies of the scattered electron, respectively, is plotted in fig. 5.3a, as a function of $R_{rec} = \sqrt{X^2 + Y^2}$ around the RCAL beampipe, for the whole Monte Carlo sample, before any selection criteria are applied. If the maximum energy cell is vertically adjacent to the beampipe, the upper or lower strip is lost and the $Y$ position reconstruction is significantly affected. The $X$ position reconstruction is affected for maximum energy cells horizontally adjacent to the beampipe. This effect, however, is less pronounced than in the $Y$ direction, since the module (or cell) with the maximum energy deposit contributes the

most to the $X$ reconstruction. The effect of the RCAL beampipe on the resolution of the scattered electron polar angle $\theta$ is shown in fig. 5.3b. In order to avoid the electron energy leakage in the beampipe hole and ensure a reliable reconstruction of the electron scattering angle, the electron impact position on the face of the RCAL is required to lie outside a square of half side 16 cm around the center of the RCAL beampipe. This cut is referred to as the *box cut*.

## 5.4 Hadron Angle

When the current jet is emitted at very low scattering angles (i.e. in the low-$y$ region) and gets lost in the forward (proton) direction of the beampipe, the calorimeter cell noise, misidentified as hadronic flow, shifts the reconstructed angle $\gamma$ of the hadron system to higher values, as discussed in section 4.3. This effect yields a poor resolution in $\gamma$, and therefore, a poor resolution in $y$, in the low-$y$ region. This can be seen in fig. 5.4a, where the difference between the generated and reconstructed angles is plotted for the whole NC DIS Monte Carlo sample, before any selection criteria are applied.

This effect can be reduced by applying a cut on $y_{JB}$ (see section 4.1.2), when using the Double Angle reconstruction method (see section 4.1.3), in order to ensure sufficient hadronic activity in the calorimeter and a good reconstruction of the angle $\gamma$. The cut applied is $y_{JB} > 0.01$ and is referred to as the *$y_{JB}$ cut*.

The relative resolution of $y_{DA}$ as a function of $y_{JB}$ for the whole MC sample is shown in fig. 5.4b. For $y_{JB}$ greater than 0.01 the resolution in $y_{DA}$ considerably improves over that at low-$y$ values.



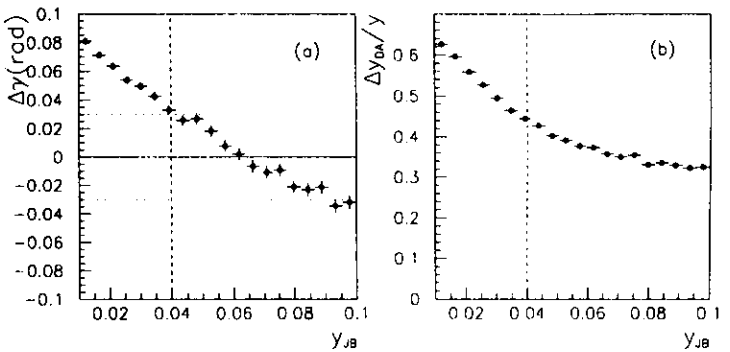


Figure 5.4: *The hadron angle $\gamma$. (a) The resolution of the $\gamma$-reconstruction, as extracted from the NC DIS Monte Carlo, plotted as a function of $y_{JB}$. (b) The relative resolution of $y_{DA}$, as extracted from the Monte Carlo, plotted as a function of $y_{JB}$. No selection criteria are applied.*

## 5.5 Background Sources

### 5.5.1 Cosmic Ray / Beam Halo Muons

A cosmic ray muon background event is characterised by a large EMC energy deposit, which mimics a scattered electron, very little activity in the rest of the calorimeter, and a maximum of two tracks in the CTD. The difference in time (see section 5.6) between the top and the bottom of the calorimeter, for a cosmic muon event, should correspond to the transit time of muons.

In addition to the cosmic muon background, there are also beam-associated

halo muons. The main characteristic of this type of muon background event is the difference from cell to cell in x and y positions, which should be quite small.

Muon background events are recognized by an algorithm that first examines the following quantities:

- the total energy in the calorimeter,
- the total number of calorimeter cells above threshold,
- the number of calorimeter cells hit,
- the maximum energy deposited in a cell,
- the calorimeter energy deposited around the beam pipe,
- the number of tracks in the CTD.

If an event is classified by these criteria as a possible muon event, the algorithm imposes a second set of criteria. The most important of them are the time difference between the upper and lower part of the calorimeter, for cosmic muon events, and the difference in x and y positions between the hit cells, for beam halo muon events.

### 5.5.2 QED Comptons

Elastic QED Compton background events,

$$ep \rightarrow ep\gamma, \tag{5.5}$$

are characterized by two electromagnetic clusters in the calorimeter, one track in the CTD, and no energy in the FCAL. They are not simulated in the



Monte Carlo. Therefore, they have to be removed from the data sample. The algorithm that identifies elastic QED Compton events searches for:

- two electromagnetic clusters in the calorimeter,
- total energy sum of the two clusters 15 GeV $\leq E_{sum} \leq$ 30 GeV,
- remaining energy in the calorimeter $E_{rest} \leq$ 1 Gev,
- maximum of one track in the CTD.

Inelastic QED Compton events are simulated in the Monte Carlo.

### 5.5.3 Beam Induced Background

A large source of background arises from interactions of the proton or electron beam with residual beam-pipe gas, the protons having a larger cross section than the electrons. The signature of the beam-gas events depends on the interaction point.

Proton-gas events that originate downstream the detector (in the positive-z direction towards the FCAL) do not enter the calorimeter and do not leave a signal. Proton-gas events that originate inside the detector deposit large amounts of energy in the FCAL and no energy in the RCAL, and they can be removed by an energy-momentum-conservation cut, as will be discussed in section 5.7. Proton-gas events that originate upstream the detector (in the negative z-direction, towards the RCAL) can be removed by timing cuts, as will be discussed in section 5.6. Nevertheless, a small fraction of proton-gas events escape the momentum-conservation and timing cuts, contaminating the

final data sample. The rate of this remaining proton-gas background can be estimated from the proton pilot bunches, as discussed in section 5.10.1.

Electron-gas events that originate downstream or upstream in the detector either do not deposit any energy in the calorimeter, or can be removed by timing cuts. However, electron-gas events that originate inside the detector produce an event signature very similar to the nominal DIS events. These background events contaminate the final data sample. Their rate is small and is estimated from the electron pilot bunches, as discussed in section 5.10.1.

### 5.5.4 Photoproduction

A large source of background to the DIS NC events, especially at high $y$ values, comes from photoproduction (PHP):

$$ep \rightarrow e + X, \quad \text{at } Q^2 \approx 0. \tag{5.6}$$

The total photoproduction cross section as measured by ZEUS [46] is:

$$\sigma_{tot}(\gamma p) = 154 \pm 16(stat.) \pm 32(syst.)\ \mu\text{b}, \tag{5.7}$$

at an average center of mass energy of 210 GeV.

The outgoing electron for PHP events is emitted at very low angles and in most cases escapes undetected in the rear direction down the beampipe. Therefore, the PHP background is significantly reduced by requiring a detected electron in the final state. However, some PHP events still remain in the sample, because occasionally the electron-finding algorithm wrongly identifies an electron in the hadronic activity of the calorimeter. If the falsely identified electron lies around the FCAL beampipe, the event has a very high



reconstructed $y_{elec}$, and can be removed by applying a $y_{elec}$ cut (section 5.8). A part of the remaining PHP events are removed by momentum-conservation considerations, as discussed in section 5.7. Nevertheless, a fraction of the photoproduction background contaminates the final sample. This has to be estimated and subtracted statistically using the PHP Monte Carlo, as discussed in section 5.10.2.

## 5.6 Calorimeter Timing

The time that a particle hits a calorimeter cell is extracted from the PMT information. An energy weighted average of the times of all cells, with energy deposits greater than 200 MeV, in a particular calorimeter section (F/B/RCAL), yields the total time of this section ($t_F$, $t_B$, $t_R$).

The time offset of each individual PMT is adjusted so that the calorimeter cell time equals zero for interactions originating at the nominal interaction point and at the nominal bunch crossing time. Therefore, for nominal $ep$ interactions, the difference $t_F - t_R$ should equal zero. However, for a proton-gas interaction that occurs upstream of the detector, the outgoing particles reach the RCAL earlier than the FCAL, and the time difference $t_F - t_R$ is approximately equal to the time needed to travel twice the distance from RCAL to the nominal interaction point ($\sim$ 11ns). Thus, a cut applied on the $t_F - t_R$ distribution significantly reduces the proton-gas background. In fig. 5.5 the difference $t_F - t_R$ is plotted versus $t_R$, for DIS events accepted at the DST (see section 5.9.2) level, after a timing cut of $|t_F - t_R| < 8$ ns has been applied. The main peak represents the DIS events, whereas a small number

of remaining proton-gas background events can be seen on the upper left side of the plot. In order to remove this remaining background, a stricter cut of

$$|t_F - t_R| < 6\text{ns} \tag{5.8}$$

is applied at the final selection level.

In practice, the proton bunch length broadens the time distribution of the FCAL, and hence, also the $t_F - t_R$ distribution, for both $ep$ and proton-gas interactions. The time distribution of the RCAL for nominal $ep$ interactions is affected only by the electron bunch length. However, for proton-gas interactions, the $t_R$ distribution is also affected by the proton bunch length. Therefore, it is broader than the $t_R$ distribution for $ep$ interactions. This effect can be used to remove the proton-gas background for events with a small energy deposit in the FCAL, which does not allow a $t_F$ measurement, by requiring:

$$|t_R| < 6\text{ns}. \tag{5.9}$$



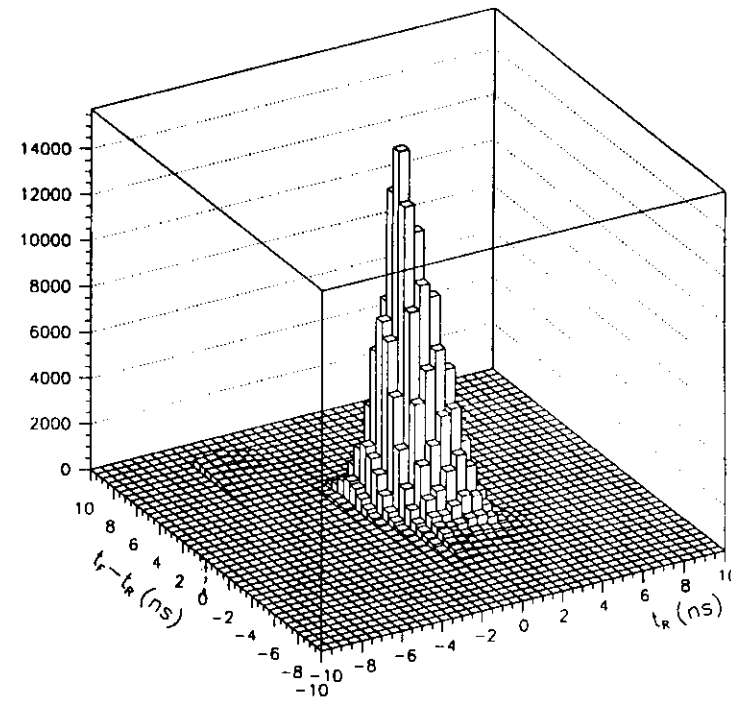


Figure 5.5: *Measured time difference between FCAL and RCAL, versus the RCAL time, for events accepted at the DST level. The main peak comes from the DIS events. The small excess on the upper left side is due to proton-gas events.*

## 5.7 Momentum Conservation

Although ZEUS is a nearly hermetic detector, a large part of the proton remnant jet, which is emitted at very low angles, escapes undetected in the forward direction down the beampipe. In order to minimize analysis mistakes due to this effect, the difference between the total energy of the event and the energy in the z-direction is used. We define $\delta$ as:

$$\delta \equiv E_{tot} - P_{z\,tot} = \sum_i E_i(1 - \cos\theta_i), \tag{5.10}$$

where the sum runs over all calorimeter cells.

Conservation of $E_{tot}$ and $P_{z\,tot}$ during the interaction determines that $\delta$ must be equal to twice the energy of the initial electron, $2E_e$, for a completely hermetic detector:

$$(E_{tot} - P_{z\,tot})_{final} = (E_{tot} - P_{z\,tot})_{initial} = (E_p + E_e) - (E_p - E_e) = 2E_e. \tag{5.11}$$

Although this is not exactly the case at ZEUS, the proton remnant jet contributes very little to $\delta$, since it is emitted at very small, forward angles. Therefore, for DIS events it is expected that:

$$\delta^{DIS} = 2E_e. \tag{5.12}$$

In the case of ISR events, the initial electron energy $E_e$ is lowered to $E_e - E_\gamma$, where $E_\gamma$ is the energy of the real photon which is emitted from the initial state electron, as discussed in section 4.2. In most of the cases, the photon escapes undetected in the direction of the beampipe, and the apparent (measured) $\delta$ peaks at lower values:

$$\delta^{ISR}_{app} = 2(E_e - E_\gamma). \tag{5.13}$$



In the case of photoproduction events, the scattered electron (of energy $E$) escapes undetected in the rear direction of the beampipe, yielding again a lower $\delta$ value:

$$\delta^{PHP}_{app} = 2E_e - E. \tag{5.14}$$

The $\delta$ distribution for photoproduction Monte Carlo events (see section 5.10.2) is plotted in fig. 5.6. Also plotted in this figure is the $\delta$ distribution for the standard DIS NC Monte Carlo events.

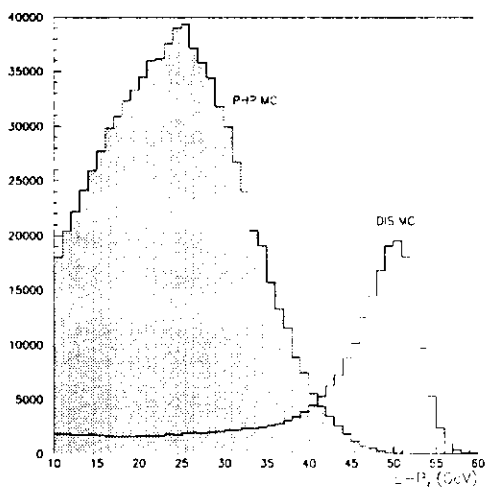


Figure 5.6: *The $E_{tot} - P_{z\,tot}$ distribution for events accepted at the DST level. The unshaded histogram represents the DIS NC Monte Carlo events. The shaded histogram represents the PHP Monte Carlo events, normalized to the DIS Monte Carlo luminosity.*

Finally, low $\delta$ values are found for proton beam-gas events which occur inside the detector, since they deposit a considerable amount of energy in the FCAL, but no energy in the RCAL.

In order to remove all three types of background, a lower cut on $(E_{tot} - P_{z\,tot})$ is applied at various phases of the DIS selection procedure. Looser cuts, of 20 and 25 GeV, that include the energy measured by the photon calorimeter of the Luminosity monitor, are applied at the early phases. At the final selection phase, the lower cut is raised to 35 GeV, while the upper cut is determined by eq. (5.12) ($2 \cdot 26.7$ GeV $+1\sigma$):

$$35\,\mathrm{GeV} < \delta < 60\,\mathrm{GeV}. \tag{5.15}$$

## 5.8 Fake FCAL Electrons

In some cases, the electron finder incorrectly identifies an electron within the hadronic activity around the FCAL beampipe. For the present HERA kinematic range, there is a high probability that these FCAL electrons are fake. Most of them belong to photoproduction events, which have to be removed from the data sample.

Since the reconstructed $y_{elec}$ of the events with the FCAL electron is fairly high, these events can be removed by applying a $y_{elec}$ *cut*:

$$y_{elec} < 0.95. \tag{5.16}$$



## 5.9 Data Selection

The selection criteria, most of which have been discussed in the previous sections, are summarized here.

### 5.9.1 Trigger

The DIS NC Trigger is applied at three levels.

The First Level Trigger (FLT) requires a logical OR of three conditions:

- BCAL EMC energy greater then 3.1 GeV
- RCAL EMC energy, excluding the trigger towers around the RCAL beampipe, greater than 2 GeV
- RCAL EMC energy, including the trigger towers around the RCAL beampipe, greater than 3.75 GeV

The Second Level Trigger (SLT)

- applies timing cuts of 8ns on the FCAL and RCAL time, $|t_F|$ and $|t_R|$, respectively, in order to further reduce the proton beam-gas background,
- rejects sparks in the calorimeter.

The Third Level Trigger (TLT - DIS NC filter)

- applies timing cuts, of 8ns, on $|t_R|$, $|t_F|$, $|t_F - t_R|$, and the global calorimeter timing $|t_G|$,
- rejects cosmic and beam halo muons, using the online version of the muon finder,

- requires:

$$(E_{tot} - P_{z\,tot}) + 2E_{\gamma} > 20 \text{ GeV}. \quad (5.17)$$

In the 1993 data taking a total of $2 \times 10^6$ events was recorded with the DIS NC trigger.

### 5.9.2 DST

Events are written on the DIS NC Data Summary Tape (DST) if the following requirements are satisfied:

- the event passes the TLT DIS NC filter
- stricter calorimeter timing cuts are passed: a cut of 6 ns is applied on the RCAL time $|t_R|$, and a cut of 8 ns is applied on the FCAL time $|t_F|$, global calorimeter timing $|t_G|$, and on the quantity $|t_F - t_R|$
- cosmic and beam halo muons are not found, using the offline versions of the muon finder
- after removal of sparks, events must have an energy deposit in the calorimeter
- an electron is loosely identified, taking the logical OR of four electron finders, with electron energy greater than 4 GeV
- a stricter cut on the quantity $(E_{tot} - P_{z\,tot}) + 2E_{\gamma}$ is passed:

$$(E_{tot} - P_{z\,tot}) + 2E_{\gamma} > 25 \text{ GeV}. \quad (5.18)$$

After the DST filter, $3.1 \times 10^5$ events remained in the DIS NC data sample.



### 5.9.3 Preselection

The DIS NC events written on DST are further processed, in order to remove:

- events with an incomplete or malfunctioning detector,
- events with total energy in the calorimeter less than 2 GeV.

After the preselection phase, the remaining data sample consists of 380,537 events, corresponding to an integrated luminosity of 545.63 $\text{nb}^{-1}$.

The DIS NC Monte Carlo is also processed through the preselection, removing events with total calorimeter energy less than 2 GeV.

### 5.9.4 Final Selection

The final selection criteria applied to the data are the following:

- *Electron Energy cut*: $E \geq 5$ GeV
  to ensure reliable electron finding and reduce photoproduction background;
- *$\delta$ cut*: 35 GeV $\leq (E_{tot} - P_{z\,tot}) \leq 60$ GeV
  to reduce ISR, photoproduction and proton-gas backgrounds;
- *Box cut*: $|X_{elec}| \geq 16$ cm and $|Y_{elec}| \geq 16$ cm, in the RCAL
  to ensure full containment of the electron shower;
- *$y_{elec}$ cut*: $y_{elec} \leq 0.95$
  to reduce photoproduction background
- *$y_{JB}$ cut*: $y_{JB} \geq 0.04$, only for the Double Angle method
  to ensure good measurement of the hadron angle $\gamma$;

- *timing cuts*: $|t_R| \leq 6$ ns and $|t_F - t_R| \leq 6$ ns
  to reduce beam-gas background;
- removal of events that have originated from the electron or proton pilot bunches (see section 5.10.1);
- removal of remaining cosmic or halo muons;
- removal of QED Compton events.

All the above selection criteria, except for the timing cuts and the removal of the pilot-bunch events, are also applied to the DIS NC Monte Carlo sample.

After the final selection, the data sample for the Double Angle method consists of 41,513 events, while the sample for the Electron method consists of 65,316 events. It should be noted, however, that the number of events for the Electron method is modified by the electron energy corrections, discussed in the next chapter. The final statistics is given in chapter 7.



## 5.10 Background in the Final Sample

The remaining background in the data sample, after all selection cuts have been applied, cannot be identified on an event by event basis. It has to be estimated and subtracted statistically, in each $(x, Q^2)$ bin used for the $F_2$ extraction. This remaining background originates either from non-colliding beam interactions, or from photoproduction.

### 5.10.1 Non-Colliding Beam Background

Proton-gas or electron-gas events originate either from the proton/electron pilot bunches (see section 2.1), or from the colliding proton/electron bunches, when they interact with the residual gas in the beampipe.

Events identified by the bunch-crossing type as originating from the pilot bunches are used to calculate the number of colliding beam-gas events that survive all selection criteria and contaminate the final sample.

The number of $p(e)$-pilot bunch events that pass all cuts, in each $(x, Q^2)$ bin, is multiplied by the ratio of the total current of colliding $p(e)$ bunches to the total current of $p(e)$-pilot bunch(es). The ratio of currents is 12.976 for the proton beam and 7.848 for the electron beam. The result is an estimate of the total number of $p(e)$-gas events that remain in the bin after the final selection, and is subtracted from the number of events in the bin.

The estimated total number of proton- and electron-gas events in the final sample, in all $(x, Q^2)$ bins, accounts for approximately 1% of the final data sample. The details are given in chapter 7.

### 5.10.2 Photoproduction Background

The largest background in the final DIS data sample is that from photoproduction.

The photoproduction background that remains in each $(x, Q^2)$ bin after the electron energy cut, the $y_{elec}$ cut, and the $\delta$ cut, is estimated from Monte Carlo.

The PHP Monte Carlo events are generated with the PYTHIA minimum bias photoproduction generator, with generated $y > 0.6$. They are processed through the detector and trigger simulation programs, the event reconstruction program, and the full event selection procedure.

The photoproduction Monte Carlo event distribution is plotted versus $(E_{tot} - P_{z\,tot})$ in fig. 5.7, along with the nominal DIS NC Monte Carlo, before and after the electron energy cut and the $y_{elec}$ cut. It can be seen that a number of photoproduction events with $(E_{tot} - P_{z\,tot})$ greater than 35 GeV remains after the two cuts.

In order to statistically subtract the PHP background that contaminates the final data sample, the number of photoproduction Monte Carlo events that remain in a bin, after all selection criteria have been applied, is weighted to the total luminosity of the data and subtracted from the number of data events in the bin.

A total of 150k PHP events were generated, which corresponds to approximately 1/3 of the total data luminosity. The estimated photoproduction events in the final data sample are not distributed uniformly over the $(x, Q^2)$ plane. In the high $y$ bins, the PHP background is as high as 5%, but for most bins it amounts to only 1-2% or less. The final numbers of PHP background events,



for both the Electron and Double Angle methods, are given in chapter 7.

A second method of PHP background subtraction has also been used, for the Double Angle method. In each bin, a combination of exponential and gaussian curves is fit to the shape of the measured $\delta$ distribution, before the cut on $\delta$ is applied. The PHP background level estimated from the fit is about 50% higher than the one estimated from the PHP Monte Carlo. However, this difference is within the range covered by the various systematic checks on the PHP background, as discussed in section 8.6.

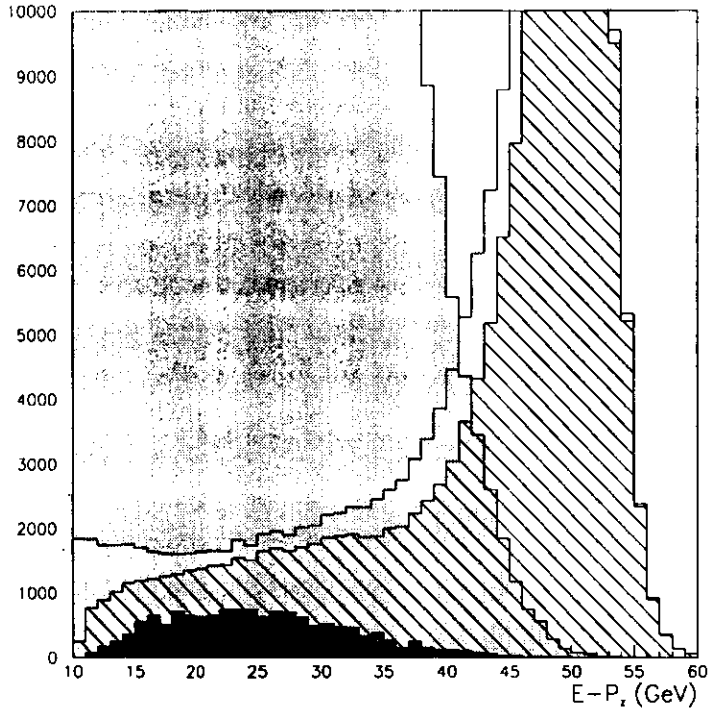


Figure 5.7: *The photoproduction background. The solid line on the right and the shaded area on the left represent the DIS NC Monte Carlo and the PHP Monte Carlo event distributions, at the DST level, respectively. The hashed area on the right and the solid area on the left represent the DIS NC Monte Carlo and the PHP Monte Carlo event distributions, after the electron energy and $y_{elec}$ cuts, respectively.*



# Chapter 6

# The Electron Energy Scale

## 6.1 Electron Energy Response

A reliable measurement of the energy of the final state electron is crucial for the reconstruction of kinematics when using the Electron method (see section 1.1.1). The effect on the Double Angle method (see section 1.1.3) is much less important, since it is relevant only for the selection cuts.

The electron energy response for the Electron method sample is shown in fig. 6.1. There is a discrepancy of approximately 1% between the scattered electron energy in the data and the Monte Carlo. The disagreement is mainly attributed to inactive material in front of the RCAL, especially around the RCAL beampipe, which is not fully simulated in the Monte Carlo.

The different electron energy response causes a discrepancy between data and Monte Carlo in the $\delta$ distribution, as can be seen in fig. 6.2. It also causes a disagreement in the reconstructed $x_{elec}$, $y_{elec}$ and $Q^2_{elec}$ between data and Monte Carlo, as can be seen in fig. 6.3.

A method to correct for the energy loss of the scattered electron due to inactive material, and hence make the use of the Electron method feasible, is discussed in this chapter.

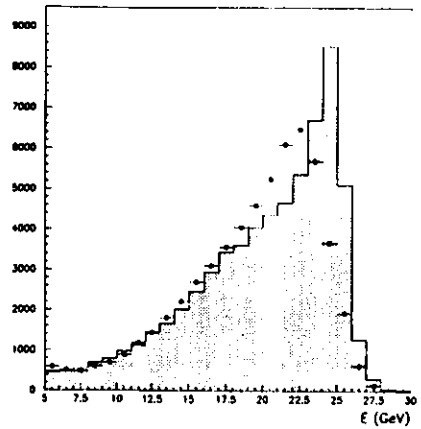


Figure 6.1: *Electron energy distribution, for data (points) and Monte Carlo (shaded histogram) events, for the Electron method sample.*

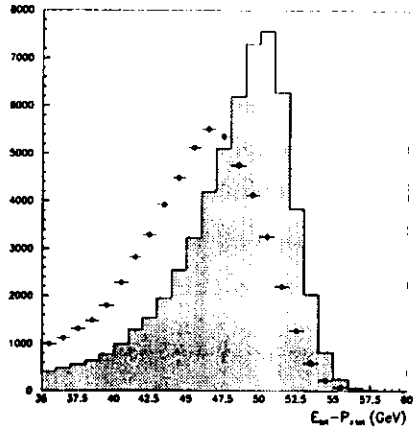


Figure 6.2: *δ distribution, for data (points) and Monte Carlo (shaded histogram) events, for the Electron method sample.*



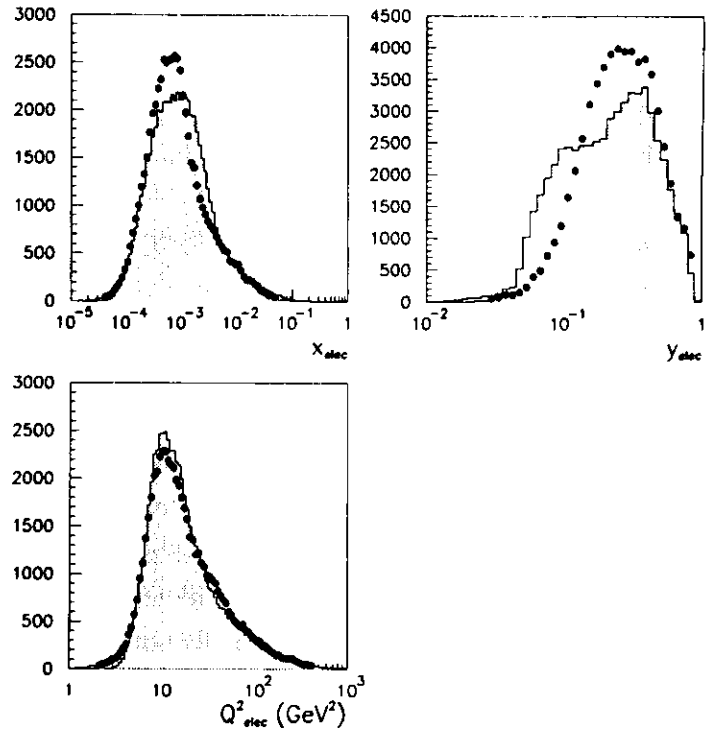


Figure 6.3: *x,y and $Q^2$ distributions, for data (points) and Monte Carlo (shaded histograms) events, for the Electron method sample.*

## 6.2 Kinematic Peak

In order to determine the spatial structure of the electron energy loss in the calorimeter, a sample of events with known scattered electron energies is needed. The *kinematic peak* (KP) region provides such a sample. The KP is a region of phase space where the mean scattered electron energy is almost equal to the incident electron energy. This occurs at low values of y, independently of $x$ and $Q^2$, as can be seen from eq. (1.3). The KP region is plotted in fig. 6.4 as the region bounded by the electron energy isolines of 26 and 27.5 GeV, around the beam electron energy isoline of 26.7 GeV.

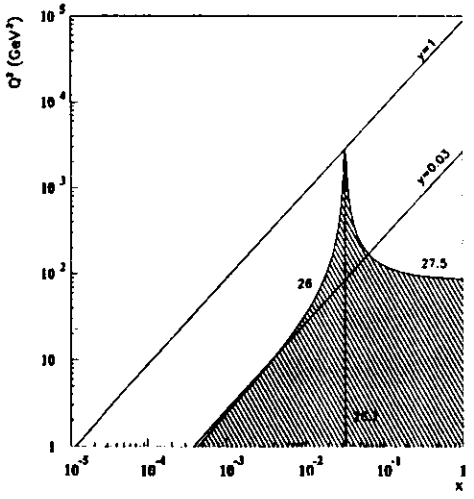


Figure 6.4: $(x, Q^2)$ *plane showing the shaded KP area, bounded by the electron energy isolines at 26 GeV and 27.5 GeV.*



The KP region can be isolated with appropriate cuts. First, all cuts described in the previous chapter, except for the $y_{JB}$ cut, are applied, in order to reject background and ensure a reliable reconstruction of the event kinematics. The $y_{JB}$ cut is necessary only in the double angle method, to ensure adequate resolution of the hadronic angle $\gamma$, as discussed in section 5.1. A cut is then made on $Q^2_{DA}$, which is required to lie between 10 GeV$^2$ and 100 GeV$^2$.

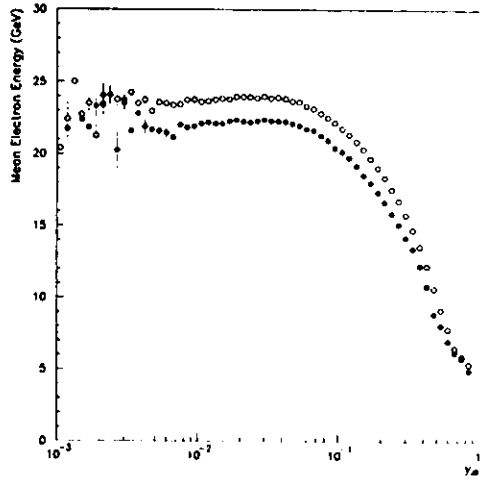


Figure 6.5: *Mean electron energy versus $y_{JB}$, after the $Q^2$ cut, for data (solid circles) and Monte Carlo (open circles) events.*

The mean scattered electron energy after the above selection is plotted in fig. 6.5, as a function of $y_{JB}$. It is evident that the electron energy becomes independent of $y_{JB}$, at low values of $y$. Thus, events in the KP region can be

selected by requiring $y_{JB} < 0.03$. In addition, this $y_{JB}$ cut ensures that the KP sample does not overlap with the Double Angle sample ($y_{JB} > 0.04$ for the Double Angle method).

Fig. 6.6 shows the generated Monte Carlo scattered electron energy distribution for KP events. The scattered electron spectrum peaks sharply at the electron beam energy. Therefore, the KP sample can be used as a "test beam" at 26.7 GeV to determine the electron energy loss seen in the calorimeter.

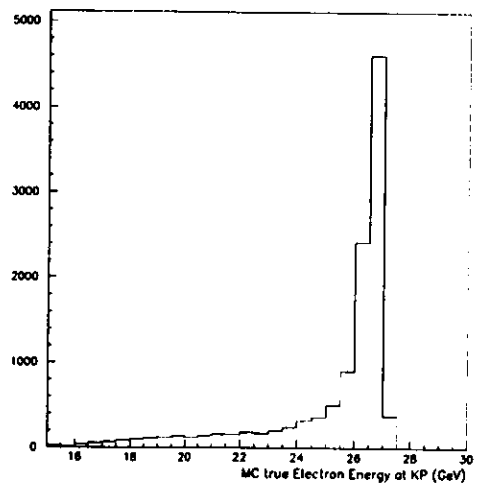


Figure 6.6: *Monte Carlo true electron energy for the KP sample.*



## 6.3 Electron Energy Correction Method

### 6.3.1 Principle

In order to correct the scattered electron energy for energy loss due to inactive material in front of the RCAL, we use the KP electrons to measure the calorimeter response at 26.7 GeV.

The sample is binned in scattered electron impact position on the face of the RCAL so that the average inactive material traversed by the electron before reaching the RCAL is approximately constant in the bin (see section 6.3.3). The measured deviation of the scattered KP electron energies from the electron beam energy ($E_e$), measures the energy loss of a 26.7 GeV electron when it traverses the inactive material.

The observed shift is compared to test beam data[17] which provide the energy loss of a 30 GeV electron as a function of the absorber thickness in front of the calorimeter modules. In this way, a map of the inactive material in front of the RCAL is produced. Consequently, test beam data, which provide the energy loss of an electron as a function of its energy and the material depth, is used to extract the corrected scattered electron energy from the calorimeter measured energy and the calculated inactive material.

The energy corrections are applied both to data and Monte Carlo events. Due to the inadequate description of the inactive material in front of the rear beampipe in the ZEUS detector simulation, the electron energy loss seen in the calorimeter is different for data and Monte Carlo events. Therefore, the obtained maps of inactive material, and the subsequent electron energy corrections according to these maps, are different for data and Monte Carlo.

### 6.3.2 Energy Loss Parametrization

The test beam measurements [47] for the response of the calorimeter to 30 GeV electrons as a function of the absorber thickness and as a function of the electron energy for various absorber thickness are parametrized with the function:

$$\frac{E_{corr}}{E_{meas}} = 1 + d(0.0037e^{1.79d}E_{meas}^{-2.75} + 0.054e^{0.58d}E_{meas}^{-0.54}), \qquad (6.1)$$

where $E_{meas}$ and $E_{corr}$ are the calorimeter measured and corrected energies of the scattered electron, respectively, and $d$ is the absorber thickness, measured in radiation lengths (r.l.). The function given in eq. (6.1) is plotted in fig. 6.7.

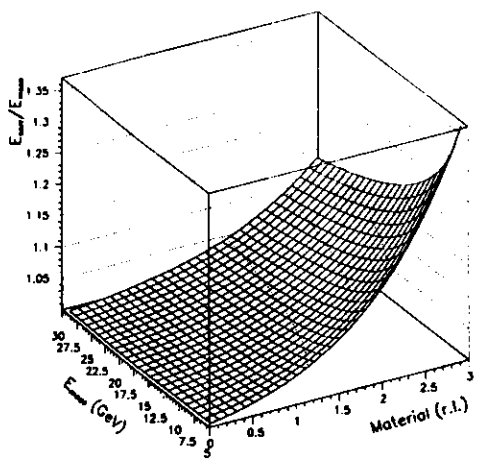


Figure 6.7: *Parametrization of the ratio $E_{corr}/E_{meas}$ in eq. (6.1), as a function of the material traversed (in radiation lengths) and of $E_{meas}$.*



### 6.3.3 Bin Selection and Dead Material Map

The correction bins are chosen on the face of the RCAL so that the average inactive material in front of the area covered by each bin is approximately constant. In practice, however, the choice of bin size is limited by statistics. The chosen bins are shown in fig. 6.8. They cover a square of 110 cm on each side centered around the RCAL beampipe. Outside this correction square the statistics is insufficient to implement the energy correction method.

The electron energy spectra in the chosen bins, for data and Monte Carlo (shown in figures 6.9 and 6.10, respectively) are fit with a gaussian with an exponential tail.

The maps of the inactive material, which are extracted from the energy loss in each bin, are shown in figures 6.11 and 6.12, for data and Monte Carlo, respectively. In the area around the RCAL beampipe, the inactive material extracted from the data is approximately 1 r.l. greater than the inactive material in the Monte Carlo.

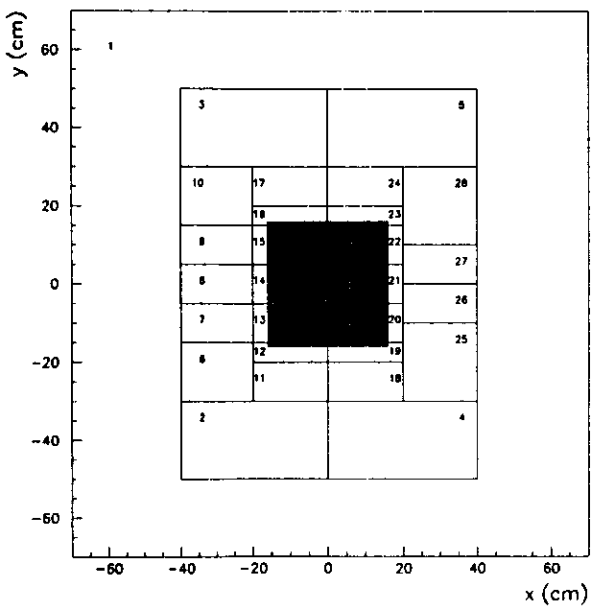


Figure 6.8: *The correction bins on the face of the RCAL. The solid area indicates the beampipe hole. The shaded area indicates the box cut of 16 cm.*



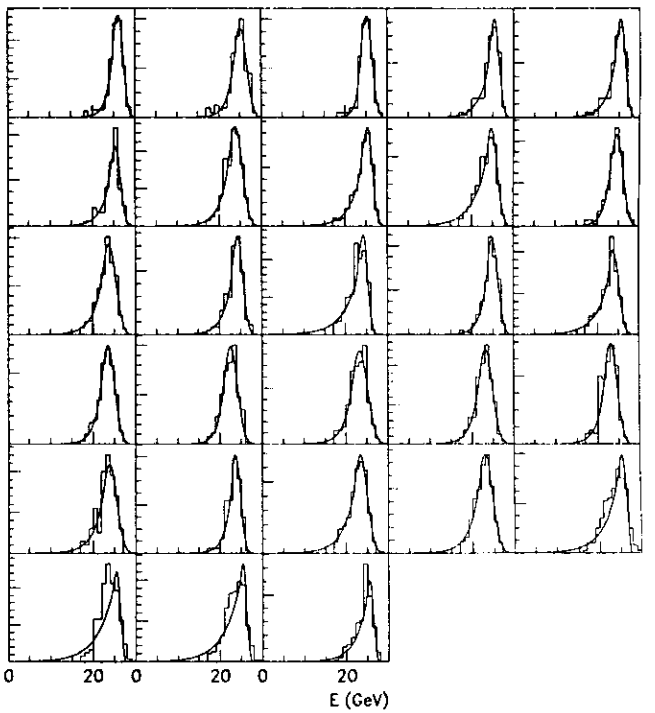


Figure 6.9: *The electron energy spectra in the correction bins, for the data KP sample. The histograms from left to right and top to bottom follow the numbering scheme of fig. 6.8, with the top left and bottom right histograms corresponding to bins 1 and 28, respectively.*

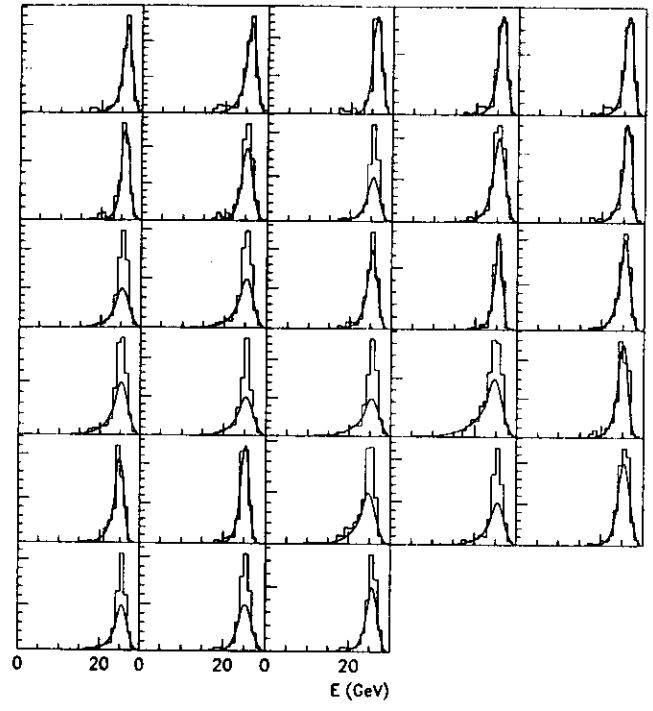


Figure 6.10: *The electron energy spectra in the correction bins, for the Monte Carlo KP sample. The histograms from left to right and top to bottom follow the numbering scheme of fig. 6.8, with the top left and bottom right histograms corresponding to bins 1 and 28, respectively.*



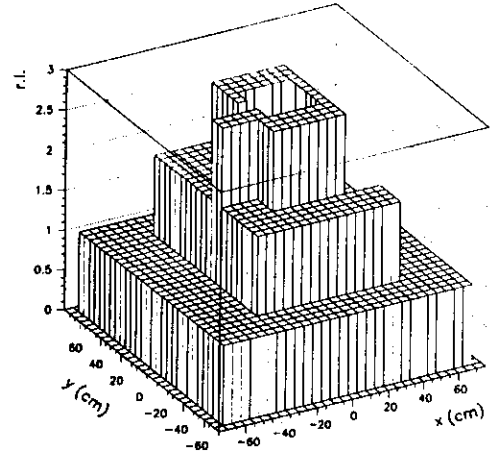


Figure 6.11: *Inactive material around the RCAL beampipe, for data.*

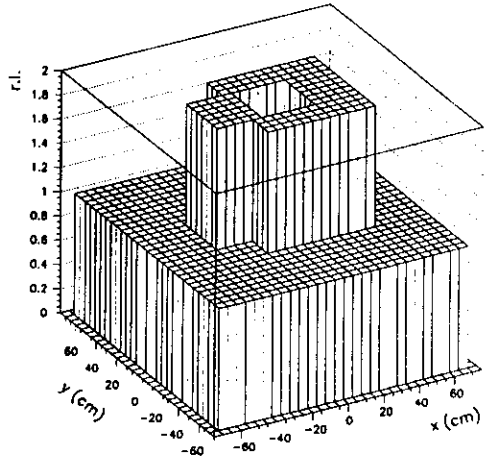


Figure 6.12: *Inactive material around the RCAL beampipe, for MC.*

### 6.3.4 Electron Energy Correction

The electron energy correction is applied separately to data and Monte Carlo events.

For data events, the scattered electron energy is corrected for energy loss in the inactive material in front of the RCAL using the following procedure. The impact point of the scattered electron, after being projected onto the face of the RCAL, determines the correction bin (see fig. 6.8). The inactive material $d$, that the electron has traversed before reaching the front of this specific RCAL bin, is read from the map of the inactive material for data (see fig. 6.11). The calorimeter measured energy, $E_{meas}$, and the thickness of the inactive material, $d$ (in r.l.), are inserted in eq. (6.1), which provides the corrected scattered electron energy.

The effect of the energy correction on the spectrum of the scattered electron energy for data events can be seen in fig. 6.13. The dashed line represents the calorimeter measured electron energy before correction. The solid line represents the corrected electron energy. The correction for the energy loss in the inactive material shifts the scattered electron energy to higher values. In order to account for this effect, we raise the electron energy selection cut from 5 GeV to 8 GeV. Since the scattered electron energy is included in the $\delta \equiv (E_{tot} - P_{z\,tot})$ distribution, the upper cut on $\delta$ is also shifted from 60 GeV to 65 GeV, in order to include the high energy tail of the distribution. The data sample used for both histograms in fig. 6.13 has been obtained by applying these higher cuts on corrected variables.

For Monte Carlo events, a similar procedure is followed. The impact point of the scattered electron, projected onto the face of the RCAL, determines the correction bin (see fig. 6.8). The inactive material $d$, that the electron has traversed before reaching the RCAL, is read from the map of the inactive material for Monte Carlo (see fig. 6.12). The calorimeter measured energy, $E_{meas}$, and the thickness of the inactive material, $d$ (in r.l.), are inserted in eq. (6.1), yielding the corrected scattered electron energy.



The effect of the energy correction on the spectrum of the scattered electron energy for Monte Carlo events can be seen in fig. 6.14. The dashed line represents the calorimeter measured electron energy before correction. The solid line represents the corrected electron energy. The dotted line gives the true generated electron energy. The correction for the energy loss in the inactive material shifts the electron energy to higher values, closer to the true generated energy. However, the shift is smaller for Monte Carlo events than for data events. This is expected, since the inactive material in the Monte Carlo is approximately 1 r.l. less than the inactive material extracted from the data, as shown by comparing figures 6.11 and 6.12. As is done for the data, the electron energy and the upper $\delta$ selection cuts are raised for the corrected Monte Carlo events from 5 GeV to 8 GeV and 60 GeV to 65 GeV, respectively. The Monte Carlo sample used for all three histograms in fig. 6.14 has been obtained by applying these modified cuts to the corrected reconstructed variables.

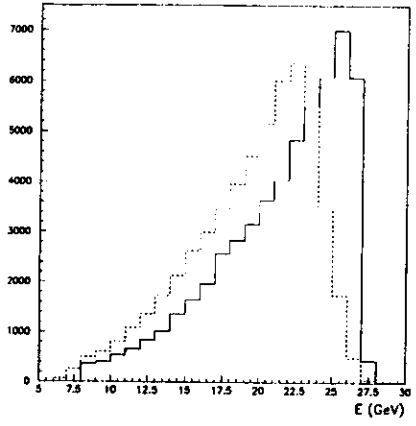


Figure 6.13: *Electron energy distribution, for data events, before (dashed line) and after (solid line) correction.*

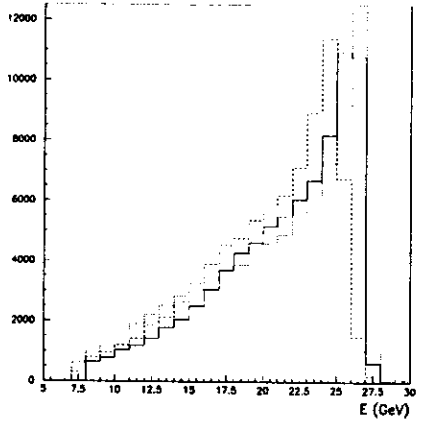


Figure 6.14: *Electron energy distribution, for Monte Carlo events, before (dashed line) and after (solid line) correction. Also shown (dotted line) is the true generated Monte Carlo scattered electron energy.*



### 6.3.5 Resolution Smearing in Monte Carlo

The energy resolution of the calorimeter is modified by the presence of absorber in front of the calorimeter. The resolution $\sigma$ as a function of the particle energy $E$ and the absorber thickness $d$, is given by:

$$\sigma(E,d) = 0.19\sqrt{E}\,(1+\sigma_d), \tag{6.2}$$

where:

$$\sigma_d = 0.02\,e^{0.7d}. \tag{6.3}$$

Eq. (6.3) is obtained from a fit to test beam data, which provide the resolution with and without absorber as function of the absorber thickness.[47]

Thus, the 1 r.l. additional inactive material around the RCAL beampipe yields a worse energy resolution for data events than for Monte Carlo events, in addition to the lower data energies.

The effect can be seen in figures 6.9 and 6.10 for the KP sample. The peaks of the electron energy are not only consistently lower in the data than in the Monte Carlo, but also broader.

In order to account for this effect, the electron energy in the Monte Carlo is smeared, bin by bin, after the energy correction. The smearing is done so that $\sigma_d^{MC}$ in each correction bin becomes equal to $\sigma_d^{data}$ in the corresponding bin.

Fig. 6.15 shows the corrected electron energy for Monte Carlo events after the MC resolution smearing (solid line). Also shown are the uncorrected electron energy (dashed line) and the true generated electron energy (dotted line). The Monte Carlo sample used for all three histrograms has been obtained by

applying the higher electron energy selection cut (8 GeV) to the corrected and resolution-smeared reconstructed electron energies.

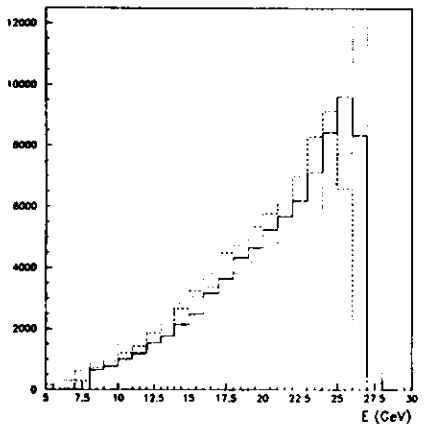


Figure 6.15: *Electron energy distribution, for Monte Carlo events, before (dashed line) and after (solid line) correction. Also shown (dotted line) is the true generated Monte Carlo scattered electron energy.*

### 6.3.6 Extension to the Whole Calorimeter

Outside the RCAL beampipe region, the KP sample does not provide enough statistics to extract a map of the inactive material. Thus, the Monte Carlo estimate is used for the rest of the calorimeter. This estimated inactive material was obtained by firing virtual Monte Carlo particles into the calorimeter, using the ZEUS detector simulation code, in order to determine the path-integrated inactive material traversed by the particles.



### 6.3.7 Final Correction Results

The electron energy response, after the electron energy corrections have been applied to both the data and Monte Carlo samples, is shown in fig. 6.16. The shaded area represents the corrected Monte Carlo energy with the smeared resolution, while the dashed line gives the same distribution without smearing. The points represent the corrected electron energy for data. The selection criteria are similar to those used in fig. 6.1 (i.e. all cuts for the Electron method have been applied). However, the values of the electron energy and $\delta$ selection cuts are raised to 8 GeV and 65 GeV, respectively, as explained in section 6.3.4. Fig. 6.16 includes events with the scattered electron anywhere in the calorimeter, and with $x$ and $Q^2$ over the whole $(x, Q^2)$ plane.

The $\delta$ distribution after the electron energy corrections is shown in fig. 6.17, while the corrected $x_{elec}$, $y_{elec}$ and $Q^2_{elec}$ are plotted in fig. 6.18. The selection criteria for these plots are the same as in fig. 6.16.

The electron energy resolution, as extracted from the difference between generated and reconstructed electron energies for Monte Carlo events, is:

$\sigma(E) = 1.319 \pm 0.006$ GeV,

for uncorrected electron energies,

$\sigma(E) = 1.251 \pm 0.005$ GeV,

for corrected electron energies, without MC resolution smearing, and

$\sigma(E) = 1.861 \pm 0.007$ GeV,

for corrected electron energies, with MC resolution smearing.

The energy and event kinematics distributions, as well as the statistics, for the final data sample, after the modified selection criteria, are given in the next chapter.

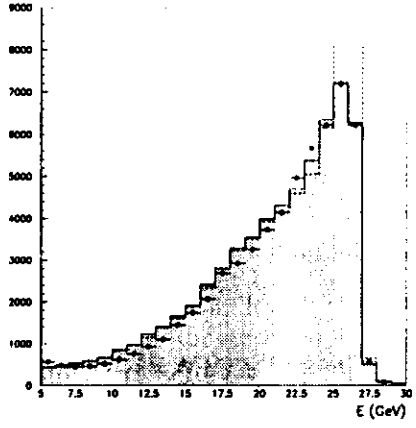


Figure 6.16: *Corrected electron energy distribution, for data (points) and Monte Carlo (shaded histogram) events, for the Electron method selected sample. The dashed line gives the corrected electron energy for Monte Carlo, without resolution smearing.*

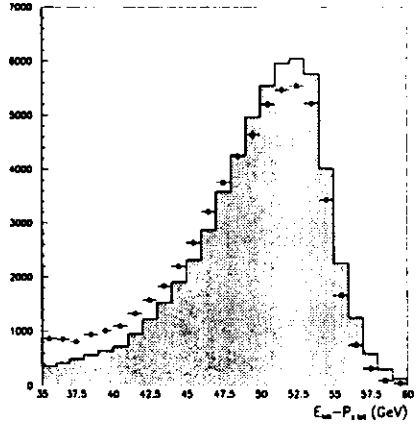


Figure 6.17: *Corrected $\delta$ distribution, for data (points) and Monte Carlo (shaded histogram) events, for the Electron method selected sample.*



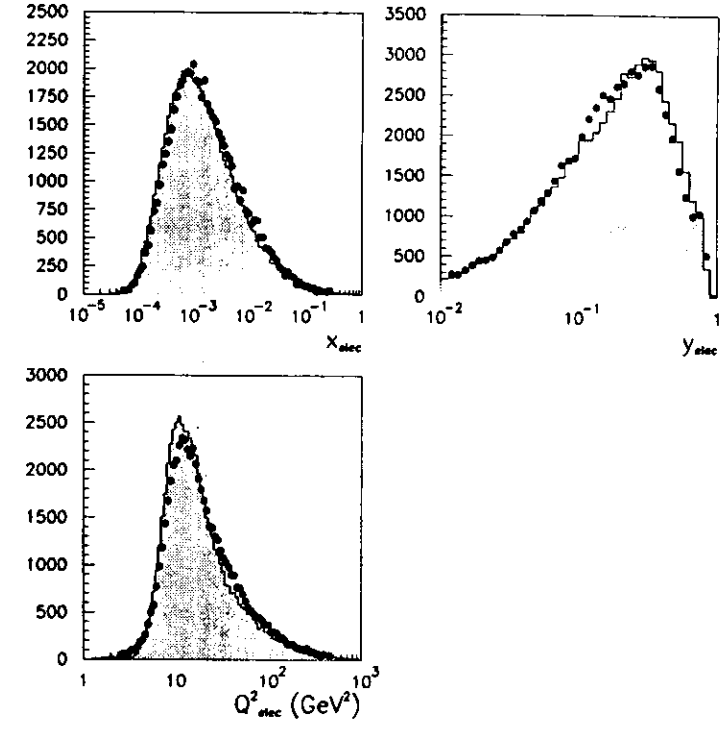


Figure 6.18: *Corrected $x, y, Q^2$ distributions, for data (points) and Monte Carlo (shaded histograms) events, for the Electron method selected sample.*

### 6.3.8 Checking the Correction Method

Three independent physics channels have been used to verify the accuracy of the electron energy corrections within the correction square in the RCAL.

- Elastic QED Compton events. The final state of these events consists of an electron and a photon, whose sum of energies (as measured by the calorimeter) must be approximately equal to the electron beam energy.
- Diffractive (see section 7.3) DIS $\rho$ events. Since these events have a clear hadronic final state (the $\rho$), energy and momentum conservation yield an estimate of the scattered electron energy, independently of the RCAL energy scale.
- ISR DIS events, with the radiative photon tagged by the luminosity $\gamma$-detector. The energy of the radiated photon can be reconstructed using calorimeter quantities, and compared to the energy measured by the luminosity $\gamma$-detector.

All channels yield an accuracy of about 1% [18] for the RCAL electron energy corrections.



# Chapter 7

# The Final Sample

## 7.1 Electron method

The scattered electron energy, $E'$, for the Electron method data and Monte Carlo samples, is corrected with the energy correction method described in the previous chapter. The variables $\delta$, $x_{elec}$, $y_{elec}$ and $Q^2_{elec}$ of each event are calculated using the corrected electron energy. The cuts on $E'$ and $\delta$ are raised to 8 GeV and 65 GeV (upper cut), respectively, as explained in section 6.3.1.

The resolution plots for $Q^2_{elec}$, $x_{elec}$ and $y_{elec}$, extracted from the selected Monte Carlo sample, are shown before correction in fig. 7.1 and after correction in fig. 7.2. Comparing the uncorrected distributions of fig. 7.1 with the resolution plots of fig. 4.3 for the initial Monte Carlo sample, it is seen that the selection criteria considerably improve the resolution of the kinematic reconstruction, especially in the low-$x$, low-$Q^2$ region. Fig. 7.2 shows the resolution plots for the corrected $Q^2_{elec}$, $x_{elec}$ and $y_{elec}$ distributions. The electron energy correction worsens the resolution somewhat, since it accounts for additional inactive material. The effect is more pronounced in the high-$x$, low-$y$ region; the higher corrected electron energy reconstructs $x_{elec}$ to higher values, and $y_{elec}$ to lower values (see equations (1.3) and (1.4)).

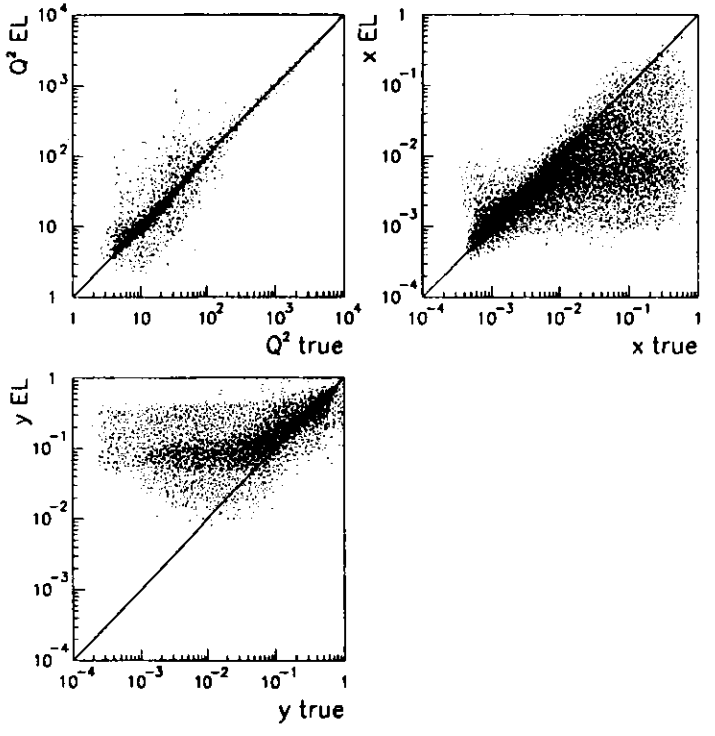


Figure 7.1: *Resolution of the Electron method in $Q^2$, $x$ and $y$, extracted from the selected Monte Carlo sample, before the electron energy correction is applied.*



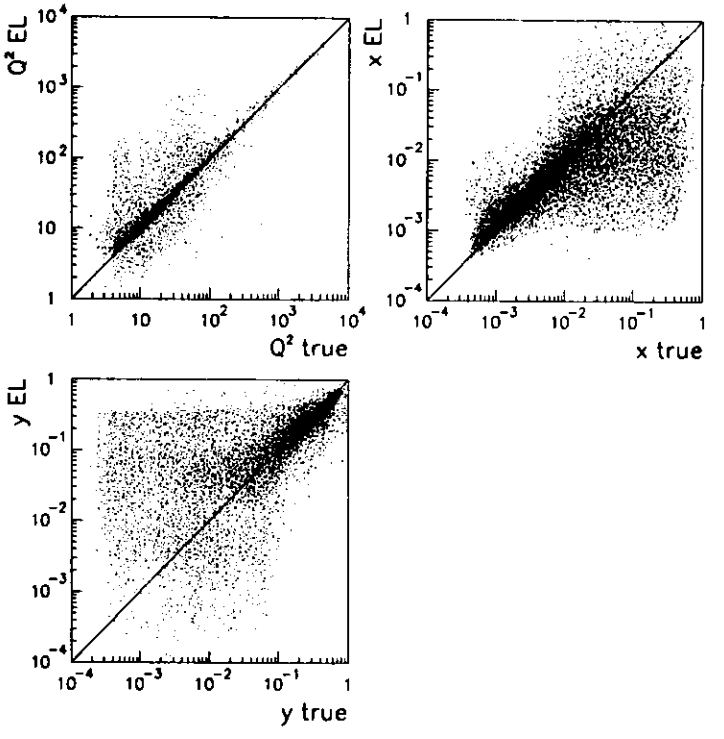


Figure 7.2: *Resolution of the Electron method in $Q^2$, $x$ and $y$, extracted from the selected Monte Carlo sample, after the electron energy correction is applied.*

The number of events of the final data sample for the Electron method, as well as the estimated background in the final sample, are given in table 7.1.

| | Electron method | |
|---|---|---|
| | Final sample | |
| Data | 57,334 | |
| estimated e-gas bkgd | 507 | 0.88% |
| estimated p-gas bkgd | 223 | 0.39% |
| estimated PHP bkgd | 900 | 1.57% |

Table 7.1: *Statistics of the final data sample for the Electron method.*

The vertex reconstruction efficiencies, using tracking and calorimeter timing information, for the final Electron method data and Monte Carlo samples, are given in table 7.2. The corresponding efficiencies for the initial data and Monte Carlo samples were given in table 5.1.

| | Electron method | |
|---|---|---|
| | Data - final | DIS MC - final |
| Tracking vertex | 86.3% | 90.1% |
| CAL Time vertex | 11.7% | |
| no vertex | 2.0% | 9.9% |

Table 7.2: *Vertex reconstruction efficiencies, for the final Electron method data and Monte Carlo samples.*



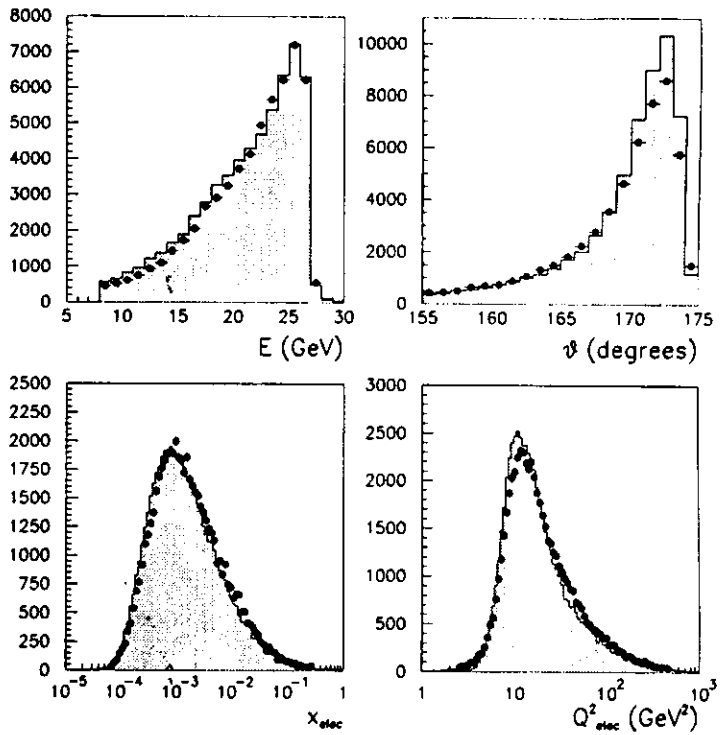


Figure 7.3: *Distributions of the scattered electron energy and polar angle, E and θ, respectively, and the reconstructed $x_{elec}$ and $Q^2_{elec}$, for the final Electron method data (points) and Monte Carlo (shaded histograms) samples, after the electron energy correction.*

Fig. 7.3 shows the scattered electron energy $E'$, the scattered electron polar angle $\theta$, and the reconstructed $x_{elec}$ and $Q^2_{elec}$, for the final Electron method data and Monte Carlo samples. There is a good agreement between data and Monte Carlo, in the electron energy and the kinematic distributions, after the electron energy correction. The agreement is worse in the distribution of the scattered electron polar angle. However, the effect is covered by a systematic check on the electron angle (see section 8.6).

The impact point of the scattered electron, on the face of the RCAL, for the final Electron method data sample, is shown in fig. 7.4. The fiducial cut of 16 cm around the beam-pipe is clearly seen.

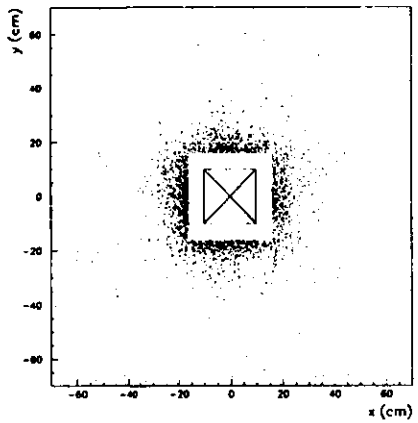


Figure 7.4: *The impact point of the scattered electron on the face of the RCAL, for the final Electron method data sample.*



## 7.2 Double Angle method

The electron energy response has only a secondary effect on the reconstruction of the kinematics with the Double Angle method: it enters through the selection criteria on $E'$, $\delta$ and $y_{elec}$. In correcting the electron energy, the amount of inactive material outside the square of side 140 cm around the RCAL beampipe has been estimated from Monte Carlo, rather than calculated from the energy loss of the Kinematic Peak sample, due to limited statistics (see section 6.3.5). Therefore, the corrections are less reliable for the rest of the calorimeter than for the RCAL beampipe region. Since the effect of the electron energy response is much smaller for the Double Angle method than for the Electron method, the uncorrected $E'$, $\delta$ and $y_{elec}$ are used in the event selection for the Double Angle method, for the whole calorimeter.

The resolution plots for $Q^2_{DA}$, $x_{DA}$ and $y_{DA}$, as extracted from the final Monte Carlo sample, are shown in fig. 7.5. The resolution in $x$ in the low-$x$ region is worse in the Double Angle method than in the Electron method, as can be seen by comparing fig. 7.5 with figures 7.1 and 7.2. The effect of the imposed $y_{JB}$ cut can be seen in the $y$ resolution plot of fig. 7.5.

The number of events of the final data sample for the Double Angle method is given in table 7.3, along with the estimated background in the final sample.

The efficiencies for the vertex reconstruction, using tracking and calorimeter timing information, for the final Double Angle method data and Monte Carlo samples, are given in table 7.4. The corresponding efficiencies for the initial data and Monte Carlo samples were given in table 5.1. The efficiencies improve significantly after the event selection.

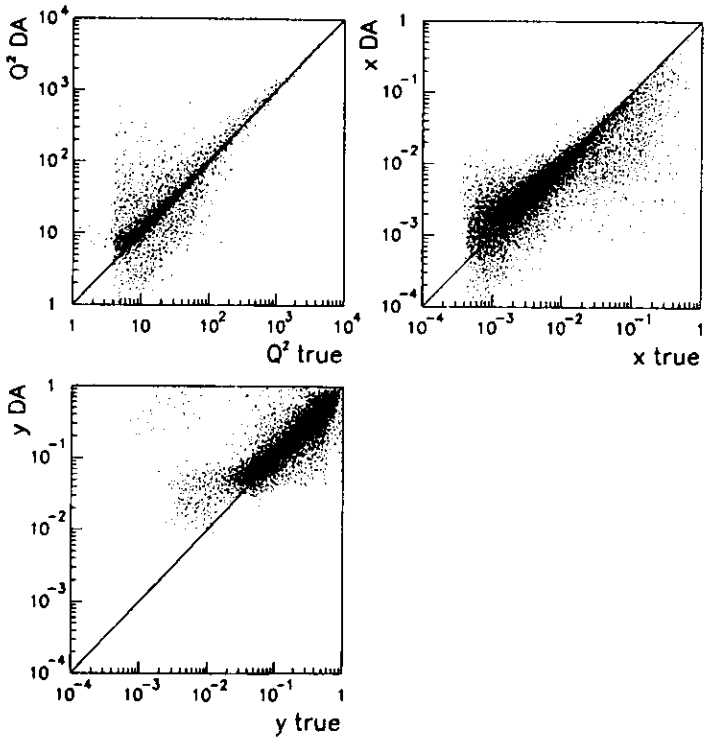


Figure 7.5: *Resolution of the Double Angle method in $Q^2$, $x$ and $y$, extracted from the final Monte Carlo sample.*



The scattering angles of the outgoing electron and the final state hadron system, together with the reconstructed $x_{DA}$ and $Q^2_{DA}$, for the final Double Angle method data and Monte Carlo samples, are shown in fig. 7.6. There is a good agreement between data and Monte Carlo for the angle of the final hadronic system, and $x_{DA}$. The agreement is worse for the distribution of the polar angle of the scattered electron, which also affects the $Q^2_{DA}$ distribution. However, this effect is included in the systematic error for the electron angle (see section 8.6).

| | Double Angle method | |
|---|---|---|
| | Final sample | |
| Data | 41,513 | |
| estimated $e$-gas bkgd | 246 | 0.59% |
| estimated $p$-gas bkgd | 108 | 0.26% |
| estimated PHP bkgd | 653 | 1.57% |

Table 7.3: *Statistics of the final data sample for the Double Angle method.*

| | Double Angle method | |
|---|---|---|
| | Data - final | DIS MC - final |
| Tracking vertex | 98.8% | 99.7% |
| CAL Time vertex | 0.6% | |
| no vertex | 0.6% | 0.3% |

Table 7.4: *Vertex reconstruction efficiencies, for the final Double Angle method data and Monte Carlo samples.*

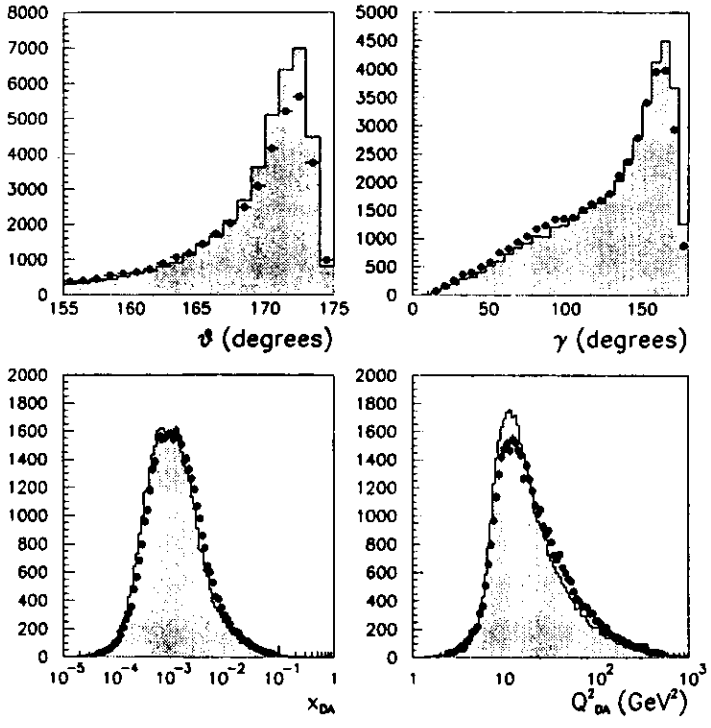


Figure 7.6: *Distributions of the final state electron and hadron system polar angles, $\theta$ and $\gamma$, respectively, and the reconstructed $x_{DA}$ and $Q^2_{DA}$, for the final Double Angle method data (points) and Monte Carlo (shaded histograms) samples.*



## 7.3 Events with a Large Rapidity Gap

In regular deep inelastic electron-proton scattering, the proton breaks up, and the incident electron scatters off a colored quark inside the proton. The color transfer between the struck quark and the remnant of the proton results in the production of the final state hadron system (current and remnant jets). The remnant jet is emitted in the forward (proton beam) direction, and results in considerable amounts of energy deposited around the FCAL beampipe.

However, there is a type of DIS event (first observed in the 1992 HERA data[49]) which exhibits very little activity in the forward direction (low FCAL energies). This can be explained by the assumption that the virtual photon scatters off a colorless object inside the incident proton. The proton remains, in most of the cases, intact and is lost in the forward beampipe direction.

The Feynman diagram for this type of event is shown in fig. 7.7. In this diagram, $I\!P$ represents the colorless object in the proton, off which the virtual photon scatters. The squared 4-momentum transfer at the proton vertex is denoted by $t$, while $Q^2$ represents the usual negative squared 4-momentum transfer carried by the virtual photon, which is now measured only at the electron vertex.

A selection method for this type of event is to impose a cut on the maximum pseudorapidity $\eta_{max}$. The pseudorapidity of a hadronic cluster is defined as

$$\eta = -\ln[\tan(\theta_h/2)], \tag{7.1}$$

where $\theta_h$ is the polar angle of the hadronic cluster. The cluster is required to have an energy of at least 400 MeV. The maximum pseudorapidity of an event, $\eta_{max}$, is defined as the pseudorapidity of the hadronic cluster which is

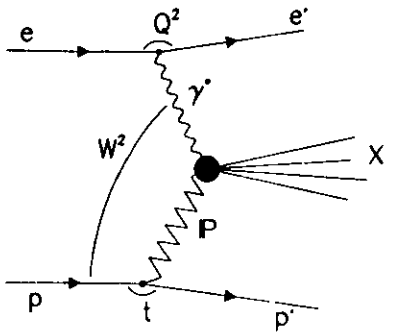


Figure 7.7: *Feynman diagram of a Large Rapidity Gap event*

closest to the proton beam direction.

The $\eta_{max}$ distribution for the final Electron method data and Monte Carlo samples is shown in fig. 7.8. There is an excess of data events with low values of $\eta_{max}$ (i.e. events with an absence of hadronic activity in the forward direction), which is not expected in the standard DIS Monte Carlo. These events, with a large rapidity gap in the final phase space, are also called *diffractive*, because of the clear separation between the final state proton and the photon dissociation.

If we impose a cut of $\eta_{max} < 1.5$ we find that the diffractive events account for 6.2% of the final Electron method data sample, and for 6.5% of the final Double Angle method data sample. However, since the $F_2$ proton structure function corresponds to the inclusive DIS cross section, which is independent of the form of the final hadronic state, the diffractive events are included in the $F_2$ measurement.



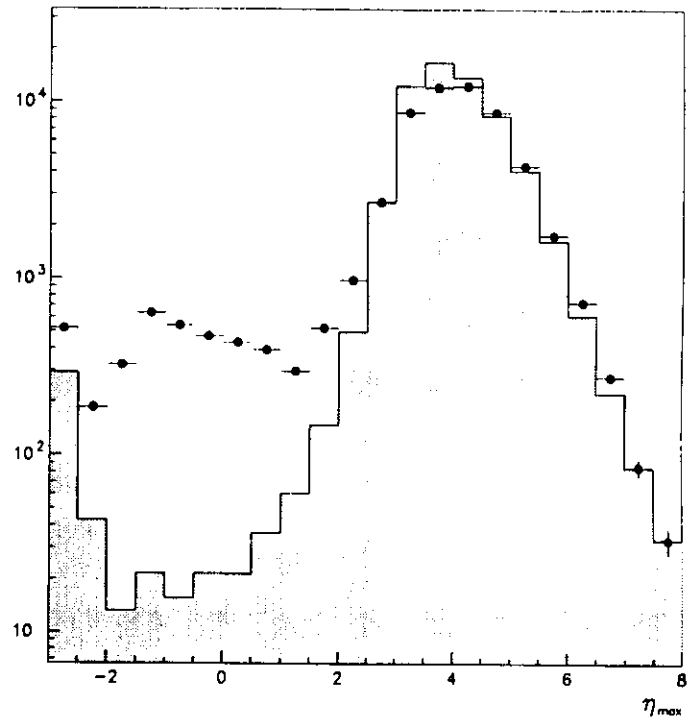


Figure 7.8: *The $\eta_{max}$ distribution for the final Electron method data (points) and Monte Carlo (shaded histogram) samples. The Monte Carlo sample is normalized to the data.*

# Chapter 8

# $F_2$ Extraction

## 8.1 Description of the method

The differential NC $ep$ cross section is given, in its general form, by eq. (1.38). At $Q^2$ values below the square of the mass of the $Z^o$, the structure function $x\mathcal{F}_3$ is negligible and the structure functions $\mathcal{F}_2$ and $\mathcal{F}_L$ reduce to their virtual photon contributions only, $F_2$ and $F_L$, respectively. Then the differential cross section is given by:

$$\frac{d^2\sigma}{dxdQ^2} = \frac{4\pi\alpha^2}{xQ^4}[(1-y+y^2/2)\,F_2(x,Q^2) - (y^2/2)\,F_L(x,Q^2)]. \qquad (8.1)$$

Eq. (8.1) can be written in the form:

$$\frac{d^2\sigma}{dxdQ^2} = \frac{4\pi\alpha^2(1-y+y^2/2)}{xQ^4}\,F_2'(x,Q^2), \qquad (8.2)$$

where $F_2'$ is given by:

$$F_2'(x,Q^2) = F_2(x,Q^2) - \frac{y^2/2}{1-y+y^2/2}\,F_L(x,Q^2). \qquad (8.3)$$

Hence, the structure function $F_2$ can be extracted by first measuring the differential cross section, and then applying $F_L$ corrections to $F_2'$.

The method is briefly outlined here. Exact definitions and values of variables and selection criteria are given in the following sections.



In order to measure the differential cross section, we divide the data into $x$ and $Q^2$ bins. For each bin, we calculate a number of correction factors, using the Monte Carlo sample: a smearing factor due to initial and final state radiation, a smearing factor due to detector effects, and an acceptance factor. A purity factor is also evaluated for each bin. Selection criteria are applied on all the above factors, in order to determine the bins suitable for $F_2$ extraction. For each of those bins, the raw number of data events, after the estimated background has been subtracted, is corrected for smearing and acceptance effects. Since the Monte Carlo includes radiative events, the measured number of data events in each bin is also corrected to the Born cross section. The corrected number of data events in each bin is converted to a differential cross section, using the luminosity of the data and appropriate bin widths.

Subsequently, the differential cross section in each bin is weighted by the factor W

$$W(x,Q^2) = \frac{xQ^2}{4\pi\alpha^2(1-y+y^2/2)} \qquad (8.4)$$

in order to evaluate $F_2'$.

Finally, $F_2'$ is corrected to $F_2$, using QCD calculations of $F_L$.

## 8.2 Choice of $(x, Q^2)$ Bins

The bins in the $x$ and $Q^2$ phase space are chosen according to the resolutions in $x$ and $Q^2$. Limited statistics determines the size of the bins at high $Q^2$.

The resolutions in $x$ and $Q^2$, for the Electron and Double Angle final Monte Carlo samples, are shown in fig. 8.1. The relative differences between reconstructed and generated $x$ and $Q^2$ are plotted as functions of the reconstructed quantities. For both the Electron and Double Angle methods the relative resolution in $Q^2$ is 25%, independent of $Q^2$. Thus, the same $Q^2$ binning can be used for both methods. The relative resolution in $x$ is around 20% for both methods at intermediate values of $x$. At low values of $x$ the Electron method has a better $x$ resolution than the Double Angle method. However, the difference is rather small, due to the degradation of the energy resolution caused by the inactive material in front of the RCAL (which is not completely recovered by the electron energy correction), and to the additional smearing of the energy resolution introduced in the Monte Carlo. Therefore, the same binning also in $x$ is used for both methods.

The chosen $x$ and $Q^2$ bins are given in tables 8.1 and 8.2, respectively. For each bin the range in $x$ and $Q^2$ is given, along with the central $x$ and $Q^2$ value in the bin, $x_{center}$ and $Q^2_{center}$. The cental values are used to denote the bins in all the following sections, and are the $x$ and $Q^2$ values where the final $F_2$ is calculated. It has to be noted that $Q^2_{center}$ is chosen to differ slightly from the actual center of the $Q^2$ bins, so that the final $F_2$ results can be compared with other experimental sets.



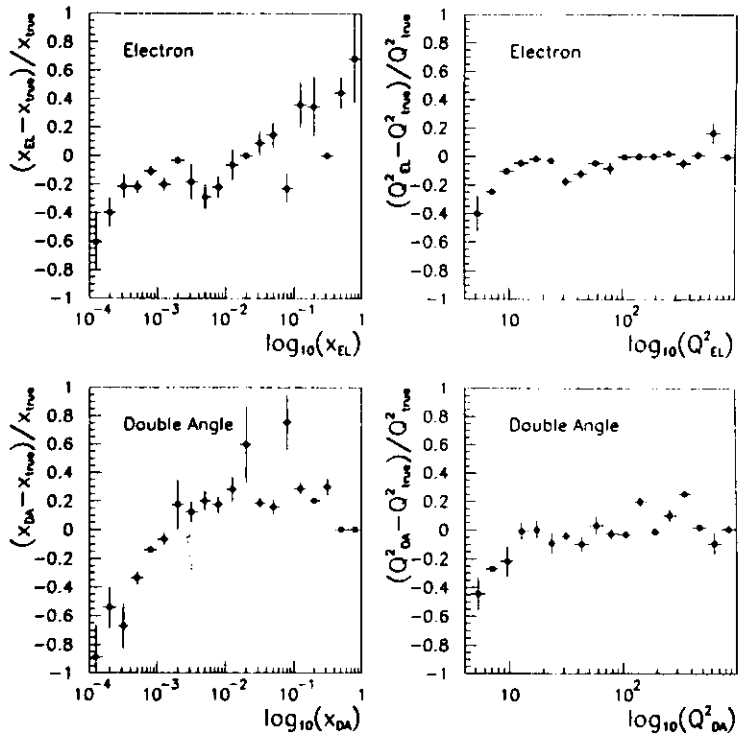


Figure 8.1: *Relative resolutions in $x$ and $Q^2$ of the Electron and Double Angle methods, as functions of the reconstructed variables.*

| | $x$ range | $x_{center}$ |
|---|---|---|
| 1 | $7.0-15.0 \cdot 10^{-5}$ | $1.1 \cdot 10^{-4}$ |
| 2 | $1.5-3.0 \cdot 10^{-4}$ | $2.25 \cdot 10^{-4}$ |
| 3 | $3.0-6.0 \cdot 10^{-4}$ | $4.5 \cdot 10^{-4}$ |
| 4 | $6.0-12.0 \cdot 10^{-4}$ | $9.0 \cdot 10^{-4}$ |
| 5 | $1.2-2.0 \cdot 10^{-3}$ | $1.6 \cdot 10^{-3}$ |
| 6 | $2.0-3.6 \cdot 10^{-3}$ | $2.8 \cdot 10^{-3}$ |
| 7 | $3.6-6.0 \cdot 10^{-3}$ | $4.8 \cdot 10^{-3}$ |
| 8 | $6.0-10.0 \cdot 10^{-3}$ | $8.0 \cdot 10^{-3}$ |
| 9 | $1.0-2.0 \cdot 10^{-2}$ | $1.5 \cdot 10^{-2}$ |
| 10 | $2.0-4.0 \cdot 10^{-2}$ | $3.0 \cdot 10^{-2}$ |
| 11 | $4.0-8.0 \cdot 10^{-2}$ | $6.0 \cdot 10^{-2}$ |
| 12 | $8.0-16.0 \cdot 10^{-2}$ | $1.2 \cdot 10^{-1}$ |
| 13 | $1.6-3.2 \cdot 10^{-1}$ | $2.4 \cdot 10^{-1}$ |
| 14 | $3.2-10.0 \cdot 10^{-1}$ | $6.6 \cdot 10^{-1}$ |

Table 8.1: *Definition of the bins in $x$.*



| | $Q^2$ range (GeV$^2$) | $Q^2_{center}$ (GeV$^2$) |
|---|---|---|
| 1 | 5 - 7 | 6 |
| 2 | 7 - 10 | 8.5 |
| 3 | 10 - 14 | 12 |
| 4 | 14 - 20 | 15 |
| 5 | 20 - 28 | 25 |
| 6 | 28 - 40 | 35 |
| 7 | 40 - 56 | 50 |
| 8 | 56 - 80 | 65 |
| 9 | 80 - 160 | 125 |
| 10 | 160 - 320 | 250 |
| 11 | 320 - 640 | 500 |
| 12 | 640 - 1280 | 1000 |
| 13 | 1280 - 2560 | 2000 |
| 14 | 2560 - 10000 | 5000 |

Table 8.2: *Definition of the bins in $Q^2$.*

## 8.3 Correction Factors and Bin Selection

A number of correction factors are evaluated for each $(x, Q^2)$ bin, using the Monte Carlo sample. Recall that the DIS NC Monte Carlo includes QED radiative processes in the cross section, as calculated by HERACLES (see section 3.1).

**• Smearing due to QED Radiative processes**

QED radiative processes shift the reconstructed kinematic variables, as discussed in section 4.2. For radiative Monte Carlo events, we denote by *true* the generated kinematic variables calculated from the 4-vector momenta of the particles at the lepton or hadron vertex, including the effects of QED radiation, and by *apparent* the generated kinematic variables calculated from the initial 4-vector momenta of the particles, without taking into account the QED radiation. Then, the *radiation smearing factor* is defined as the ratio of the true generated to the apparent generated number of DIS Monte Carlo events in the bin that pass all selection criteria:

$$\text{RadSmr} = \frac{dN(MC, true, cuts)}{dN(MC, app, cuts)} \tag{8.5}$$

**• Smearing due to Detector effects**

Detector smearing effects on the measurement of the energies and angles of the final state particles shift the reconstructed kinematic variables, as discussed in section 4.3. The *experimental smearing factor* is defined as the ratio of the apparent generated to the reconstructed number of DIS Monte Carlo events in the bin that pass all selection criteria:



$$\text{ExpSmr} = \frac{dN(MC, app, cuts)}{dN(MC, rec, cuts)} \tag{8.6}$$

**• Acceptance due to selection**

The *selection acceptance factor* is defined as the ratio of the true generated number of DIS Monte Carlo events in the bin to the true generated number of events that remain in the bin after all selection criteria have been applied:

$$\text{SelAcc} = \frac{dN(MC, true, no\ cuts)}{dN(MC, true, cuts)} \tag{8.7}$$

Defined in this way, the SelAcc factor is always greater than 1.

**• QED Radiative corrections**

QED radiative processes modify the Born cross section, in addition to smearing the kinematic variables, as discussed in section 1.7. In order to evaluate this effect, we define the *radiative correction factor* as the ratio of the Born cross section to the DIS Monte Carlo cross section in the bin. The latter includes radiative processes. The ratio is calculated in terms of the true variables, before any selection criteria are applied:

$$\text{RadCor} = \frac{\mathcal{L}_{MC}}{\mathcal{L}_{Born}} \cdot \frac{dN(Born, true, no\ cuts)}{dN(MC, true, no\ cuts)} \tag{8.8}$$

where $\mathcal{L}_{MC}$ and $\mathcal{L}_{Born}$ denote the integrated luminosity of the DIS MC sample and the Born cross section MC sample, respectively. In order to evaluate the Born cross section we generated a sample of 100k DIS events using LEPTO (see chapter 3), with only the Born cross section turned on.

**• Purity**

The quality of the reconstruction is evaluated in terms of purity, defined as

the fraction of the Monte Carlo events reconstructed in a bin that were also generated in the same bin:

$$\text{Purity} = \frac{dN(MC, true.and.rec, cuts)}{dN(MC, rec, cuts)} \tag{8.9}$$

Purity is by definition less than 1.

An $F_2$ value is calculated only in the $(x, Q^2)$ bins that satisfy the following criteria:

$$0.5 \leq \text{TotSmr} = \text{RadSmr} \cdot \text{ExpSmr} \leq 2 \tag{8.10}$$

$$1 \leq \text{SelAcc} \leq 2 \tag{8.11}$$

$$\text{Purity} \geq 0.2 \tag{8.12}$$

$$dN(MC, rec, cuts) \geq 10 \tag{8.13}$$

$$dN(data, cuts) \geq 10 \tag{8.14}$$

where the number of data events in the bin is considered after background subtraction. A minimum number of MC events in the bin is also required, to ensure a reliable evaluation of the bin correction factors.

For most of the selected $(x, Q^2)$ bins the TotSmr factor is around 0.8. The SelAcc correction factors are close to 1 in most of the bins, except in the low-$x$, low-$Q^2$ bins, where they become larger (around 1.5). Purity is low (30%-40%) in the low-$Q^2$ or low-$y$ bins in the Electron method. In the rest of the Electron method bins and in most of the Double Angle method bins, purity is about 50%. Radiative corrections, which are important especially in the Electron method, are of the order of a few percent in most of the selected bins, for both methods.



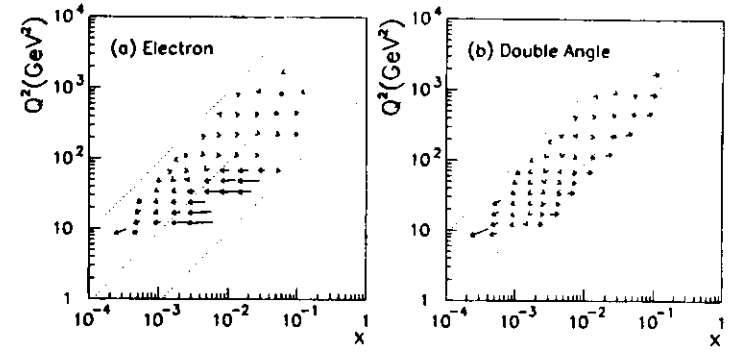


Figure 8.2: *Migrations of the Electron and Double Angle methods, in the $(x, Q^2)$ bins that satisfy the bin selection criteria. The dotted lines represent the $y = 1, 0.1, 0.01$ boundaries.*

The migrations (see section 1.3) for the $(x, Q^2)$ bins that satisfy the above criteria are shown in fig. 8.2. The length of the arrow is proportional to the shift of mean reconstructed variables. The migrations for the selected bins are much smaller than the migrations extracted from the initial Monte Carlo sample, as can be seen by comparing fig. 8.2 with fig. 1.4. The Electron method has somewhat smaller migrations than the Double Angle method in the low-$x$ bins, but the difference is minimized by the degradation of the electron energy resolution caused by the inactive material in front of the RCAL. In the high-$x$ bins the poorer Electron method resolution in $x$ causes larger migrations.

One more consideration about the bin selection for the Electron method has to be taken into account. The electron energy corrections are less reliable outside the RCAL correction square (see section 6.3.3), since the amount of the inactive material for the rest of the calorimeter has been estimated from Monte Carlo rather than calculated from the Kinematic Peak sample (see section 6.3.6). Therefore, we choose to report an Electron method $F_2$ value only for electron impact positions within the RCAL correction square, which corresponds to $Q^2$ values less than 80 GeV$^2$.

The correction factors for the selected bins are given in tables 8.3 and 8.4, for the Electron and Double Angle Monte Carlo samples, respectively. The number of Monte Carlo and data events in each bin, which are used in the bin selection procedure, are given in tables 8.5 and 8.6, for the Electron and Double Angle samples, respectively.



| Electron method | | | | | | | |
|---|---|---|---|---|---|---|---|
| $Q^2$ (GeV$^2$) | $x$ | RadSmr | ExpSmr | TotSmr | SelAcc | RadCor | Purity |
| 8.5 | 0.00023 | 0.81 | 1.27 | 1.07 | 1.79 | 1.01 | 0.45 |
| | 0.00045 | 0.87 | 0.82 | 0.71 | 1.85 | 1.09 | 0.38 |
| 12 | 0.00045 | 0.82 | 0.92 | 0.75 | 1.27 | 1.01 | 0.41 |
| | 0.00090 | 0.87 | 0.88 | 0.77 | 1.28 | 0.98 | 0.39 |
| | 0.00160 | 0.96 | 0.85 | 0.82 | 1.38 | 0.96 | 0.25 |
| | 0.00280 | 1.05 | 0.76 | 0.81 | 1.61 | 0.91 | 0.21 |
| 15 | 0.00045 | 0.83 | 1.12 | 0.92 | 1.38 | 0.96 | 0.49 |
| | 0.00090 | 0.86 | 0.87 | 0.75 | 1.07 | 1.03 | 0.41 |
| | 0.00160 | 0.91 | 0.93 | 0.85 | 1.07 | 0.90 | 0.33 |
| | 0.00280 | 0.95 | 0.83 | 0.79 | 1.13 | 0.93 | 0.21 |
| 25 | 0.00045 | 0.85 | 1.15 | 0.98 | 1.97 | 0.92 | 0.52 |
| | 0.00090 | 0.84 | 0.97 | 0.82 | 1.10 | 0.98 | 0.48 |
| | 0.00160 | 0.88 | 0.94 | 0.83 | 1.03 | 1.03 | 0.40 |
| | 0.00280 | 0.92 | 0.94 | 0.87 | 1.03 | 0.94 | 0.32 |
| 35 | 0.00090 | 0.84 | 1.00 | 0.84 | 1.17 | 0.98 | 0.57 |
| | 0.00160 | 0.87 | 0.94 | 0.81 | 1.03 | 1.02 | 0.47 |
| | 0.00280 | 0.88 | 1.04 | 0.91 | 1.02 | 1.03 | 0.44 |
| | 0.00480 | 0.98 | 0.89 | 0.87 | 1.04 | 0.99 | 0.28 |
| | 0.00800 | 1.03 | 0.83 | 0.85 | 1.17 | 0.85 | 0.20 |
| | 0.01500 | 1.17 | 0.91 | 1.07 | 1.37 | 0.91 | 0.23 |

Table 8.3: *Correction Factors for the Electron method selected $(x, Q^2)$ bins.*

| Electron method | | | | | | | |
|---|---|---|---|---|---|---|---|
| $Q^2$ (GeV$^2$) | $x$ | RadSmr | ExpSmr | TotSmr | SelAcc | RadCor | Purity |
| 50 | 0.00090 | 0.88 | 0.96 | 0.85 | 1.52 | 1.04 | 0.61 |
| | 0.00160 | 0.86 | 0.99 | 0.85 | 1.04 | 1.02 | 0.55 |
| | 0.00280 | 0.88 | 0.96 | 0.84 | 1.02 | 1.03 | 0.52 |
| | 0.00480 | 0.94 | 0.93 | 0.87 | 1.01 | 0.85 | 0.35 |
| | 0.00800 | 0.99 | 0.88 | 0.87 | 1.05 | 1.01 | 0.25 |
| | 0.01500 | 1.09 | 0.91 | 0.99 | 1.20 | 0.94 | 0.25 |
| 65 | 0.00160 | 0.89 | 0.92 | 0.82 | 1.05 | 0.94 | 0.58 |
| | 0.00280 | 0.84 | 0.94 | 0.79 | 1.01 | 1.13 | 0.52 |
| | 0.00480 | 0.89 | 0.94 | 0.84 | 1.01 | 1.02 | 0.41 |
| | 0.00800 | 0.96 | 0.79 | 0.75 | 1.01 | 1.05 | 0.30 |
| | 0.01500 | 0.96 | 0.80 | 0.77 | 1.05 | 1.03 | 0.22 |
| | 0.03000 | 1.13 | 0.86 | 0.98 | 1.19 | 0.87 | 0.20 |
| | 0.06000 | 1.22 | 1.47 | 1.80 | 1.43 | 0.85 | 0.20 |

Table 8.3: *Correction Factors for the Electron method selected $(x, Q^2)$ bins.*



| Double Angle method | | | | | | | |
|---|---|---|---|---|---|---|---|
| $Q^2$ (GeV$^2$) | $x$ | RadSmr | ExpSmr | TotSmr | SelAcc | RadCor | Purity |
| 8.5 | 0.00023 | 0.87 | 1.27 | 1.10 | 1.77 | 1.01 | 0.16 |
| | 0.00045 | 0.97 | 0.83 | 0.81 | 1.85 | 1.09 | 0.43 |
| 12 | 0.00045 | 0.89 | 0.98 | 0.87 | 1.27 | 1.01 | 0.33 |
| | 0.00090 | 0.98 | 0.79 | 0.77 | 1.28 | 0.98 | 0.39 |
| | 0.00160 | 1.15 | 0.67 | 0.77 | 1.39 | 0.96 | 0.36 |
| | 0.00280 | 1.31 | 0.76 | 1.00 | 1.92 | 0.94 | 0.42 |
| 15 | 0.00045 | 0.87 | 1.17 | 1.02 | 1.37 | 0.96 | 0.37 |
| | 0.00090 | 0.95 | 0.83 | 0.80 | 1.07 | 1.03 | 0.41 |
| | 0.00160 | 1.04 | 0.76 | 0.79 | 1.06 | 0.90 | 0.40 |
| | 0.00280 | 1.16 | 0.69 | 0.80 | 1.13 | 0.94 | 0.43 |
| | 0.00480 | 1.36 | 1.01 | 1.37 | 1.90 | 1.00 | 0.37 |
| 25 | 0.00045 | 0.88 | 1.19 | 1.05 | 1.72 | 0.92 | 0.31 |
| | 0.00090 | 0.90 | 0.97 | 0.87 | 1.09 | 0.98 | 0.43 |
| | 0.00160 | 0.99 | 0.87 | 0.86 | 1.03 | 1.03 | 0.42 |
| | 0.00280 | 1.05 | 0.77 | 0.81 | 1.03 | 0.94 | 0.47 |
| | 0.00480 | 1.24 | 0.78 | 0.97 | 1.11 | 0.92 | 0.45 |
| 35 | 0.00090 | 0.89 | 1.02 | 0.91 | 1.11 | 0.98 | 0.43 |
| | 0.00160 | 0.95 | 0.93 | 0.88 | 1.02 | 1.02 | 0.43 |
| | 0.00280 | 0.99 | 0.82 | 0.81 | 1.02 | 1.03 | 0.52 |
| | 0.00480 | 1.13 | 0.73 | 0.82 | 1.02 | 0.99 | 0.44 |
| | 0.00800 | 1.29 | 0.91 | 1.21 | 1.28 | 0.85 | 0.40 |

Table 8.4: *Correction Factors for the Double Angle method selected $(x, Q^2)$ bins.*

| Double Angle method | | | | | | | |
|---|---|---|---|---|---|---|---|
| $Q^2$ (GeV$^2$) | $x$ | RadSmr | ExpSmr | TotSmr | SelAcc | RadCor | Purity |
| 50 | 0.00090 | 0.92 | 0.99 | 0.91 | 1.24 | 1.04 | 0.42 |
| | 0.00160 | 0.89 | 1.01 | 0.90 | 1.04 | 1.03 | 0.46 |
| | 0.00280 | 0.96 | 0.91 | 0.87 | 1.02 | 1.03 | 0.57 |
| | 0.00480 | 1.02 | 0.80 | 0.82 | 1.01 | 0.85 | 0.52 |
| | 0.00800 | 1.17 | 0.71 | 0.81 | 1.03 | 1.01 | 0.47 |
| 65 | 0.00090 | 0.81 | 0.84 | 0.68 | 1.93 | 1.07 | 0.26 |
| | 0.00160 | 0.91 | 0.95 | 0.86 | 1.04 | 0.94 | 0.46 |
| | 0.00280 | 0.92 | 0.99 | 0.91 | 1.00 | 1.13 | 0.56 |
| | 0.00480 | 0.95 | 0.87 | 0.82 | 1.01 | 1.02 | 0.54 |
| | 0.00800 | 1.11 | 0.69 | 0.76 | 1.01 | 1.05 | 0.46 |
| | 0.01500 | 1.18 | 0.79 | 0.93 | 1.12 | 1.03 | 0.48 |

Table 8.4: *Correction Factors for the Double Angle method selected* $(x, Q^2)$ *bins.*



| Double Angle method | | | | | | | |
|---|---|---|---|---|---|---|---|
| $Q^2$ (GeV$^2$) | $x$ | RadSmr | ExpSmr | TotSmr | SelAcc | RadCor | Purity |
| 125 | 0.00160 | 0.90 | 0.86 | 0.77 | 1.35 | 1.00 | 0.55 |
| | 0.00280 | 0.88 | 0.94 | 0.83 | 1.04 | 0.91 | 0.67 |
| | 0.00480 | 0.92 | 0.96 | 0.88 | 1.01 | 0.95 | 0.61 |
| | 0.00800 | 0.89 | 0.84 | 0.75 | 1.00 | 1.05 | 0.41 |
| | 0.01500 | 1.13 | 0.97 | 1.10 | 1.02 | 0.92 | 0.52 |
| | 0.03000 | 1.27 | 1.39 | 1.76 | 1.30 | 0.92 | 0.47 |
| 250 | 0.00480 | 0.89 | 1.00 | 0.89 | 1.10 | 1.24 | 0.65 |
| | 0.00800 | 0.84 | 1.02 | 0.86 | 1.03 | 0.83 | 0.69 |
| | 0.01500 | 0.93 | 0.90 | 0.84 | 1.02 | 0.95 | 0.70 |
| | 0.03000 | 1.06 | 0.65 | 0.69 | 1.00 | 1.02 | 0.51 |
| | 0.06000 | 1.23 | 0.98 | 1.21 | 1.11 | 0.87 | 0.49 |
| 500 | 0.00800 | 0.98 | 0.89 | 0.87 | 1.61 | 0.64 | 0.66 |
| | 0.01500 | 0.84 | 1.04 | 0.87 | 1.25 | 1.18 | 0.76 |
| | 0.03000 | 0.91 | 0.99 | 0.93 | 1.11 | 1.14 | 0.72 |
| | 0.06000 | 1.06 | 0.76 | 0.81 | 1.09 | 0.81 | 0.55 |
| | 0.12000 | 1.25 | 0.84 | 1.05 | 1.17 | 0.73 | 0.47 |
| 1000 | 0.01500 | 1.00 | 1.03 | 1.03 | 1.47 | 0.95 | 0.89 |
| | 0.03000 | 0.93 | 0.88 | 0.82 | 1.59 | 1.17 | 0.76 |
| | 0.06000 | 0.86 | 1.04 | 0.89 | 1.92 | 0.49 | 0.71 |
| | 0.12000 | 1.21 | 0.50 | 0.61 | 1.88 | 1.48 | 0.36 |
| 2000 | 0.12000 | 0.88 | 0.67 | 0.58 | 1.57 | 1.21 | 0.42 |

Table 8.4: *Correction Factors for the Double Angle method selected* $(x, Q^2)$ *bins.*

## 8.4 Measurement of the Cross Section

For each of the selected $(x, Q^2)$ bins, the number of estimated beam-gas and photoproduction background events (see section 5.10) is subtracted from the number of measured data events. The obtained number of background-subtracted (bkg.sub) data events is corrected for smearing and acceptance effects, using the TotSmr and SelAcc correction factors:

$$\text{TotSmr} \cdot \text{SelAcc} = \frac{dN(MC, true, no\ cuts)}{dN(MC, rec, cuts)} \tag{8.15}$$

In addition, the number of data events is corrected back to the Born cross section, using the radiative correction factor. Therefore, the total correction factor in each bin can be written as:

$$\text{TotCor} = \text{TotSmr} \cdot \text{SelAcc} \cdot \text{RadCor} = \frac{dN(Born, true, no\ cuts)}{dN(MC(Rad), rec, cuts)} \tag{8.16}$$

The corrected number of data events in each $(x, Q^2)$ bin divided by the total luminosity of the data yields the cross section $\sigma(x, Q^2)$ in that bin. Using appropriate bin widths, $\Delta x$ and $\Delta Q^2$, the differential cross section is then obtained.

The number of Monte Carlo events, data events before and after background subtraction, and after bin corrections, as well as the calculated cross section, in each $(x, Q^2)$ bin, are given in tables 8.5 and 8.6, for the Electron and Double Angle methods, respectively.



| Electron method | | | | | | | |
|---|---|---|---|---|---|---|---|
| $Q^2$ (GeV$^2$) | $x$ | MC | Data meas. | Bkgd estim. | Data bkg.sub | Data corr. | $\sigma$ (nb$^{-1}$) |
| 8.5 | 0.00022 | 3595 | 2097 | 254 | 1842 | 3569 | 6.51 |
| | 0.00045 | 1708 | 2936 | 173 | 2762 | 3988 | 7.31 |
| 12 | 0.00045 | 1686 | 2948 | 97 | 2850 | 2735 | 5.01 |
| | 0.00090 | 1145 | 3115 | 64 | 3050 | 2922 | 5.36 |
| | 0.00160 | 2226 | 1517 | 7 | 1509 | 1619 | 3.02 |
| | 0.00280 | 1973 | 1176 | 7 | 1168 | 1421 | 2.61 |
| 15 | 0.00045 | 2600 | 1741 | 105 | 1635 | 1999 | 3.66 |
| | 0.00090 | 3814 | 2903 | 39 | 2863 | 2356 | 4.32 |
| | 0.00160 | 2316 | 1926 | 7 | 1918 | 1548 | 2.84 |
| | 0.00280 | 2272 | 1514 | 15 | 1498 | 1255 | 2.30 |
| 25 | 0.00045 | 965 | 618 | 52 | 565 | 1001 | 1.84 |
| | 0.00090 | 2227 | 1611 | 28 | 1582 | 1386 | 2.54 |
| | 0.00160 | 1610 | 1317 | 0 | 1317 | 1154 | 2.12 |
| | 0.00280 | 1552 | 1275 | 7 | 1267 | 1072 | 1.97 |
| 35 | 0.00090 | 1454 | 1076 | 43 | 1032 | 993 | 1.82 |
| | 0.00160 | 1246 | 910 | 19 | 890 | 759 | 1.39 |
| | 0.00280 | 1159 | 1075 | 33 | 1041 | 994 | 1.82 |
| | 0.00480 | 901 | 746 | 0 | 746 | 671 | 1.23 |
| | 0.00800 | 690 | 524 | 0 | 524 | 445 | 0.82 |
| | 0.01500 | 584 | 441 | 0 | 441 | 588 | 1.08 |

Table 8.5: *Statistics and measured cross section for the Electron method*

| Electron method | | | | | | | |
|---|---|---|---|---|---|---|---|
| $Q^2$ (GeV$^2$) | $x$ | MC | Data meas. | Bkgd estim. | Data bkg.sub | Data corr. | $\sigma$ (nb$^{-1}$) |
| 50 | 0.00090 | 666 | 518 | 26 | 191 | 657 | 1.20 |
| | 0.00160 | 758 | 566 | 8 | 557 | 505 | 0.93 |
| | 0.00280 | 834 | 695 | 0 | 695 | 617 | 1.13 |
| | 0.00480 | 626 | 573 | 0 | 573 | 428 | 0.78 |
| | 0.00800 | 523 | 452 | 0 | 452 | 417 | 0.77 |
| | 0.01500 | 474 | 409 | 0 | 409 | 456 | 0.84 |
| 65 | 0.00160 | 543 | 389 | 14 | 374 | 305 | 0.56 |
| | 0.00280 | 603 | 482 | 4 | 477 | 428 | 0.79 |
| | 0.00480 | 470 | 408 | 0 | 408 | 350 | 0.64 |
| | 0.00800 | 460 | 357 | 0 | 357 | 285 | 0.52 |
| | 0.01500 | 524 | 399 | 0 | 399 | 332 | 0.61 |
| | 0.03000 | 330 | 209 | 0 | 209 | 210 | 0.39 |
| | 0.06000 | 135 | 101 | 0 | 101 | 221 | 0.41 |

Table 8.5: *Statistics and measured cross section for the Electron method*



| Double Angle method | | | | | | | |
|---|---|---|---|---|---|---|---|
| $Q^2$ (GeV$^2$) | $x$ | MC | Data meas. | Bkgd estim. | Data bkg.sub | Data corr. | $\sigma$ (nb$^{-1}$) |
| 8.5 | 0.00022 | 3532 | 2017 | 224 | 1792 | 3535 | 6.48 |
| | 0.00045 | 4181 | 2180 | 94 | 2385 | 3874 | 7.10 |
| 12 | 0.00045 | 4023 | 2113 | 81 | 2061 | 2301 | 4.22 |
| | 0.00090 | 4076 | 2370 | 31 | 2335 | 2274 | 4.17 |
| | 0.00160 | 2353 | 1436 | 0 | 1436 | 1484 | 2.72 |
| | 0.00280 | 1333 | 820 | 0 | 820 | 1476 | 2.71 |
| 15 | 0.00045 | 2353 | 1227 | 39 | 1187 | 1605 | 2.94 |
| | 0.00090 | 3585 | 2136 | 26 | 2109 | 1848 | 3.39 |
| | 0.00160 | 2474 | 1493 | 21 | 1471 | 1113 | 2.04 |
| | 0.00280 | 2274 | 1428 | 6 | 1421 | 1190 | 2.18 |
| | 0.00480 | 582 | 390 | 0 | 390 | 1011 | 1.86 |
| 25 | 0.00045 | 1027 | 641 | 38 | 602 | 1003 | 1.84 |
| | 0.00090 | 2094 | 1387 | 34 | 1352 | 1258 | 2.31 |
| | 0.00160 | 1548 | 1018 | 8 | 1009 | 921 | 1.69 |
| | 0.00280 | 1675 | 1162 | 8 | 1153 | 901 | 1.66 |
| | 0.00480 | 961 | 610 | 0 | 610 | 624 | 1.14 |
| 35 | 0.00090 | 1371 | 992 | 28 | 963 | 982 | 1.80 |
| | 0.00160 | 1152 | 792 | 36 | 755 | 697 | 1.28 |
| | 0.00280 | 1306 | 948 | 3 | 944 | 800 | 1.47 |
| | 0.00480 | 972 | 746 | 0 | 746 | 622 | 1.14 |
| | 0.00800 | 444 | 312 | 0 | 312 | 112 | 0.76 |

Table 8.6: *Statistics and measured cross section for the Double Angle method*

| Double Angle method | | | | | | | |
|---|---|---|---|---|---|---|---|
| $Q^2$ (GeV$^2$) | $x$ | MC | Data meas. | Bkgd estim. | Data bkg.sub | Data corr. | $\sigma$ (nb$^{-1}$) |
| 50 | 0.00090 | 758 | 564 | 36 | 527 | 619 | 1.14 |
| | 0.00160 | 710 | 541 | 7 | 533 | 515 | 0.95 |
| | 0.00280 | 805 | 623 | 8 | 614 | 566 | 1.04 |
| | 0.00480 | 669 | 588 | 0 | 588 | 111 | 0.75 |
| | 0.00800 | 554 | 419 | 0 | 419 | 365 | 0.67 |
| 65 | 0.00090 | 248 | 170 | 23 | 146 | 204 | 0.38 |
| | 0.00160 | 521 | 395 | 22 | 372 | 315 | 0.58 |
| | 0.00280 | 528 | 419 | 17 | 101 | 411 | 0.75 |
| | 0.00480 | 479 | 376 | 0 | 376 | 317 | 0.58 |
| | 0.00800 | 454 | 350 | 0 | 350 | 282 | 0.52 |
| | 0.01500 | 408 | 293 | 0 | 293 | 313 | 0.57 |

Table 8.6: *Statistics and measured cross section for the Double Angle method*



| Double Angle method | | | | | | | |
|---|---|---|---|---|---|---|---|
| $Q^2$ (GeV$^2$) | $x$ | MC | Data meas. | Bkgd estim. | Data bkg.sub | Data corr. | $\sigma$ (nb$^{-1}$) |
| 125 | 0.00160 | 323 | 261 | 29 | 231 | 211 | 0.11 |
| | 0.00280 | 620 | 532 | 58 | 473 | 371 | 0.68 |
| | 0.00480 | 531 | 460 | 15 | 444 | 373 | 0.69 |
| | 0.00800 | 522 | 459 | 20 | 438 | 318 | 0.61 |
| | 0.01500 | 501 | 361 | 0 | 361 | 371 | 0.68 |
| | 0.03000 | 199 | 150 | 0 | 150 | 311 | 0.58 |
| 250 | 0.00480 | 178 | 169 | 21 | 147 | 177 | 0.33 |
| | 0.00800 | 228 | 159 | 13 | 145 | 105 | 0.19 |
| | 0.01500 | 302 | 248 | 12 | 235 | 189 | 0.35 |
| | 0.03000 | 308 | 238 | 0 | 238 | 167 | 0.31 |
| | 0.06000 | 161 | 124 | 0 | 124 | 111 | 0.26 |
| 500 | 0.00800 | 62 | 49 | 12 | 36 | 32 | 0.06 |
| | 0.01500 | 101 | 79 | 0 | 79 | 101 | 0.19 |
| | 0.03000 | 105 | 98 | 0 | 98 | 115 | 0.21 |
| | 0.06000 | 108 | 95 | 0 | 95 | 67 | 0.12 |
| | 0.12000 | 62 | 34 | 0 | 34 | 30 | 0.06 |
| 1000 | 0.01500 | 35 | 30 | 0 | 30 | 13 | 0.08 |
| | 0.03000 | 33 | 18 | 0 | 18 | 27 | 0.05 |
| | 0.06000 | 28 | 24 | 0 | 24 | 20 | 0.01 |
| | 0.12000 | 28 | 27 | 0 | 27 | 15 | 0.08 |
| 2000 | 0.12000 | 12 | 11 | 0 | 11 | 12 | 0.02 |

Table 8.6: *Statistics and measured cross section for the Double Angle method*

## 8.5 From the Cross Section to $F_2$

The differential cross section in each $(x, Q^2)$ bin is multiplied by the kinematic factor $W(x, Q^2)$, given by eq.(8.1), in order to evaluate $F_2'(x, Q^2)$ (see eq. (8.3)). The factor $W$ is calculated in a bin using the mean values $x_{mean}$, $y_{mean}$ and $Q^2_{mean}$ in the bin.

In this way, the mean value of $F_2'$ is calculated in each bin. It has to be corrected to the $F_2'$ value at the point $(x_{center}, Q^2_{center})$. This is done by evaluating a *bin centering correction factor* in each bin, given by the ratio of the MRSD'_ parametrization of $F_2'$ at the exact point $(x_{center}, Q^2_{center})$ to the LEPTO calculated mean $F_2'$ in the bin. The dependence of the bin centering corrections on the input parametrization MRSD'_ is minimized by iterating the whole procedure of the $F_2'$ measurement, as explained later in this section.

After the bin centering corrections, the $F_2(x_{center}, Q^2_{center})$ value is extracted from the $F_2'(x_{center}, Q^2_{center})$ value using the $F_L$ corrections of the MRSD'_ parametrisation. The dependence of the $F_L$ corrections on the input parametrisation MRSD'_ is minimized by using $F_L$ corrections from different parametrisations as a systematic check (see section 8.6).

The statistical error on $F_2$ is calculated by considering the relevant statistical errors of the data, DIS NC Monte Carlo and PHP Monte Carlo samples that have been used in the $F_2$ measurement.

The $F_L$ correction factors and the central values of $F_2$ in each $(x, Q^2)$ bin, together with the statistical and systematic errors on $F_2$, are given in tables 8.9 and 8.10, for the Electron and Double Angle methods, respectively.



**• Iterative method**

The value of $F_2'$, obtained from the differential cross section, depends on the input structure function that has been used in the DIS NC Monte Carlo, through the bin correction factors.

In order to minimize the dependence on this input, we evaluate an *iteration factor* in each $(x, Q^2)$ bin, given by the ratio of the data to the Monte Carlo cross section in the bin. Both cross sections are evaluated after the event selection, using the reconstructed $x$ and $Q^2$ (relevant for the Monte Carlo).

$$R(x, Q^2) = \frac{\mathcal{L}_{MC}}{\mathcal{L}_{data}} \cdot \frac{dN(data, cuts)}{dN(MC, rec, cuts)} \tag{8.17}$$

This ratio should be equal to 1, if the Monte Carlo described the data perfectly. In practice, it varies from 0.6 to 1.5 in the selected bins (up to 50% deviations), before any iteration.

Subsequently, the iteration factors $R(x, Q^2)$ are applied as weights to the Monte Carlo events, but with the corresponding $x$ and $Q^2$ taken as the true generated values. The bin correction factors are reevaluated from the weighted Monte Carlo, and the $F_2'$ values obtained with the new correction factors are much less sensitive to the input structure function. The factors $R$ re-evaluated after the first iteration deviate from unity only by a few per cent.

**• Test of the $F_2$ extraction method**

The $F_2$ extraction procedure has been tested by using half of the Monte Carlo sample as real data. The extracted $F_2$ in this case reproduces the MRSD'_ structure function (within errors), that has been used as input to the DIS NC Monte Carlo.

## 8.6 Systematic Error on $F_2$

The stability of the $F_2$ measurement is checked against all important quantities used for the kinematic reconstruction, background reduction, and unfolding of the $F_2$ value from the measured number of events. In each case, a change is made to one quantity, the whole analysis is repeated, and the bin-by-bin deviations in $F_2$ from the nominal central values are recorded.

The systematic checks on the $F_2$ extraction are the following:

- *Electron finding and Photoproduction background*:

  The whole analysis is repeated using the electron finding algorithm referred to as EF2 in section 5.2. The two electron finders have different efficiencies and purities. In addition, they allow a different amount of PHP background events to enter the final data sample. Therefore, the use of a different electron finding algorithm is also a powerful systematic check of the level of PHP background.

- *Electron Energy scale*:

  For the Electron method, the electron energy scale in the Monte Carlo is changed by applying no additional resolution smearing (see section 6.3.5).

  For the Double Angle method, although the kinematic reconstruction does not depend on the electron energy scale, the selection criteria (cuts on $E$, $\delta$ and $y_{elec}$) do, and thus also does the final data sample. In order to check this, the analysis is repeated using corrected electron energies.



- *reliable electron finding and PHP background*:

  The cut on the electron energy is raised from 8 to 10 GeV for the Electron method, and from 5 to 10 GeV for the Double Angle method, and the analysis is repeated.

- *ISR, PHP and beam-gas backgrounds*:

  The lower $\delta$ cut controls the radiative corrections, the photoproduction background, and the $e/p$-gas background. In order to check the level of these types of background events, the lower cut on $\delta$ is varied from 35 GeV to 30 and 40 GeV, and the largest change is taken as the error in each bin.

- *Electron Angle*:

  The analysis is most sensitive to the electron position uncertainty in the region around the RCAL beam-pipe. In order to check this sensitivity, the box cut is varied from the standard square box of side 32 cm to a square box of side 34 cm for the Electron method, and to a rectangular box of vertical side 36 cm and horizontal side 28 cm for the Double Angle method. The different change of the box cut in the two methods is due to the need in the Electron method to remain within the region where the electron energy corrections have been measured.

- *Hadron Angle - only for the Double Angle method*:

  The $y_{JB}$ cut, which ensures a good measurement of the hadron angle $\gamma$, is varied from 0.01 to 0.02 and 0.06, and the largest deviation is taken in each bin.

- *Vertex*:

  A vertex cut of $-40 < Z_{vtx} < 20$ cm is applied (no vertex cut is applied in the nominal analysis).

- *Uncertainty in the Unfolding method*:

  The analysis is repeated without any iteration.

- *Uncertainty in the estimation of $F_L$*:

  $F_L$ is estimated using various PDF parametrisations ($MRSD'_0$, $MRSD'_-$, GRV(HO), CTEQ2), and the largest change is taken in each bin.

The systematic error on the $F_2$ value in each $(x, Q^2)$ bin is calculated by adding in quadrature the deviations, which are caused by the systematic checks, from the nominal $F_2$ value in the bin. However, not all systematic checks are included in the calculation of the final systematic error, depending on the reconstruction method.

In addition to the bin-by-bin systematic errors, there is an overall normalisation uncertainty of 3.5%, originating from the luminosity measurement (3.3%) and the first level trigger efficiency (1%). This normalisation uncertainty is not included in the calculation of the bin systematic errors, since it does not distort the shape of the distributions.



### 8.6.1 Electron method

The systematic error on the Electron method $F_2$ is calculated from the following systematic checks (SC):

SC1: different electron finder

SC2: electron energy scale

SC3: electron energy cut

SC4: $\delta$ cut

SC5: box cut

SC6: vertex cut

SC7: no iteration

SC8: $F_L$ estimation

It has to be noted here that by including both SC1 and SC3-4 we overestimate the systematic error on the PHP background, since using a different electron finder (EF2) also provides a different estimate of the PHP background events. However, the different efficiencies and purities of the two electron finders also affect the whole $F_2$ unfolding. Therefore, all three checks are included.

The systematic errors on radiative corrections, PHP and beam-gas backgrounds are also overestimated by including both SC2 and SC3-4, since the different electron energy scale effectively changes the cuts on $E$ and $\delta$. However, in the Electron method, the electron energy scale not only affects the event selection, but also is crucial for the kinematic reconstruction. Therefore, all three checks are included.

The percentage deviations from the nominal $F_2$ value in each bin, for each systematic check, are given in table 8.7.

### 8.6.2 Double Angle method

The systematic error on the Double Angle method $F_2$ is calculated from the following checks:

SC1: different electron finder

SC2: electron energy cut

SC3: $\delta$ cut

SC4: box cut

SC5: $y_{JB}$ cut

SC6: vertex cut

SC7: no iteration

SC8: $F_L$ estimation

Including both SC1 and SC2-3 leads to an overestimate of the PHP background, as discussed for the Electron method.

The electron energy scale check is covered by SC2 and SC3, since it affects the Double Angle analysis only through the electron energy and $\delta$ cuts.

The percentage deviations from the nominal $F_2$ value in each bin, for each systematic check, are given in table 8.8.



| Electron method | | | | | | | | | |
|---|---|---|---|---|---|---|---|---|---|
| $Q^2$ (GeV$^2$) | $x$ | SC1 | SC2 | SC3 | SC4 | SC5 | SC6 | SC7 | SC8 |
| 8 | 0.00022 | 0.40 | 2.50 | 1.05 | 19.57 | 0.00 | 0.26 | 10.87 | 0.99 |
| | 0.00045 | 1.61 | 0.66 | 0.00 | 0.07 | 3.51 | 4.46 | 6.07 | 0.22 |
| 12 | 0.00045 | 4.62 | 0.54 | 0.00 | 2.41 | 1.01 | 0.10 | 0.10 | 0.20 |
| | 0.00090 | 0.73 | 1.28 | 0.00 | 0.07 | 0.15 | 1.16 | 12.93 | 0.00 |
| | 0.00160 | 0.50 | 5.38 | 0.00 | 0.00 | 0.90 | 2.99 | 8.76 | 0.00 |
| | 0.00280 | 3.46 | 11.63 | 0.00 | 0.00 | 1.29 | 1.16 | 6.65 | 0.00 |
| 15 | 0.00045 | 6.65 | 0.75 | 0.99 | 5.28 | 0.19 | 1.61 | 3.35 | 0.25 |
| | 0.00090 | 0.70 | 3.72 | 0.00 | 0.21 | 0.35 | 1.12 | 6.94 | 0.14 |
| | 0.00160 | 0.32 | 4.73 | 0.00 | 0.00 | 1.89 | 0.87 | 15.69 | 0.00 |
| | 0.00280 | 0.12 | 1.56 | 0.00 | 0.00 | 3.23 | 2.03 | 5.50 | 0.00 |
| 25 | 0.00045 | 1.85 | 9.32 | 2.73 | 10.50 | 1.21 | 3.73 | 1.86 | 0.19 |
| | 0.00090 | 1.68 | 3.09 | 0.07 | 0.20 | 0.00 | 1.11 | 1.95 | 0.00 |
| | 0.00160 | 1.25 | 3.83 | 0.00 | 0.00 | 0.37 | 2.51 | 7.01 | 0.00 |
| | 0.00280 | 0.09 | 2.71 | 0.00 | 0.09 | 0.27 | 3.71 | 11.66 | 0.00 |
| 35 | 0.00090 | 1.23 | 2.99 | 1.10 | 2.14 | 0.45 | 2.08 | 1.30 | 0.19 |
| | 0.00160 | 0.90 | 1.31 | 0.08 | 0.08 | 0.16 | 1.96 | 3.35 | 0.00 |
| | 0.00280 | 2.22 | 6.51 | 0.00 | 0.08 | 0.00 | 1.13 | 11.03 | 0.00 |
| | 0.00480 | 0.32 | 8.52 | 0.00 | 0.11 | 0.32 | 3.36 | 3.05 | 0.00 |
| | 0.00800 | 1.86 | 17.61 | 0.00 | 0.00 | 0.27 | 1.38 | 1.06 | 0.00 |
| | 0.01500 | 3.23 | 29.89 | 0.00 | 0.16 | 0.00 | 3.23 | 3.72 | 0.00 |

Table 8.7: *Systematic errors, in percent, for the Electron method.*

| Electron method | | | | | | | | | |
|---|---|---|---|---|---|---|---|---|---|
| $Q^2$ (GeV$^2$) | $x$ | SC1 | SC2 | SC3 | SC4 | SC5 | SC6 | SC7 | SC8 |
| 50 | 0.00090 | 15.49 | 3.81 | 0.24 | 1.79 | 0.24 | 2.86 | 2.74 | 0.60 |
| | 0.00160 | 5.17 | 8.82 | 0.08 | 0.91 | 0.15 | 1.14 | 1.29 | 0.15 |
| | 0.00280 | 0.08 | 1.84 | 0.00 | 0.17 | 0.17 | 3.17 | 0.42 | 0.00 |
| | 0.00480 | 3.02 | 1.69 | 0.09 | 0.09 | 0.44 | 5.51 | 5.78 | 0.00 |
| | 0.00800 | 0.34 | 14.12 | 0.00 | 0.11 | 0.23 | 2.07 | 1.95 | 0.00 |
| | 0.01500 | 0.58 | 12.23 | 0.15 | 0.00 | 0.29 | 6.55 | 5.97 | 0.00 |
| 65 | 0.00160 | 6.67 | 3.49 | 1.29 | 0.68 | 0.00 | 1.82 | 2.96 | 0.23 |
| | 0.00280 | 4.70 | 2.84 | 0.08 | 0.81 | 0.00 | 4.86 | 0.73 | 0.00 |
| | 0.00480 | 0.37 | 16.16 | 0.00 | 0.09 | 0.37 | 1.39 | 5.36 | 0.00 |
| | 0.00800 | 0.51 | 1.16 | 0.00 | 0.00 | 0.00 | 5.02 | 0.00 | 0.00 |
| | 0.01500 | 0.77 | 15.41 | 0.00 | 0.00 | 0.15 | 4.93 | 2.77 | 0.00 |
| | 0.03000 | 2.90 | 41.52 | 0.00 | 0.00 | 0.00 | 6.25 | 12.95 | 0.00 |
| | 0.06000 | 3.39 | 19.28 | 0.00 | 0.00 | 0.00 | 0.64 | 2.97 | 0.00 |

Table 8.7: *Systematic errors, in percent, for the Electron method.*



| Double Angle method | | | | | | | | | |
|---|---|---|---|---|---|---|---|---|---|
| $Q^2$ (GeV$^2$) | $x$ | SC1 | SC2 | SC3 | SC1 | SC5 | SC6 | SC7 | SC8 |
| 8.5 | 0.00022 | 8.49 | 1.40 | 8.08 | 0.58 | 0.41 | 2.23 | 11.54 | 0.99 |
| | 0.00045 | 5.07 | 0.41 | 8.76 | 3.60 | 0.49 | 0.98 | 1.47 | 0.16 |
| 12 | 0.00045 | 2.63 | 1.87 | 5.60 | 1.53 | 0.25 | 0.42 | 2.29 | 0.17 |
| | 0.00090 | 2.77 | 0.10 | 3.91 | 3.19 | 1.03 | 1.23 | 1.03 | 0.00 |
| | 0.00160 | 0.21 | 0.00 | 2.06 | 0.60 | 5.11 | 1.57 | 0.21 | 0.00 |
| | 0.00280 | 0.30 | 0.00 | 0.45 | 1.61 | 14.80 | 3.11 | 5.23 | 0.00 |
| 15 | 0.00045 | 1.38 | 1.46 | 9.83 | 0.11 | 0.65 | 1.87 | 1.38 | 0.16 |
| | 0.00090 | 0.48 | 0.00 | 3.35 | 0.67 | 0.38 | 1.11 | 1.50 | 0.10 |
| | 0.00160 | 1.56 | 0.12 | 1.93 | 0.21 | 0.81 | 0.21 | 0.81 | 0.00 |
| | 0.00280 | 0.11 | 0.11 | 0.11 | 0.11 | 8.19 | 0.12 | 2.50 | 0.00 |
| | 0.00480 | 2.93 | 0.00 | 2.16 | 2.00 | 3.85 | 8.32 | 1.51 | 0.00 |
| 25 | 0.00045 | 1.67 | 1.61 | 7.51 | 0.39 | 0.00 | 1.80 | 3.92 | 0.19 |
| | 0.00090 | 6.67 | 1.09 | 1.11 | 0.78 | 0.00 | 1.55 | 6.52 | 0.00 |
| | 0.00160 | 0.79 | 0.00 | 1.77 | 0.10 | 0.10 | 2.17 | 1.28 | 0.00 |
| | 0.00280 | 0.93 | 0.00 | 0.46 | 0.35 | 2.21 | 1.05 | 2.11 | 0.00 |
| | 0.00180 | 3.17 | 0.00 | 0.63 | 0.32 | 3.01 | 2.06 | 9.19 | 0.00 |
| 35 | 0.00090 | 6.90 | 2.17 | 5.11 | 1.08 | 0.11 | 1.19 | 1.10 | 0.20 |
| | 0.00160 | 3.61 | 0.00 | 2.75 | 0.19 | 1.23 | 0.76 | 0.17 | 0.00 |
| | 0.00280 | 1.97 | 0.00 | 1.11 | 0.21 | 1.76 | 0.21 | 0.62 | 0.00 |
| | 0.00480 | 1.09 | 0.00 | 0.36 | 0.12 | 7.38 | 3.51 | 0.36 | 0.00 |
| | 0.00800 | 2.16 | 0.00 | 0.15 | 0.00 | 11.62 | 5.51 | 19.23 | 0.00 |

Table 8.8: *Systematic errors, in percent, for the Double Angle method.*

| Double Angle method | | | | | | | | | |
|---|---|---|---|---|---|---|---|---|---|
| $Q^2$ (GeV$^2$) | $x$ | SC1 | SC2 | SC3 | SC4 | SC5 | SC6 | SC7 | SC8 |
| 50 | 0.00090 | 13.83 | 13.06 | 8.83 | 0.19 | 0.00 | 2.24 | 0.77 | 0.51 |
| | 0.00160 | 3.26 | 0.78 | 1.79 | 0.23 | 0.16 | 0.85 | 2.17 | 0.08 |
| | 0.00280 | 2.56 | 0.09 | 1.14 | 0.19 | 0.19 | 0.95 | 0.38 | 0.00 |
| | 0.00180 | 2.88 | 0.10 | 0.77 | 0.19 | 0.87 | 2.02 | 7.12 | 0.00 |
| | 0.00800 | 1.10 | 0.00 | 0.28 | 0.00 | 9.12 | 2.21 | 1.66 | 0.00 |
| 65 | 0.00090 | 4.68 | 18.23 | 9.58 | 0.00 | 0.00 | 3.75 | 5.12 | 1.37 |
| | 0.00160 | 1.92 | 14.51 | 8.85 | 0.23 | 0.00 | 0.08 | 0.62 | 0.31 |
| | 0.00280 | 6.56 | 0.09 | 2.62 | 0.00 | 0.00 | 1.75 | 2.10 | 0.00 |
| | 0.00480 | 1.91 | 0.00 | 0.96 | 0.00 | 0.00 | 3.51 | 0.21 | 0.00 |
| | 0.00800 | 1.19 | 0.00 | 0.00 | 0.00 | 1.59 | 1.59 | 3.04 | 0.00 |
| | 0.01500 | 1.72 | 0.00 | 0.00 | 0.00 | 3.95 | 1.37 | 4.12 | 0.00 |

Table 8.8: *Systematic errors, in percent, for the Double Angle method.*



| Double Angle method | | | | | | | | | |
|---|---|---|---|---|---|---|---|---|---|
| $Q^2$ (GeV$^2$) | $x$ | SC1 | SC2 | SC3 | SC4 | SC5 | SC6 | SC7 | SC8 |
| 125 | 0.00160 | 11.45 | 6.32 | 8.01 | 1.19 | 0.00 | 0.77 | 9.76 | 1.62 |
| | 0.00280 | 5.38 | 9.33 | 6.92 | 0.29 | 0.00 | 3.27 | 0.19 | 0.29 |
| | 0.00480 | 0.91 | 0.30 | 0.20 | 0.00 | 0.10 | 1.01 | 1.52 | 0.10 |
| | 0.00800 | 1.19 | 0.00 | 0.70 | 0.00 | 0.20 | 1.09 | 6.66 | 0.00 |
| | 0.01500 | 1.23 | 0.15 | 0.77 | 0.00 | 0.62 | 2.62 | 3.09 | 0.00 |
| | 0.03000 | 2.72 | 0.00 | 0.00 | 0.00 | 3.68 | 3.27 | 15.12 | 0.00 |
| 250 | 0.00480 | 19.60 | 20.37 | 1.98 | 2.07 | 0.00 | 9.19 | 3.06 | 0.38 |
| | 0.00800 | 8.23 | 2.37 | 1.71 | 0.42 | 0.00 | 3.63 | 6.69 | 0.14 |
| | 0.01500 | 10.41 | 0.00 | 1.51 | 0.00 | 0.76 | 0.45 | 1.66 | 0.00 |
| | 0.03000 | 5.37 | 0.00 | 0.81 | 0.00 | 0.00 | 1.31 | 2.18 | 0.00 |
| | 0.06000 | 3.56 | 0.00 | 0.56 | 0.00 | 3.38 | 8.82 | 33.02 | 0.00 |
| 500 | 0.00800 | 75.30 | 27.60 | 7.88 | 3.55 | 0.00 | 5.65 | 7.10 | 0.39 |
| | 0.01500 | 30.44 | 0.00 | 3.91 | 0.47 | 0.00 | 0.32 | 2.68 | 0.16 |
| | 0.03000 | 2.77 | 0.00 | 2.19 | 2.77 | 0.00 | 3.65 | 3.80 | 0.15 |
| | 0.06000 | 2.11 | 0.19 | 0.58 | 0.96 | 1.80 | 1.15 | 23.99 | 0.00 |
| | 0.12000 | 4.23 | 0.00 | 0.00 | 1.63 | 1.89 | 1.30 | 99.99 | 0.00 |
| 1000 | 0.01500 | 58.82 | 12.79 | 1.01 | 2.21 | 0.00 | 0.00 | 9.52 | 0.37 |
| | 0.03000 | 21.80 | 0.00 | 0.00 | 2.10 | 7.97 | 18.24 | 13.21 | 0.00 |
| | 0.06000 | 9.05 | 0.00 | 3.18 | 11.15 | 0.00 | 3.71 | 1.16 | 0.00 |
| | 0.12000 | 2.88 | 0.00 | 0.00 | 0.18 | 0.00 | 3.21 | 71.53 | 0.00 |
| 2000 | 0.12000 | 1.97 | 0.00 | 0.00 | 0.88 | 0.00 | 0.00 | 31.11 | 0.00 |

Table 8.8: *Systematic errors, in percent, for the Double Angle method.*

## 8.7 Final Results on $F_2$

The final results on $F_2$, together with the statistical and systematic errors on $F_2$, in each $(x, Q^2)$ bin, are given in tables 8.9 and 8.10, for the Electron and Double Angle methods, respectively. Also listed are the $F_L$ correction factors in each bin.

The total error on $F_2$ in each $(x, Q^2)$ bin is obtained by adding the statistical and systematic errors in the bin in quadrature.

In figures 8.3 through 8.6 the $F_2$ values from the Electron and Double Angle methods, respectively, are plotted as functions of $x$ at fixed $Q^2$ bins. Various parametrizations for $F_2$ are also plotted for comparison. In figures 8.3 and 8.5 the Electron and Double Angle $F_2$ values are plotted together with the MRSD'_, MRSD'_0, MRSA and CTEQ2 curves (see sections 1.10.1 and 1.10.2). In figures 8.4 and 8.6 the Electron and Double Angle $F_2$ values are plotted together with the GRV(HO) (full curve) and the GRV94 (dashed curve) calculations. The latter takes in account the mass of the heavy quarks $c$ and $b$ (see section 1.10.3). The $F_2$ values for $Q^2 \leq 80$ GeV$^2$ from both the Electron and Double Angle methods are shown together in fig. 8.7.

Discussion of the $F_2$ results, as well as a detailed comparison of the $F_2$ values with the various PDFs, follow in chapter 10.



| Electron method | | | |
|---|---|---|---|
| $Q^2$ (GeV$^2$) | $x$ | $F_L$ corr. | $F_2 \pm$ stat $\pm$ sys |
| 8.5 | 0.00022 | 1.057 | 1.193 ± 0.013 ± 0.337 |
| | 0.00045 | 1.011 | 1.370 ± 0.033 ± 0.116 |
| 12 | 0.00045 | 1.022 | 1.199 ± 0.036 ± 0.080 |
| | 0.00090 | 1.004 | 1.316 ± 0.031 ± 0.180 |
| | 0.00160 | 1.001 | 0.947 ± 0.031 ± 0.102 |
| | 0.00280 | 1.000 | 0.806 ± 0.030 ± 0.121 |
| 15 | 0.00045 | 1.035 | 1.611 ± 0.051 ± 0.151 |
| | 0.00090 | 1.007 | 1.372 ± 0.034 ± 0.110 |
| | 0.00160 | 1.002 | 1.205 ± 0.037 ± 0.199 |
| | 0.00280 | 1.001 | 0.815 ± 0.028 ± 0.058 |
| 25 | 0.00045 | 1.115 | 1.571 ± 0.083 ± 0.217 |
| | 0.00090 | 1.020 | 1.113 ± 0.017 ± 0.062 |
| | 0.00160 | 1.005 | 1.302 ± 0.048 ± 0.110 |
| | 0.00280 | 1.001 | 1.076 ± 0.040 ± 0.135 |
| 35 | 0.00090 | 1.041 | 1.511 ± 0.063 ± 0.073 |
| | 0.00160 | 1.010 | 1.226 ± 0.054 ± 0.051 |
| | 0.00280 | 1.003 | 1.261 ± 0.054 ± 0.165 |
| | 0.00180 | 1.001 | 0.951 ± 0.047 ± 0.092 |
| | 0.00800 | 1.000 | 0.757 ± 0.011 ± 0.139 |
| | 0.01500 | 1.000 | 0.621 ± 0.039 ± 0.189 |

Table 8.9: *$F_L$ corrections and final $F_2$ values, for the Electron method.*

| Electron method | | | |
|---|---|---|---|
| $Q^2$ (GeV$^2$) | $x$ | $F_L$ corr. | $F_2 \pm$ stat $\pm$ sys |
| 50 | 0.00090 | 1.096 | 1.678 ± 0.100 ± 0.278 |
| | 0.00160 | 1.022 | 1.315 ± 0.073 ± 0.137 |
| | 0.00280 | 1.006 | 1.200 ± 0.062 ± 0.044 |
| | 0.00480 | 1.002 | 1.127 ± 0.065 ± 0.098 |
| | 0.00800 | 1.001 | 0.870 ± 0.056 ± 0.125 |
| | 0.01500 | 1.000 | 0.686 ± 0.046 ± 0.101 |
| 65 | 0.00160 | 1.039 | 1.323 ± 0.089 ± 0.111 |
| | 0.00280 | 1.010 | 1.234 ± 0.076 ± 0.091 |
| | 0.00480 | 1.003 | 1.083 ± 0.073 ± 0.185 |
| | 0.00800 | 1.001 | 0.780 ± 0.055 ± 0.040 |
| | 0.01500 | 1.000 | 0.649 ± 0.043 ± 0.107 |
| | 0.03000 | 1.000 | 0.448 ± 0.040 ± 0.197 |
| | 0.06000 | 1.000 | 0.471 ± 0.062 ± 0.093 |

Table 8.9: *$F_L$ corrections and final $F_2$ values, for the Electron method.*



| Double Angle method | | | |
|---|---|---|---|
| $Q^2$ (GeV$^2$) | $x$ | $F_L$ corr. | $F_2 \pm$ stat $\pm$ sys |
| 8.5 | 0.00022 | 1.057 | 1.322 ± 0.038 ± 0.221 |
| | 0.00045 | 1.011 | 1.191 ± 0.031 ± 0.130 |
| 12 | 0.00045 | 1.022 | 1.179 ± 0.032 ± 0.083 |
| | 0.00090 | 1.004 | 0.973 ± 0.025 ± 0.059 |
| | 0.00160 | 1.001 | 0.827 ± 0.028 ± 0.050 |
| | 0.00280 | 1.000 | 0.669 ± 0.030 ± 0.108 |
| 15 | 0.00045 | 1.035 | 1.231 ± 0.011 ± 0.127 |
| | 0.00090 | 1.007 | 1.011 ± 0.029 ± 0.061 |
| | 0.00160 | 1.002 | 0.831 ± 0.027 ± 0.023 |
| | 0.00280 | 1.001 | 0.720 ± 0.024 ± 0.062 |
| | 0.00480 | 1.000 | 0.649 ± 0.042 ± 0.066 |
| 25 | 0.00045 | 1.115 | 1.557 ± 0.080 ± 0.110 |
| | 0.00090 | 1.020 | 1.289 ± 0.045 ± 0.131 |
| | 0.00160 | 1.005 | 1.015 ± 0.011 ± 0.032 |
| | 0.00280 | 1.001 | 0.861 ± 0.033 ± 0.031 |
| | 0.00480 | 1.000 | 0.631 ± 0.033 ± 0.066 |
| 35 | 0.00090 | 1.041 | 1.478 ± 0.062 ± 0.149 |
| | 0.00160 | 1.010 | 1.053 ± 0.019 ± 0.050 |
| | 0.00280 | 1.003 | 0.966 ± 0.011 ± 0.029 |
| | 0.00480 | 1.001 | 0.827 ± 0.010 ± 0.068 |
| | 0.00800 | 1.000 | 0.650 ± 0.018 ± 0.162 |

Table 8.10: *$F_L$ corrections and final $F_2$ values, for the Double Angle method.*

| Double Angle method | | | |
|---|---|---|---|
| $Q^2$ (GeV$^2$) | $x$ | $F_L$ corr. | $F_2 \pm$ stat $\pm$ sys |
| 50 | 0.00090 | 1.096 | 1.562 ± 0.089 ± 0.330 |
| | 0.00160 | 1.022 | 1.288 ± 0.071 ± 0.058 |
| | 0.00280 | 1.006 | 1.053 ± 0.056 ± 0.032 |
| | 0.00480 | 1.002 | 1.040 ± 0.059 ± 0.084 |
| | 0.00800 | 1.001 | 0.721 ± 0.047 ± 0.069 |
| 65 | 0.00090 | 1.183 | 1.388 ± 0.141 ± 0.307 |
| | 0.00160 | 1.039 | 1.300 ± 0.088 ± 0.223 |
| | 0.00280 | 1.010 | 1.111 ± 0.076 ± 0.087 |
| | 0.00480 | 1.003 | 0.911 ± 0.065 ± 0.039 |
| | 0.00800 | 1.001 | 0.756 ± 0.051 ± 0.030 |
| | 0.01500 | 1.000 | 0.582 ± 0.045 ± 0.036 |

Table 8.10: *$F_L$ corrections and final $F_2$ values, for the Double Angle method.*



| Double Angle method | | | |
|---|---|---|---|
| $Q^2$ (GeV$^2$) | $x$ | $F_L$ corr. | $F_2 \pm$ stat $\pm$ sys |
| 125 | 0.00160 | 1.195 | 1.355 ± 0.117 ± 0.248 |
| | 0.00280 | 1.043 | 1.066 ± 0.065 ± 0.141 |
| | 0.00480 | 1.011 | 0.993 ± 0.064 ± 0.044 |
| | 0.00800 | 1.003 | 0.891 ± 0.058 ± 0.062 |
| | 0.01500 | 1.001 | 0.606 ± 0.042 ± 0.026 |
| | 0.03000 | 1.000 | 0.571 ± 0.062 ± 0.092 |
| 250 | 0.00480 | 1.058 | 1.306 ± 0.115 ± 0.397 |
| | 0.00800 | 1.015 | 0.717 ± 0.076 ± 0.089 |
| | 0.01500 | 1.003 | 0.661 ± 0.057 ± 0.071 |
| | 0.03000 | 1.001 | 0.596 ± 0.051 ± 0.036 |
| | 0.06000 | 1.000 | 0.533 ± 0.061 ± 0.181 |
| 500 | 0.00800 | 1.082 | 0.761 ± 0.158 ± 0.618 |
| | 0.01500 | 1.015 | 0.631 ± 0.095 ± 0.195 |
| | 0.03000 | 1.002 | 0.685 ± 0.096 ± 0.047 |
| | 0.06000 | 1.000 | 0.521 ± 0.073 ± 0.128 |
| | 0.12000 | 1.000 | 0.307 ± 0.066 ± 0.312 |
| 1000 | 0.01500 | 1.081 | 1.071 ± 0.266 ± 0.655 |
| | 0.03000 | 1.011 | 0.477 ± 0.110 ± 0.155 |
| | 0.06000 | 1.002 | 0.431 ± 0.120 ± 0.076 |
| | 0.12000 | 1.000 | 0.555 ± 0.150 ± 0.398 |
| 2000 | 0.12000 | 1.001 | 0.456 ± 0.190 ± 0.112 |

Table 8.10: *$F_L$ corrections and final $F_2$ values, for the Double Angle method.*

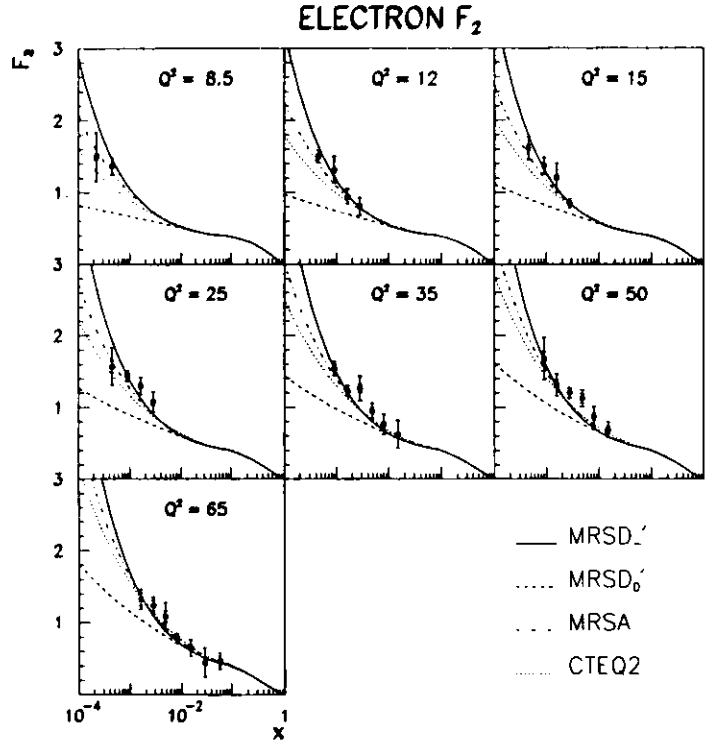


Figure 8.3: *Final $F_2$ values from the Electron method plotted as functions of $x$ at fixed $Q^2$. The inner error bars show the statistical errors. The outer error bars show the total errors. The curves represent the $F_2$ parametrizations from MRSD_, MRSD$_0$, MRSA and CTEQ2.*



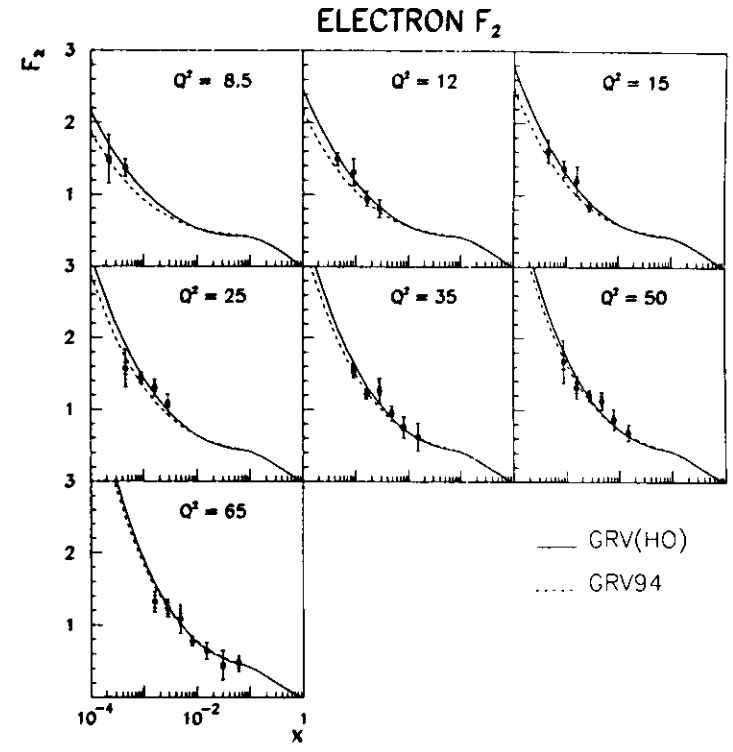


Figure 8.4: *Final $F_2$ values from the Electron method plotted as functions of $x$ at fixed $Q^2$. The full curve represents the GRV(HO) parametrization. The dashed curve represents the GRV94 parametrization (in NLO), which takes in account the finite mass of the c and b quarks.*

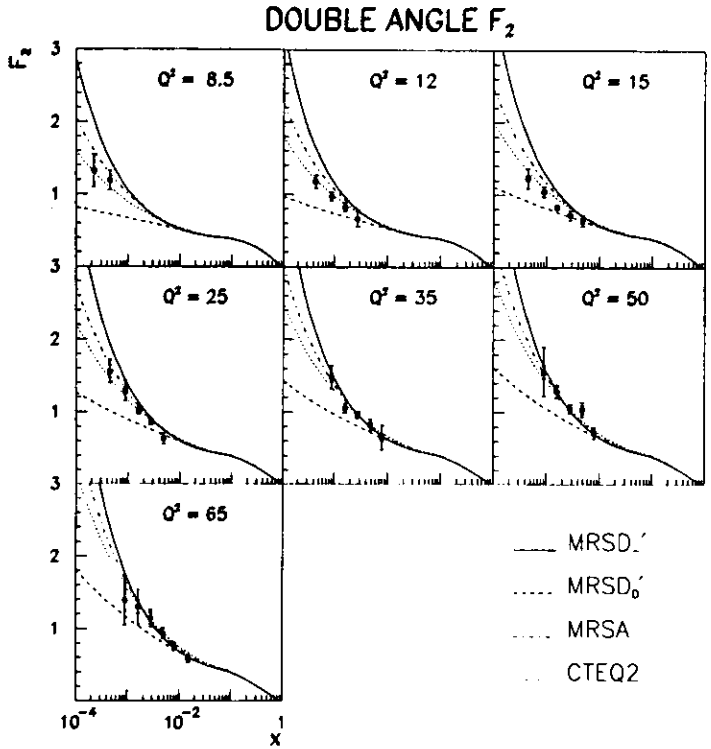


Figure 8.5: *Final $F_2$ values from the Double Angle method plotted as functions of $x$ at fixed $Q^2$. The inner error bars show the statistical errors. The outer error bars show the total errors. The curves represent the $F_2$ parametrizations from MRSD_, MRSD$_0$, MRSA and CTEQ2.*



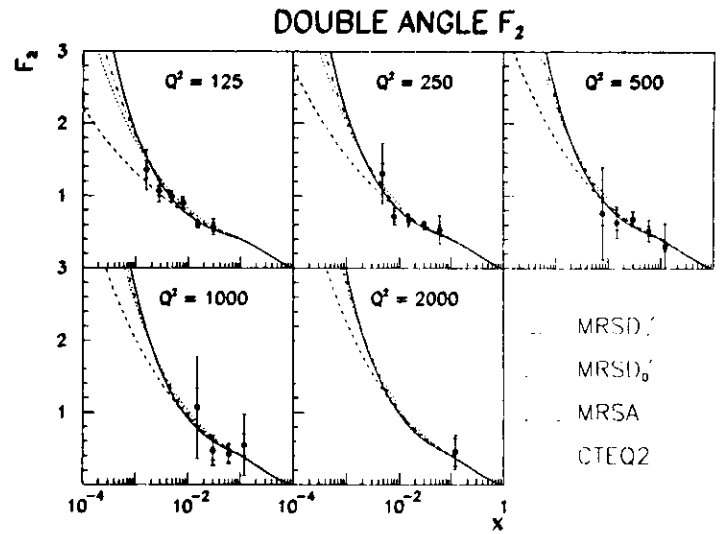


Figure 8.5: *Final $F_2$ values from the Double Angle method plotted as functions of $x$ at fixed $Q^2$. The inner error bars show the statistical errors. The outer error bars show the total errors. The curves represent the $F_2$ parametrizations from MRSD_, MRSD$_0$, MRSA and CTEQ2.*

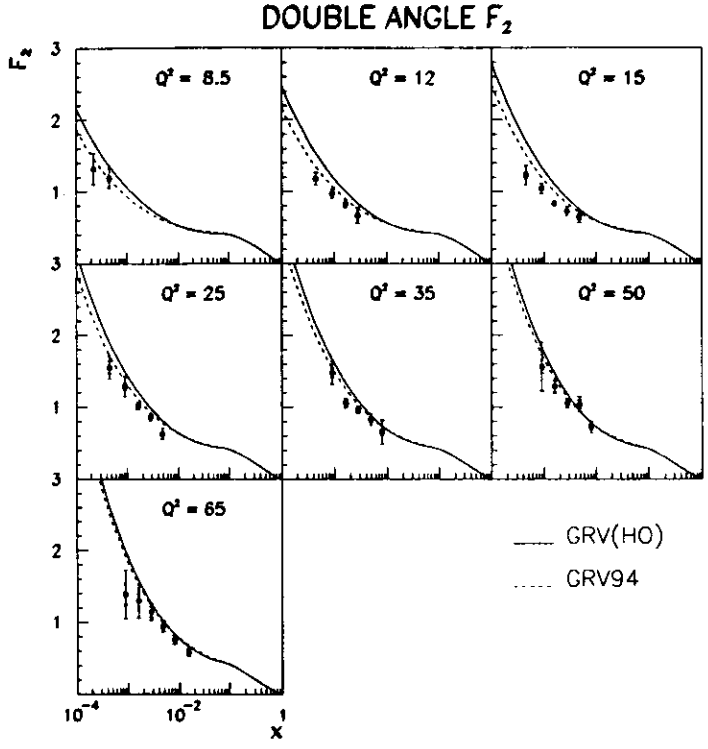


Figure 8.6: *Final $F_2$ values from the Double Angle method plotted as functions of $x$ at fixed $Q^2$. The full curve represents the GRV(HO) parametrization. The dashed curve represents the GRV94 parametrization (in NLO), which takes in account the finite mass of the c and b quarks.*



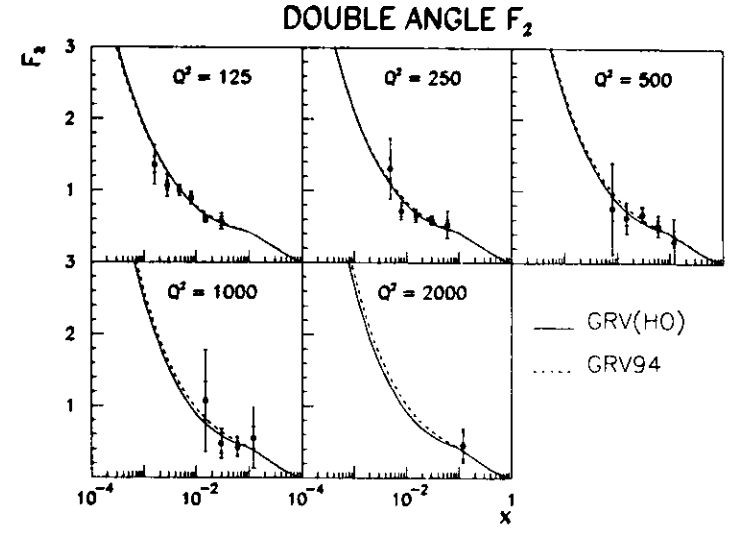


Figure 8.6: *Final $F_2$ values from the Double Angle method plotted as functions of $x$ at fixed $Q^2$. The full curve represents the GRV(HO) parametrization. The dashed curve represents the GRV94 parametrization (in NLO), which takes in account the finite mass of the c and b quarks.*

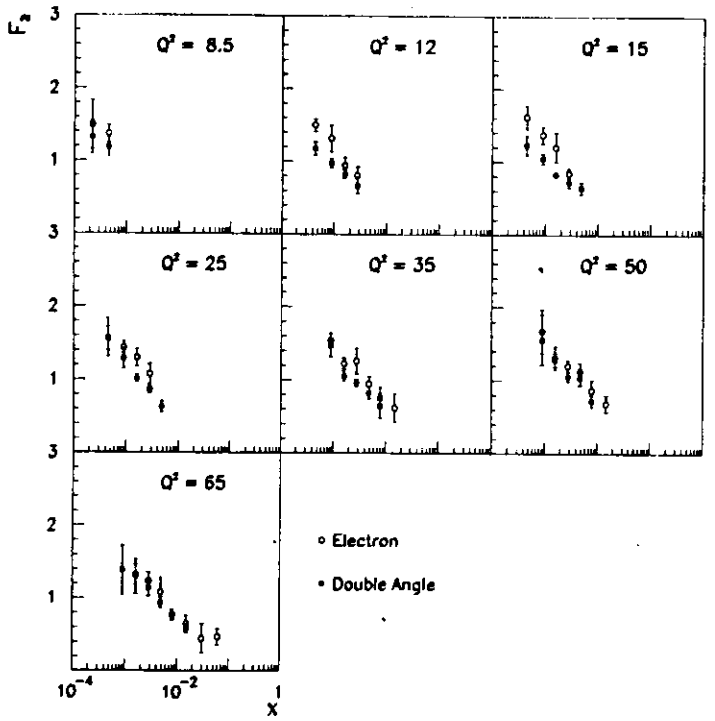


Figure 8.7: *$F_2$ values from the Electron method (open circles) and Double Angle (solid circles) methods plotted as functions of $x$ at fixed $Q^2$. The error bars show the total errors.*



# Chapter 9

# The Gluon density of the Proton

## 9.1 $F_2$ scaling violations and the Gluon

The scaling of the proton structure functions (i.e. independence of $Q^2$) is valid only in the naive Quark-Parton Model. In QCD, the quark densities in the proton, and thus also the proton structure functions, evolve with $Q^2$, as a result of the interactions between quarks and gluons: gluon bremsstrahlung from quarks, and quark pair production from gluons. This has been discussed in section 1.5 and is shown in fig. 9.1, where the $F_2$ structure function is plotted as a function of $Q^2$, at various, fixed values of $x$.

The $Q^2$ evolution of the quark densities, $q_f(x,Q^2)$, is determined by the GLAP evolution equation (1.20):

$$\frac{dq_f(x,Q^2)}{d\ln Q^2} = \frac{\alpha_s(Q^2)}{2\pi}\left[\int_x^1 \frac{dy}{y} P_{qq}(\frac{x}{y}) q_f(y,Q^2) + \int_x^1 \frac{dy}{y} P_{qg}(\frac{x}{y}) g(y,Q^2)\right] \quad (9.1)$$

For single photon exchange, the structure function $F_2$ is given by:

$$F_2(x,Q^2) = \sum_f e_f^2 \{x q_f(x,Q^2) + x q_f(x,Q^2)\}, \quad (9.2)$$

as can be deduced from equations (1.30) and (1.32).

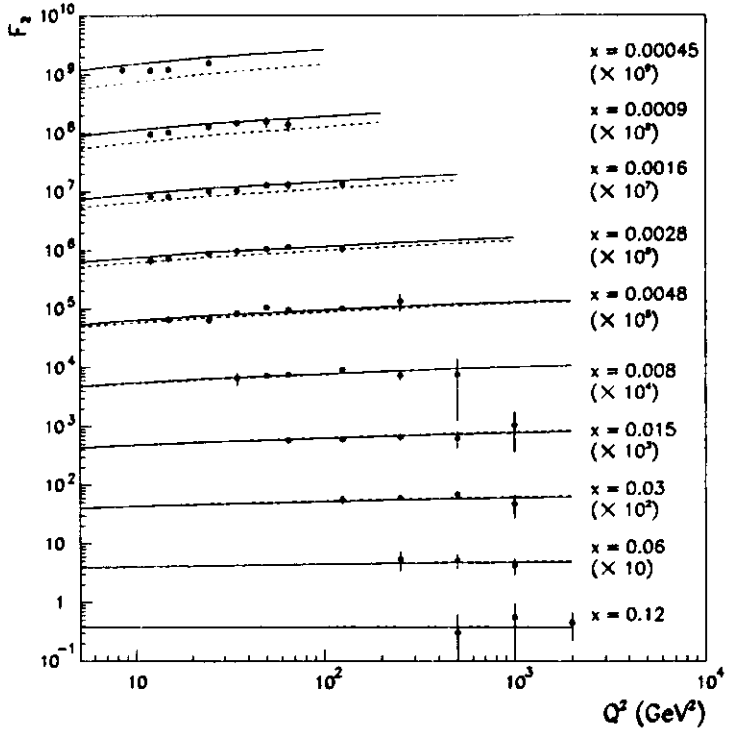


Figure 9.1: *$F_2$ values, extracted with the Double Angle method, plotted as function of $Q^2$ at fixed $x$. The error bars represent the statistical and systematic errors added in quadrature. Also shown are the $MRSD'_-$ (full curve) and $MRSD'_0$ (dashed curve) parametrizations.*



Thus, the $Q^2$ evolution of $F_2$, in Leading Order (LO) QCD, is given by:

$$\frac{dF_2(x,Q^2)}{d\ln Q^2} = \frac{\alpha_s(Q^2)}{2\pi}\left[\int_x^1 \frac{dy}{y}(\frac{x}{y})P_{qq}(\frac{x}{y})F_2(y,Q^2) + 2\sum_f \epsilon_f^2 \int_x^1 \frac{dy}{y}(\frac{x}{y})P_{qg}(\frac{x}{y})\,yg(y,Q^2)\right] \quad (9.3)$$

where the splitting functions $P_{qq}(x/y)$ and $P_{qg}(x/y)$ give the probability that a quark with momentum fraction $x$ originated from a quark or gluon with momentum fraction $y$, where $x < y < 1$ (see section 1.5).

In the above equations, $g(x,Q^2)$ is the *gluon density* of the proton, defined such that $g(x,Q^2)dx$ gives the number of gluons in the proton with a momentum fraction between $x$ and $x + dx$. Then, the *gluon momentum density* is given by:

$$G(x,Q^2) \equiv xg(x,Q^2). \quad (9.1)$$

At low values of $x$, $x < 10^{-2}$, the quark pair production from gluons dominates over the gluon bremsstrahlung from quarks in producing the $Q^2$-evolution of the quark densities[50] (i.e. the second term on the right-hand side of equations (9.1) and (9.3) becomes dominant). This fact can be exploited to extract the gluon density of the proton from the measured slope $dF_2(x,Q^2)/d\ln Q^2$ of the proton structure function $F_2$.

Two approximate methods, one proposed by Prytz and another by Ellis, Kunszt and Levin (EKL), are used here in order to determine the gluon distribution at $Q^2 = 20$ GeV$^2$. A global QCD fit to $F_2$, using the full Next to Leading Order (NLO) GLAP evolution equations, has also been perfomed.[51] The result of the fit agrees well with the results of the two approximate methods.

## 9.2 Prytz method

The Prytz method, proposed in LO [52] and NLO, [53] completely ignores the quark contribution to the $F_2$ scaling violations. Thus, the $Q^2$-evolution equation of $F_2$, in LO, takes the form:

$$\frac{dF_2(x,Q^2)}{d\ln Q^2} \approx \frac{\alpha_s(Q^2)}{2\pi} 2\sum_f e_f^2 \int_x^1 \frac{dy}{y}(\frac{x}{y})P_{qg}(\frac{x}{y})G(y,Q^2) \qquad (9.5)$$

The splitting function $P_{qg}$ is given in lowest order by eq. (1.24):

$$P_{qg}(z) = \frac{1}{2}(z^2 + (1-z)^2), \qquad (9.6)$$

where $z = x/y$.

Then

$$P_{qg}(z) = P_{qg}(1-z), \qquad (9.7)$$

which means that $P_{qg}(z)$ is symmetric around $z = 1/2$.

Substituting $P_{qg}(z)$ into eq. (9.5), converting the integral over $y$ to an integral over $z$, making a variable substitution from $z$ to $1-z$, and summing over four flavors ($n_f = 4$), eq. (9.5) becomes:

$$\frac{dF_2(x,Q^2)}{d\ln Q^2} \approx \frac{5\alpha_s(Q^2)}{9\pi} \int_0^{1-x} G(\frac{x}{1-z},Q^2)(z^2+(1-z)^2)dz. \qquad (9.8)$$

The integral in (9.8) is performed approximately. For this purpose, the gluon momentum density is expanded as a Taylor series around $z = 1/2$:

$$G(\frac{x}{1-z}) \approx G(z=\frac{1}{2}) + (z-\frac{1}{2})G'(z=\frac{1}{2}) + (z-\frac{1}{2})^2 G''(z=\frac{1}{2}) + \ldots \qquad (9.9)$$

Inserting this expression into eq. (9.8) and approximating the upper limit of the integral to 1 (justified for small $x$), the second term of the integral vanishes due to the symmetry of $P_{qg}(z)$ around $z = 1/2$. The third term gives only a small contribution compared to the first one, and is neglected. Thus, eq. (9.8) finally becomes:

$$\frac{dF_2(x,Q^2)}{d\ln Q^2} \approx \frac{10\alpha_s(Q^2)}{27\pi} G(2x,Q^2). \qquad (9.10)$$



Eq. (9.10) relates the gluon momentum density of the proton at a given point $x$ to the logarithmic slope of $F_2$ at $x/2$.

Neglecting the quark contribution to $dF_2/d\ln Q^2$ leads to an overestimate of the extracted gluon density. However, at $Q^2 = 20$ GeV$^2$ and for $x < 10^{-2}$ the quark contribution amounts to only 5-8%. [53] On the other hand, the $\alpha_s^2$ correction to the LO result reaches 35% in this kinematic region (quark contribution neglected). [53] Including the NLO correction, the gluon momentum distribution for four flavors in the $\overline{\rm MS}$ scheme takes the form:

$$G(2x,Q^2) = \frac{4\pi/\alpha_s}{10/27 + 7.96\alpha_s/4\pi}\frac{dF_2(x,Q^2)}{d\ln Q^2} - \frac{\alpha_s/4\pi}{2/3 + 3.58\alpha_s/4\pi}N(x,Q^2) \qquad (9.11)$$

The correction function $N(x/2,Q^2)$ has been estimated [53] using the $MRSD'_-$ and $MRSD'_0$ parametrizations. At $Q^2 = 20$ GeV$^2$ and in the $x$ range used in this analysis, $9\cdot10^{-4} < x < 0.48\cdot10^{-2}$ (see section 9.4), the two parametrizations give almost the same results for $N$.

The Prytz formula (9.11) has been compared [53] to the exact NLO result ($F_2$ term included) of the $MRSD'_-$ and $MRSD'_0$ calculations. At $Q^2 = 20$ GeV$^2$ eq. (9.11) was found to be accurate at the level of 10%.

## 9.3 EKL method

The EKL method [54] is based on a solution of the GLAP evolution equations in moment space. It is implemented is LO, NLO and NNL

A functional form of $x^{-\omega_0}$ is assumed for both the proton structure function $F_2$ and the gluon momentum density of the proton $G$. Then the scaling violation of $F_2$ takes the form:

$$\frac{d\Sigma(x,Q^2)}{d\ln Q^2} = P^{FF}(\omega_0)\Sigma(x,Q^2) + P^{FG}(\omega_0)g(x,Q^2), \tag{9.12}$$

with

$$\Sigma(x,Q^2) = \frac{1}{< e_q^2 >}\frac{F_2(x,Q^2)}{x}, \tag{9.13}$$

and

$$< e_q^2 >= \frac{4n_{f_u} + n_{f_d}}{9n_f}, \tag{9.14}$$

where $n_{f_u}$ and $n_{f_d}$ denote the number of quarks with electric charges $\frac{2}{3}$ and $-\frac{1}{3}$, respectively. For four quark flavours the mean square quark charge $< e_q^2 >$ is equal to 5/18. $P^{FF}$ and $P^{FG}$ are functions of $\alpha_s$. In the $\overline{\rm MS}$ scheme they are given by:

$$P^{FF}(\omega_0) = \alpha_s p_0^{FF} + \alpha_s^2 p_1^{FF} + \alpha_s^3 p_2^{FF} + \mathcal{O}(\alpha_s^4) \tag{9.15}$$

$$P^{FG}(\omega_0) = \alpha_s p_0^{FG} + \alpha_s^2 p_1^{FG} + \alpha_s^3 p_2^{FG} + \mathcal{O}(\alpha_s^4) \tag{9.16}$$

The coefficients $p_i^{FF}$ and $p_i^{FG}$ depend on the parameter $\omega_0$, whose value has to be extracted from the data.

The gluon momentum density of the proton can be deduced from eq. (9.12). For four flavours, it takes the form:

$$G(x,Q^2) \equiv xg(x,Q^2) = \frac{18/5}{P^{FG}(\omega_0)}\left[\frac{dF_2(x,Q^2)}{d\ln Q^2} - P^{FF}(\omega_0)F_2(x,Q^2)\right] \tag{9.17}$$

As it can be seen from equations (9.12) and (9.17), the quark contribution to the $F_2$ scaling violations is included in the EKL method, in contrast to the Prytz method.



It also has to be noted that eq. (9.17) relates the gluon momentum density of the proton at a given point $x$ with the logarithmic slope of $F_2$ at the same value $x$, in contrast to the Prytz method.

## 9.4 Extraction of the Gluon density

We choose to extract the gluon density of the proton at $Q^2 = 20$ GeV$^2$. In order to determine the $F_2$ slope, the four $x$ bins ($x = 0.0009, 0.0016, 0.0028, 0.0018$) that have data both below and above $Q^2 = 20$ GeV$^2$ are used. Since the Electron $F_2$ values are only extracted in a limited kinematic region, the Double Angle $F_2$ values are used here.

In each of the selected $x$ bins, the structure function $F_2$ is fit with a linear function of the form:

$$F_2(x,Q^2) = a(x) + b(x)\ln(Q^2/20\ \text{GeV}^2). \tag{9.18}$$

The fit parameters $a$ and $b$ represent the $F_2$ value at $Q^2 = 20$ GeV$^2$ and the logarithmic slope of $F_2$, respectively:

$$a(x) = F_2(x, Q^2 = 20\ \text{GeV}^2) \tag{9.19}$$

$$b(x) = \frac{dF_2(x,Q^2)}{d\ln Q^2} \tag{9.20}$$

In order to obtain the central values of $a$ and $b$ and their statistical errors, the central values of $F_2$ with only their statistical errors are fit. In order to obtain the systematic errors of $a$ and $b$, each set of the systematically shifted $F_2$ values (see section 8.6), with their statistical errors, is fit separately. In this way, 8 different sets of the fit parameters are obtained. The positive (negative) deviations from the central values of $a$ and $b$ are added in quadrature

to determine the positive (negative) systematic error of the fit parameters. The linear fits of the $F_2$ values in the four $x$ bins are shown in fig. 9.2. The values of the fit parameters and their statistical and systematic errors are listed in table 9.1.

| $x$ | $F_2(x, Q^2 = 20\,\mathrm{GeV}^2)$ | $dF_2(x)/d\ln Q^2$ |
|---|---|---|
| 0.0009 | $1.18 \pm 0.02^{+0.06}_{-0.06}$ | $0.41 \pm 0.04^{+0.03}_{-0.07}$ |
| 0.0016 | $0.94 \pm 0.02^{+0.03}_{-0.02}$ | $0.27 \pm 0.03^{+0.04}_{-0.04}$ |
| 0.0028 | $0.80 \pm 0.01^{+0.03}_{-0.03}$ | $0.23 \pm 0.02^{+0.02}_{-0.06}$ |
| 0.0048 | $0.67 \pm 0.02^{+0.06}_{-0.04}$ | $0.22 \pm 0.03^{+0.03}_{-0.05}$ |

Table 9.1: *Central values, statistical and systematic errors of $F_2(x, Q^2 = 20\,\mathrm{GeV}^2)$ and $dF_2(x)/d\ln Q^2$, obtained from linear fits to the Double Angle $F_2$ values, for the four selected $x$ bins, according to eq. (9.18).*

Substituting the values of $F_2(x, Q^2 = 20\,\mathrm{GeV}^2)$ and/or $dF_2(x)/d\ln Q^2$, as obtained from the fit, into equations (9.10), (9.11) and (9.17), the gluon momentum density of the proton is extracted at $Q^2 = 20\,\mathrm{GeV}^2$ and at the four selected $x$ values. For the Prytz method, eq. (9.10) provides the LO result, while eq. (9.11) gives the gluon momentum density in NLO. For the EKL method, the LO and NLO results are obtained retaining the terms up to $\mathcal{O}(\alpha_s)$ and $\mathcal{O}(\alpha_s^2)$ in equations (9.15) and (9.16), respectively. For both methods the value of $\alpha_s(Q^2 = 20\,\mathrm{GeV}^2) = 0.203 \pm 0.010$ is used. For the EKL method, the parameter $\omega_0$ is set to $\omega_0 = 0.4$, which agrees with the result of the global fit to the GLAP equations, as mentioned in section 9.1.

The extracted gluon momentum density of the proton, at $Q^2 = 20\,\mathrm{GeV}^2$,



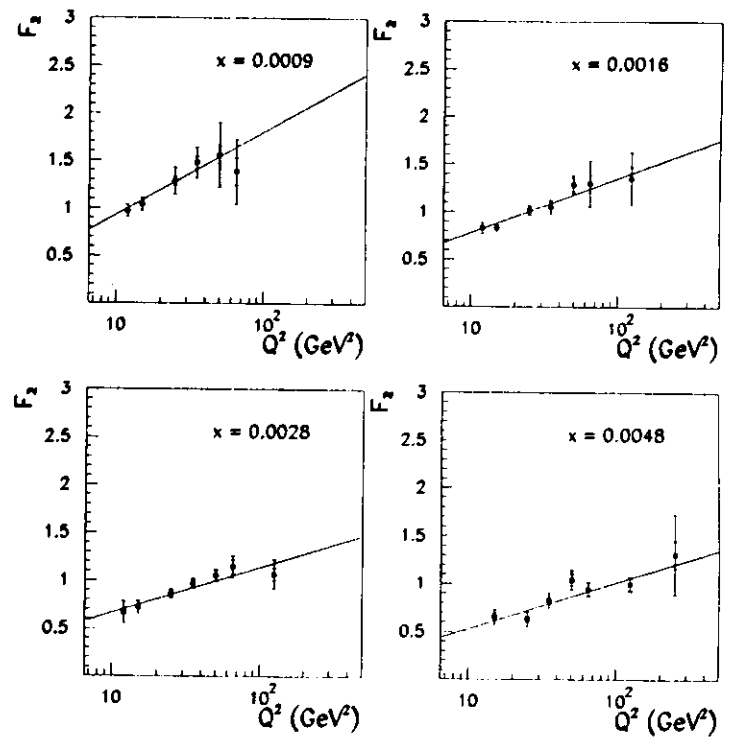


Figure 9.2: *$F_2$ values, obtained with the Double Angle method, plotted as functions of $Q^2$ at fixed $x$, together with the linear fits using eq. (9.18).*

is plotted in figures 9.3 and 9.4, in LO and NLO, respectively. The inner error bars represent the statistical errors, while the outer error bars give the statistical and positive/negative systematic errors added in quadrature.

In addition to the experimental systematic errors discussed above, there are also theoretical systematic uncertainties, not shown in the figures. The error on $\alpha_s$ yields a variation of $\pm 6\%$ for both methods in LO and NLO. For the EKL method, the results are very sensitive to the choice of $\omega_0$. Varying $\omega_0$ from 0.3 to 0.5 results in a 40% increase of $xg(x,Q^2)$. For the Prytz method, recall that neglecting the quark contribution to the $F_2$ scaling violations results in a 5-8% overestimate of the gluon density, and that the method is found to be accurate at a 10% level, as discussed in section 9.2.

The discussion of these results for the gluon distribution in the proton follows in chapter 10.



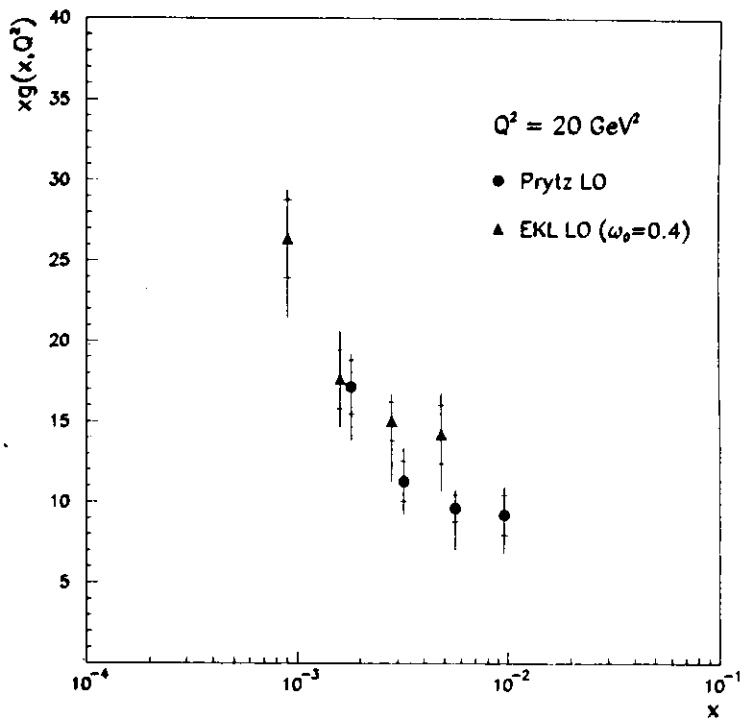


Figure 9.3: *The gluon momentum density of the proton as a function of $x$ at $Q^2 = 20\ GeV^2$ extracted from the $F_2$ scaling violations using the Prytz and EKL methods in LO. The inner error bars represent the statistical errors. The outer error bars represent the statistical and (experimental) systematic errors added in quadrature.*

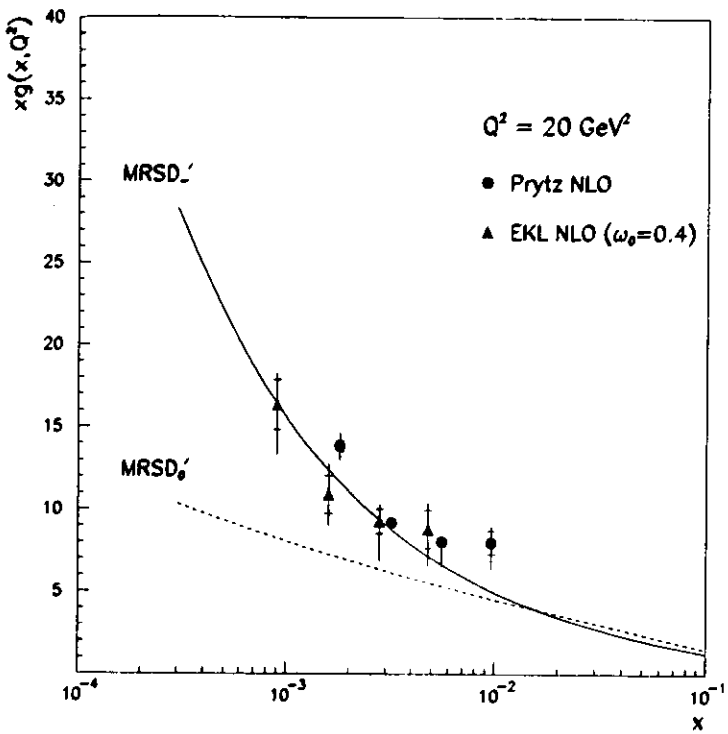


Figure 9.4: *The gluon momentum density of the proton as a function of $x$ at $Q^2 = 20\ GeV^2$ extracted from the $F_2$ scaling violations using the Prytz and EKL methods in NLO. The inner error bars represent the statistical errors. The outer error bars represent the statistical and (experimental) systematic errors added in quadrature. Also shown are the $MRSD'_-$ (full curve) and $MRSD'_0$ (dashed curve) gluon parametrizations.*



# Chapter 10

# Discussion

## 10.1 The Proton Structure Function $F_2$

The 1993 HERA data extend the measurement of $F_2$ to lower values of $x$ and both higher and lower values of $Q^2$ compared to the 1992 data. The higher luminosity of the 1993 run has reduced the statistical errors by a factor of 2.5 compared to the 1992 measurement, while better understanding of the detector, reconstruction and unfolding methods has led to smaller systematic errors by a factor of 50% or more.

The most striking feature of the measured proton structure function $F_2$ is its strong rise with decreasing $x$, which is in contrast to the almost constant behaviour of $F_2$ at larger values of $x$. The rise is steeper in the lower $Q^2$ values but it persists for $Q^2$ up to 500 GeV$^2$. It was first observed in the 1992 HERA data and is confirmed with the 1993 data presented in this thesis.

The expected logarithmic scaling violations of $F_2$ are confirmed for the first time in the new region of low $x$ and high $Q^2$ with the 1993 HERA data, as shown in fig. 9.1.

The use of the Electron method in the $F_2$ measurement is first made feasible in the 1993 analysis. In most of the $(x, Q^2)$ bins, the Double Angle and

Electron $F_2$ values agree with each other within errors (see fig. 8.6). In some of the low-$Q^2$, low-$x$ bins, the Electron method values lie higher than the Double Angle values using the uncorrected electron energies for event selection cuts. The disagreement is caused by the electron energy corrections, which shift the scattered electron energy to higher values. Using corrected electron energies for event selection cuts in the Double Angle method results in agreement with the Electron method. In all $Q^2$ bins, the $F_2$ values from the two methods find the same slopes, as functions of $x$. The two analyses are independent in the sense that the selected samples (although overlapping), the reconstruction methods, and the systematic effects are different. The agreement between the two methods is a powerful systematic check of the results. However, since the Electron method is implemented only in a limited kinematic region, and the degradation of its resolution due to inactive material is not completely recovered after the electron energy corrections, we choose the Double Angle results as the final $F_2$ values.

Before comparing the measured $F_2$ values with the various Parton Distribution Functions (see section 1.10), it must be noted that for values $x > 10^{-2}$, where a large amount of fixed target DIS data exists, all parametrizations agree with each other. It is HERA that offers the unique possibility of distinguishing among the various PDFs, at low $x$. The comparison of our final $F_2$ values with the PDFs available at the time of this analysis is shown in figures 8.4 and 8.5.

In fig. 8.4 our results are compared with the PDFs that follow the conventional fitting procedure (see section 1.10). At the lowest values of $Q^2$, MRSD'_, which has a singular gluon and sea quark distribution as $x \to 0$ at $Q^2 = Q_0^2 = 4$ GeV$^2$, and MRSD'$_0$, which has a constant behaviour, span our data. At $Q^2 = 35$ GeV$^2$ and above the data agree with the MRSD'_ curves. The MRSA parametrization, which has a singular (but softer than the MRSD'_) gluon, and which has included the 1992 and some preliminary 1993 HERA data in the GLAP fit, reproduces well the final 1993 results at $Q^2 = 25$ GeV$^2$ and above. In the lowest $Q^2$ bins it lies slightly above our data. The CTEQ2 parametrization, which has also included the 1992 HERA data in the GLAP fit, has a singular gluon, and starts the QCD evolution from a low reference value of $Q_0^2 = 1.6$ GeV$^2$, agrees well with the 1993 data at all values of $Q^2$.



In fig. 8.5 our final $F_2$ values are compared with the GRV parton distributions, which are generated radiatively from a valence-like input. The GRV(HO) curves, which treat all quarks as intrinsic massless partons, lie above our data in the four lowest $Q^2$ bins. The GRV94 parametrizations, on the other hand, which take in account the mass of the heavy quarks ($c$, $b$), lie closer to the data.

## 10.2 The Gluon density of the Proton

The scaling violations of $F_2$, confirmed for the first time with the 1993 HERA data in the low-$x$ region, $1.5 \cdot 10^{-4} < x < 10^{-2}$, are used to estimate the gluon momentum distribution in the proton.

The scaling violations become larger as $x$ decreases, as can been seen from the increasing slope of $F_2$, $dF_2(x,Q^2)/d\ln Q^2$, with decreasing $x$, in fig. 9.2.

The gluon momentum density in the proton is found to rapidly increase

as $x$ decreases from $10^{-2}$ to $9 \cdot 10^{-4}$, as can be seen in figures 9.3 and 9.4. This rapid increase of the gluon density with decreasing $x$ is in accord with the steep rise of $F_2$ at low $x$, since the sea quark distributions, generated by the gluons, dominate the $F_2$ structure function at low values of $x$.

The extracted gluon distribution clearly favors the singular gluon behaviour of $\mathrm{MRSD}'_-$, rather than the constant gluon of $\mathrm{MRSD}'_0$, as can be seen in fig. 9.4. The latter lies lower than the lower limits of our error bars.

The results from the two approximate methods used to extract the gluon distribution from the $F_2$ scaling violations are in good agreement. This indicates that the different approximations made by the two methods are justified. In the Prytz method, the quark contribution to the $F_2$ scaling violations was completely neglected in the low-$x$ region relevant to this analysis. The gluon momentum density, however, was not assumed to behave as any specific function. In the EKL method, on the other hand, the quark contribution was included, but a specific singular functional form was assumed for $xg(x, Q^2)$. The results justify the choice of the functional form and confirm that the $F_2$ scaling violations at low $x$ are dominated by gluons.



# Chapter 11

# Summary and Outlook

The 1993 HERA data, corresponding to an integrated luminosity of 0.515 $\mathrm{pb}^{-1}$, have been used to measure the proton structure function $F_2(x, Q^2)$ in the region $7 < Q^2 < 2560$ GeV$^2$ and $1.5 \cdot 10^{-4} < x < 0.16$. The scaling violations of $F_2$ have been used to extract the gluon momentum density of the proton, $G(x, Q^2)$, at $Q^2 = 20$ GeV$^2$ and $9 \cdot 10^{-4} < x < 0.96 \cdot 10^{-2}$.

The structure function $F_2$ is found to rapidly rise with decreasing $x$. The gluon distribution also shows a substantial increase at small $x$. The GLAP evolution equations are found to adequately describe the scaling violations of $F_2$ in the kinematic region measured.

The low-$x$ region in DIS has been an exciting area of theoretical speculations (before and after the start of HERA data) and experimental HERA results. However, there are important questions that still need an answer. The region of validity of the GLAP evolution equations, as opposed to the limit where the resummation of the large $\ln(1/x)$ terms becomes important (in the double logarithmic approximation and the BFKL equation) has to be clarified. Whether parton recombination occurs, the scale at which it starts, and the way it approaches the saturation limit (uniformly or concentrating around "hot spots") has to be determined.

The 1994 and 1995 HERA data, in conjunction with new ZEUS detector components at very small angles around the beam-pipe, extend the kinematic region to even lower values of $x$ and $Q^2$. The 1994 $F_2$ measurement reaches values of $x$ as low as $6 \cdot 10^{-5}$ and values of $Q^2$ as low as 2 GeV$^2$. The 1995 measurement is expected to reach values of $Q^2$ less than 1 GeV$^2$. The exploration of this new low-$x$, low-$Q^2$ region may provide some answers to the open questions mentioned above.

The upcoming measurements of the $F_2$ proton structure function in the low-$Q^2$ kinematic region will also close the gap between HERA and the DIS fixed target experiments.

In addition, the higher statistics of the 1994 and 1995 HERA data will enable a measurement of the gluon density of the proton with methods other than the scaling violations of $F_2$ (i.e. jet rates, $J/\psi$ production), providing a crucial check of the gluon results presented here.

Deep Inelastic $ep$ Scattering has proved to be a powerful tool in exploring the structure of the proton in the last thirty years. HERA has extended our knowledge in a completely new regime, and will continue doing so in the near future.



# References


1. R. Hofstadter and R.W. McAllister, Phys. Rev. 102 (1956) 851.

2. G.F. Chew and S.C. Frautschi, Phys. Rev. Lett. 8 (1961) 394

3. M. Gell-Mann, Caltech Synchrotron Laboratory Report CTSL-20 (1961), unpublished.
   M. Gell-Mann, Phys. Rev. 125 (1962) 1067.
   Y. Ne'eman, Nucl. Phys. 26 (1961) 222.
   M. Gell-Mann and Y. Ne'eman, *The Eightfold Way*, Benjamin (1964).

4. M. Gell-Mann, Phys. Lett. 8 (1964) 214.
   G. Zweig, CERN-8182/TH 401 (1964).
   G. Zweig, CERN-8419/TH 412 (1964).

5. O. W. Greenberg, Phys. Rev. Lett. 13 (1964) 598.
   M.Y. Han and Y. Nambu, Phys. Rev. 139 (1965) 1006B.

6. W.K.H. Panofsky, Proc. 14th Int. Conf. on High Energy Physics, Vienna (1968), edited by J. Prentki and J. Steinberger, p. 23.
   R. Taylor, Rev. Mod. Phys. 63 (1991) 573.
   H. Kendall, Rev. Mod. Phys. 63 (1991) 597.
   J. Friedman, Rev. Mod. Phys. 63 (1991) 615.

7. J.D. Bjorken, Phys. Rev. 179 (1969) 1547.

8. R.P. Feynman, Phys. Rev. Lett. 23 (1969) 1415.

9. J.D.Bjorken and E.A. Paschos, Phys. Rev. 185 (1969) 1975.

10. J. Kuti and V.F. Weisskopf, Phys. Rev. D 4 (1971) 3418.

11. D.J. Gross and F. Wilczek, Phys. Rev. Lett. 30 (1973) 1343.
H.D. Politzer, Phys. Rev. Lett. 30 (1973) 1346.

12. S. Weinberg, Phys. Rev. Lett. 31 (1973) 494.
D.J. Gross and F. Wilczek, Phys. Rev. D 8 (1973) 3633.

13. R. Taylor, Proc. Int. Symposium on Lepton and Photon Interactions at High Energies (1975) 679.

14. I. Aitchinson and A. Hey, *Gauge Theories in Particle Physics*, A. Hilger (1989).
F. Halzen and A. Martin, *Quarks and Leptons*, Wiley (1984).
T. Muta, *Foundations of QCD*, World Scientific (1987).
R.G. Roberts, *The structure of the proton*, Cambridge University Press (1990).

15. C.G. Callan and D.J. Gross, Phys. Rev. Lett. 22 (1969) 156.

16. V. Gribov and L. Lipatov, Sov. J. Nucl. Phys. 15 (1972) 78,438,675 ??
G. Altarelli and G. Parisi, Nucl. Phys. B 126 (1977) 298.

17. H. Spiesberger et al., *Radiative Corrections at HERA*, Proc. of the Workshop on Physics at HERA, vol. 2 (1992) 798.

18. A. Mueller, Nucl. Phys. B (Proc. Suppl.) 18C (1990) 125.

19. Y. Balitskij and L. Lipatov, Sov. J. Nucl. Phys. 28 (1978) 822.
E. Kuraev, L. Lipatov and V. Fadin, Sov. Phys. JETP 44 (1976) 443.
E. Kuraev, L. Lipatov and V. Fadin, Sov. Phys. JETP 45 (1977) 199.



20. M. Froissart, Phys. Rev. 123 (1961) 1053.

21. L.V. Gribov, E. M. Levin, M.G. Ryskin, Nucl. Phys. B 188 (1981) 555.
L.V. Gribov, E. M. Levin, M.G. Ryskin, Phys. Rep. 100 (1983) 1.

22. ZEUS Collab., M. Derrick et al., Phys. Lett. B 316 (1993) 412.

23. H1 Collab., I. Abt et al., Nucl. Phys. B 407 (1993) 515.

24. A.D. Martin, R.G. Roberts and W.J. Stirling, Phys. Lett. B 306 (1993) 145.

25. NMC Collab., P. Amaudruz et al., Phys. Rev. Lett. 66 (1991) 2712.

26. CCFR Collab., S.A. Rabinowitz et al., Phys. Rev. Lett. 70 (1993) 134.
CCFR Collab., A.O. Bazarko et al., Z. Phys. C 65 (1995) 189.

27. A.D. Martin, R.G. Roberts and W.J. Stirling, Proc. Workshop on Quantum Field Theoretical Aspects of HE Physics, Kyffhässer, Germany, edited by B. Geyer and E.-M. Ilgenfritz, Leiptzig (1993) p. 11.

28. A.D. Martin, R.G. Roberts and W.J. Stirling, Phys. Rev. D 50 (1994) 6734.
A.D. Martin, R.G. Roberts and W.J. Stirling, Rutherford Appleton Laboratory preprint, RAL-95-021, University of Durham preprint, DTP/95/14 (1995).

29. CTEQ Collab., J. Botts et al., Phys. Lett. B 304 (1993) 159.

30. W.K. Tung, *Proceedings of International Workshop on Deep Inelastic Scattering and Related Subjects*, Eilat, Israel (1994) World Scientific, Singapore.

31. CTEQ Collab., H.L. Lai et al., Michigan State University preprint, MSU-HEP-41024 (1994).

32. M. Glück, E. Reya and A. Vogt, Z. Phys. C 53 (1992) 127.
M. Glück, E. Reya and A. Vogt, Phys. Lett. B 306 (1993) 391.

33. M. Glück, E. Reya and A. Vogt, Dortmund preprint, DO-TH 94/24, DESY preprint, DESY 94-206 (1994).

34. ZEUS Collab., *The ZEUS Detector, Status Report 1993* (1993).

35. A. Kwiatkowski, H. Spiesberger and H.-J. Möhring, *HERACLES. An Event Generator for ep Interactions at HERA Including Radiative Processes*, Proc. of the Workshop on Physics at HERA, vol. 3 (1992) 1294.

36. B. Andersson et al., Z. Phys. C 43 (1989) 625.

37. L. Lönnblad, Comput. Phys. Commun. 71 (1992) 15.

38. B. Andersson et al., Phys. Rep. 97 (1983) 31.

39. T. Sjöstrand, Comput. Phys. Commun. 39 (1986) 347.

40. R. Brun et al., *GEANT 3.13*, CERN DD/EE/84-1 (1987).

41. T. Sjöstrand, *PYTHIA at HERA*, Proc. of the Workshop on Physics at HERA, vol. 3 (1992) 1405.

42. G. Ingelman, *LEPTO version 6.1 - The Lund Monte Carlo for Deep Inelastic Lepton-Nucleon Scattering*, Proc. of the Workshop on Physics at HERA, vol. 3 (1992) 1366.



43. F. Jacquet and A. Blondel, Proc. of the study of an *ep* facility for Europe, DESY 79-48 (1979), edited by U. Amaldi, p. 391.

44. S. Brouër et al., *Study of the Experimental Check of Initial State Bremsstrahlung Correction in Deep Inelastic e-p Scattering*, Proc. of the Workshop on Physics at HERA, vol. 2 (1992) 897.

45. ZEUS Structure Function Group, *A Determination of $F_2$ with the 1992 Data*, ZEUS-Note 93-078 (1993).
R. Sinkus and H. Abramowicz, *Electron Identification with Neural Networks at ZEUS*, ZEUS-Note 93-117 (1993).

46. ZEUS Collab., M. Derrick et al., Phys. Lett. B 293 (1992) 465.

47. J. Krüger, *The Uranium Scintillator Calorimeter for the ZEUS Detector at the Electron-Proton Collider HERA*, DESY Internal Report F35-92-02 (1992).

48. A. Caldwell et al., *An Electron Energy Correction Method: A Preliminary Implementation and its Effect on the $F_2$ Measurement*, ZEUS-Note 94-051 (1994).

49. ZEUS Collab., M. Derrick et al., Phys. Lett. B 315 (1993) 481.

50. A.M. Cooper-Sarkar et al., Z. Phys. C 39 (1988) 281.

51. ZEUS Collab., M. Derrick et al., Phys. Lett. B 345 (1995) 576.

52. K. Prytz, Phys. Lett. B 311 (1993) 286.

53. K. Prytz, Phys. Lett. B 332 (1994) 393.

51. R.K. Ellis, Z. Kunszt and E.M. Levin, Nucl. Phys. B 120 (1994) 517.